

TECHNICAL UNIVERSITY OF CRETE  
SCHOOL OF ELECTRICAL AND COMPUTER ENGINEERING  
ELECTRONICS AND COMPUTER ARCHITECTURE DIVISION  
ELECTRONICS LABORATORY  
OPTOELECTRONICS AND IMAGING DIAGNOSTICS  
RESEARCH GROUP



**Novel Spectral Mapping Indices for Improving  
Microscopy and Leukemia Diagnosis**

by

Marios Kastrinakis

A THESIS SUBMITTED IN PARTIAL FULFILLMENT OF THE  
REQUIREMENTS FOR THE MASTER OF SCIENCE OF  
ELECTRICAL AND COMPUTER ENGINEERING

Chania, July 2017

THESIS COMMITTEE  
Professor Costas Balas, *Supervisor*  
Professor Michael Zervakis  
Professor Minos Garofalakis

# Acknowledgements

I would like to thank heartfully many people for helping me not only to complete my thesis but most important for their support and cooperation throughout my postgraduate studies.

Firstly, I would like to thank my family and mostly my parents Antonis and Alexandra that always believe, support and encourage me to pursuit my dreams. I would like to thank wholeheartedly my supervisor Professor Costas Balas, who has offered me valuable knowledge and guidance on the area of optoelectronics and imaging diagnostics during my postgraduate studies and most important for his trust, excellent support and cooperation from the beginning till the end of my work inside his research group. In addition, I would like to thank Professor Michael Zervakis and Professor Minos Garofalakis for their participation in the examination committee.

Finally yet importantly, I would like to thank my fellow colleagues, Papathanasiou A., Tsapras A., Rossos C., Vardoulakis E., Dr. Kortsalioudakis N. and Zografos P., for their cooperation, support and share of their knowledge during the last two creative years that i had the opportunity to work with them. Moreover, a lovely “Thank You” to Ioanna, because above all moments from my student life in Chania, she remains the brightest part.

*To Ioanna, a daily joy.*

# Abstract

The rise and evolution of optical light microscopes is inevitable, as microscopy constitutes a key diagnostic and imaging tool for many fields of science, such as medicine, biology, chemistry as well as for many applications in industry. However, the internationally accepted technology residue regards to the physical limitations of the microscopes' resolution and the biological limitations of the examiners' perception, quest the improvement of imaging ability in microscopy. In addition, the evaluation of the imaging information of diagnostic importance urges the development of computational methods that will highlight and measure it quantitatively.

In this thesis, a novel method is reported for measuring and enhancing imaging resolution in microscopy, based on a single measurement of one-dimensional modulation transfer function combined with Wiener deconvolution algorithm. Additionally, for the first time in the relevant literature to the best of our knowledge, a computational method is presented for improving diagnostic accuracy of leukemia, using optical light microscopes along with spectral imaging. A set of spectral indices are introduced that have been extracted and measured quantitatively, through chemometrics regression algorithm combined with spectral imaging of peripheral blood smears.

The proposed methods are capable to achieve enhanced optical resolution of up to 176% for a brightfield microscope at 23.8x of total optical magnification, beyond microscope's optical limit. Furthermore, they achieve 100% sensitivity with 98.91% specificity in cases of Acute Lymphoblastic Leukemia, by detecting lymphoblasts accurately and 74.86% sensitivity with 96.94% specificity in cases of Chronic Lymphocytic Leukemia, by differentiating and indicating abnormal lymphocytes from the normal ones quantitatively. Thus, the proposed methods can be easily employed as additional analytical tools for minimizing errors and increasing accuracy, either in the diagnosis and in the classification of ALL and CLL leukemia.

# Table of Contents

Acknowledgements .....	2
Abstract .....	4
Table of Contents.....	5
List of Abbreviations.....	8
List of Figures .....	9
List of Tables .....	12
1 Introduction .....	13
2 Theoretical Background .....	15
2.1 Electro-Optical Imaging Systems.....	15
2.1.1 Point Spread Function Model.....	17
2.1.2 Modulation Transfer Function Model.....	18
2.1.2.1 Resolution.....	18
2.1.2.2 Contrast/Modulation.....	20
2.1.2.3 Definition of MTF as a measure of optical performance .....	20
2.1.3 Image Degradation Model.....	22
2.2 Microscopy .....	24
2.2.1 Compound System Design .....	24
2.2.1.1 Key Components .....	26
2.2.1.2 Common Microscopy Techniques .....	27
2.2.2 Method for Quantitative Analysis of Stained Microscopy Samples .....	29
2.2.2.1 Spectral Imaging and Classification.....	30
2.2.2.2 Chemometrics.....	31
2.2.2.3 Generalization of Beer-Lambert Law.....	31
2.3 Human Blood and Leukemic Abnormalities .....	32
2.3.1 Eukaryotic Cell Structure.....	33
2.3.2 Blood Physiology .....	34
2.3.2.1 Plasma.....	34
2.3.2.2 Buffy Coat.....	35
2.3.2.3 Erythrocytes .....	38
2.3.3 Hematopoiesis .....	39
2.3.3.1 Bone Marrow.....	39
2.3.3.2 Hematopoietic Series .....	40

---

2.3.3.3	Blasts.....	40
2.3.4	Leukemia .....	41
2.3.4.1	Acute Lymphoblastic Leukemia .....	42
2.3.4.2	Chronic Lymphocytic Leukemia .....	43
2.3.5	Blood and Bone Marrow Samples Staining and Examination .....	45
2.3.5.1	May Grünwald – Giemsa Stain .....	45
2.3.5.2	Microscopy Examination Procedure .....	46
3	Method for Measuring and Enhancing Imaging Resolution in Microscopy .....	47
3.1	MTF Estimation via Slanted Edge Analysis.....	47
3.1.1	Method's Analysis.....	47
3.1.2	Method's Algorithm.....	49
3.1.3	Algorithm Implementation .....	53
3.1.4	Evaluation of Implementation .....	54
3.2	Deconvolution for Enhancing Microscopy Imaging Resolution .....	57
3.2.1	Wiener Deconvolution Model .....	58
3.2.2	Two-Dimensional OTF Extraction Method.....	59
3.2.3	Noise to Signal Ratio Estimation Method .....	60
3.2.4	Implementation and Results .....	61
3.2.4.1	OTF Calibration over Magnifications and Wavelengths .....	62
3.2.4.2	$K_{NSR}$ Calibration over Camera Sensor Gains and Channels .....	64
3.2.4.3	Method Implementation and Flowchart .....	65
3.2.4.4	Brightfield and Fluorescence Deconvolution Examples .....	67
4	Method for Improving Leukemia Diagnosis .....	70
4.1	Presentation of Microscope System.....	71
4.2	System Training with Experimental MG-G Stain Mixtures .....	72
4.3	Method for Identification and Separation of Blood Cells.....	76
4.3.1.1	WBCs Nuclei Binary Mask Estimation Module .....	78
4.3.1.2	Blood Cells Contours Binary Mask Estimation Module.....	79
4.3.1.3	Complete WBCs and WBCs Cytoplasm Binary Masks Estimation Module .....	80
4.3.1.4	RBCs Binary Mask Estimation Module .....	82
4.4	Method for Stains Uptake Analysis and WBC Classification .....	83
4.4.1.1	Cytometry Statistics Calculation Module.....	85
4.4.1.2	Stains Uptake Indices Calculation Module.....	85
4.4.1.3	WBCs Classification Module .....	85

---

4.5	Method Implementation.....	87
4.6	Results on Leukemic Samples .....	89
4.6.1	Analysis of Normal Population.....	90
4.6.2	Acute Lymphoblastic Leukemia Results.....	91
4.6.3	Chronic Lymphocytic Leukemia Results .....	92
4.6.4	Overall Classification Results .....	94
5	Conclusions and Future Work .....	96
	References and Bibliography .....	98
	Appendix A: Normal Population Samples Analysis .....	102
	Appendix B: Acute Lymphoblastic Leukemia Samples Analysis.....	104
	Appendix C: Chronic Lymphocytic Leukemia Samples Analysis .....	106

# List of Abbreviations

**ADC:** Analog to Digital Converter  
**ALL:** Acute Lymphoblastic Leukemia  
**AML:** Acute Myelogenous Leukemia  
**CBC:** Complete Blood Count  
**CCD:** Charge-Coupled Device  
**CLL:** Chronic Lymphocytic Leukemia  
**CML:** Chronic Myelogenous Leukemia  
**CMOS:** Complementary Metal-Oxide Semiconductor  
**DBC:** Differential Blood Count  
**DSLR:** Digital Single-Lens Reflex Camera  
**DFT:** Discrete Fourier Transform  
**EMR:** Electro-Magnetic Radiation  
**EO:** Electro-Optical  
**FAB:** French–American–British System  
**FOV:** Field of View  
**HSC:** Hematopoietic Stem Cell  
**LP/MM:** Line Pairs per Millimeter  
**LRL:** Lower Reference Range  
**MG-G:** May Grünwald – Giemsa Stain  
**MTF:** Modulation Transfer Function  
**NSR:** Noise to Signal Ratio  
**OTF:** Optical Transfer Function  
**PhTF:** Phase Transfer Function  
**PSF:** Point Spread Function  
**RBC:** Red Blood Cells  
**RMSE:** Root Mean Square Error  
**ROI:** Region of Interest  
**LED:** Light Emitting Diode  
**MAGN:** Magnification  
**SI:** Spectral Imaging  
**SNR:** Signal to Noise Ratio  
**TMAG:** Total Magnification  
**URL:** Upper Reference Level  
**WBC:** White Blood Cells

# List of Figures

Figure 2.1: Electro-magnetic wave components. ....	15
Figure 2.2: Electro-magnetic radiation spectrum. ....	16
Figure 2.3: Common electro-optical imaging system capable to operate within visible part of spectrum. ....	16
Figure 2.4: Example of PSF and its relationship with Airy Disc. ....	17
Figure 2.5: 1951 USAF bar target. ....	18
Figure 2.6: Perfect line edges before and after EO imaging system. ....	19
Figure 2.7: Imaging of line pairs with a common sensor. ....	19
Figure 2.8: Contrast/modulation as an ideal square wave. ....	20
Figure 2.9: Contrast of a bar target at object plane and image plane. ....	20
Figure 2.10: Graphical explanation of a MTF plot. ....	21
Figure 2.11: Overall MTF degradation throughout an imaging system. ....	22
Figure 2.12: Different types of optical aberrations. ....	23
Figure 2.13: Image degradation model. ....	24
Figure 2.14: Anatomy of a compound microscope. ....	25
Figure 2.15: A compound microscope combined with an imaging sensor. ....	25
Figure 2.16: Reflective objective design. ....	26
Figure 2.17: Refractive objective design. ....	26
Figure 2.18: Brightfield microscopy illumination system. ....	27
Figure 2.19: Sample under brightfield illumination. ....	27
Figure 2.20: Darkfield microscopy illumination system. ....	28
Figure 2.21: Sample under darkfield illumination. ....	28
Figure 2.22: Basic optical design of a fluorescence microscope. ....	29
Figure 2.23: Sample under fluorescence microscopy. ....	29
Figure 2.24: Spectral signatures extracted from spectral cube. ....	30
Figure 2.25: Graphical representation of Beer-Lambert law. ....	31
Figure 2.26: Eukaryotic cell structure. ....	33
Figure 2.27: Main parts of human blood. ....	34
Figure 2.28: Human blood parts separation after centrifugation. ....	34
Figure 2.29: Stained band neutrophil (left) and segmented neutrophil (right). ....	36
Figure 2.30: Stained eosinophil. ....	36
Figure 2.31: Stained basophil. ....	36
Figure 2.32: Stained monocyte. ....	37
Figure 2.33: Stained lymphocyte. ....	38
Figure 2.34: Stained platelets (marked with arrows). ....	38
Figure 2.35: Stained erythrocytes. ....	38
Figure 2.36: The procedure of hematopoiesis in humans. ....	39
Figure 2.37: Structure of human bone marrow. ....	40
Figure 2.38: ALL abnormality in lymphoid series. ....	43
Figure 2.39: Stained lymphoblasts in peripheral blood smear. ....	43
Figure 2.40: CLL abnormality in lymphoid series. ....	44
Figure 2.41: Abnormal lymphocytes (1) and smudge cells (2) in CLL. ....	44

---

Figure 2.42: Peripheral blood smear stained with MG-G.....	45
Figure 2.43: Meander-like movement, during examination of blood smears.....	46
Figure 2.44: Examination areas of a blood smear. ....	46
Figure 3.1: Example of a slanted edge target. ....	47
Figure 3.2: Calculation procedure of MTF using a slanted edge target. ....	48
Figure 3.3: Real edge (left) and imaged edge (right).....	49
Figure 3.4: Projection of a slanted edge on sensor plane.....	49
Figure 3.5: Visual representation of MTF estimation algorithm. ....	51
Figure 3.6: Flowchart of slanted edge MTF algorithm. ....	52
Figure 3.7: Execution flow of slanted edge MTF program. ....	53
Figure 3.8: Zeiss Axio Scope A1 Series.....	54
Figure 3.9: Zeiss EC Plan-Neofluar objectives. ....	54
Figure 3.10: Custom-made slanted edge MTF target for microscopes by Thor Labs.....	55
Figure 3.11: MTF measurements repeatability for 5x objective.....	56
Figure 3.12: MTF measurements repeatability for 10x objective. ....	57
Figure 3.13: MTF measurements repeatability for 40x objective. ....	57
Figure 3.14: Visual representation of 2D OTF estimation method. ....	60
Figure 3.15: Lumnia BF-FL-Hem Multi-Modal microscope by Holoptica P.C.....	62
Figure 3.16: Measuring of MTF on Lumnia Microscope. ....	63
Figure 3.17: Measured MTF curves across different magnifications, using 530nm LED.64	
Figure 3.18: Interpolated MTF curves across different magnifications, using 530nm LED.....	64
Figure 3.19: Measured $K_{NSR}$ curves across different gain settings, using broadband white LED.....	65
Figure 3.20: Program execution for enhancing imaging resolution in microscopy.....	66
Figure 3.21: Algorithm flowchart for enhancing resolution in microscopy. ....	67
Figure 3.22: Deconvolution results on spectral image of 530nm.....	68
Figure 3.23: Deconvolution results on color image. ....	68
Figure 3.24: Deconvolution results on fluorescence image of 532nm excitation wavelength. ....	69
Figure 4.1: Spectral unmixing procedure and concentrations estimation, using SIMPLS algorithm, on MG-G stained samples.....	72
Figure 4.2: Laboratory setup for measuring MG-G components absorbance spectra. ....	74
Figure 4.3: Methylene Blue measured absorbance spectra. ....	75
Figure 4.4: Azure B measured absorbance spectra.....	75
Figure 4.5: Eosin Y measured absorbance spectra. ....	76
Figure 4.6: MG-G components mixtures measured absorbance spectra. ....	76
Figure 4.7: Flowchart of blood cells identification and separation method. ....	77
Figure 4.8: Steps of WBC nuclei binary mask estimation module. ....	79
Figure 4.9: Steps of blood cells contours binary mask estimation module. ....	80
Figure 4.10: Steps for estimation of complete WBC binary mask.....	81
Figure 4.11: Watershed transform on joined leukocytes.....	81
Figure 4.12: WBC cytoplasm binary mask extraction.....	82
Figure 4.13: Steps of RBCs binary mask estimation module. ....	83
Figure 4.14: Flowchart of leukocytes classification and stains uptake analysis method. 84	

---

Figure 4.15: Developed program for blood cells identification, separation and classification. ....	88
Figure 4.16: Example of stains uptake plot, for a normal lymphocyte.....	89
Figure 4.17: Lymphoblast's characteristic pattern of MG-G's components uptake in nucleus. ....	92
Figure 4.18: Abnormal (CLL) lymphocyte's characteristic pattern of MG-G's components uptake in nucleus.....	93
Figure 4.19: Normal (mature) lymphocyte's characteristic pattern of MG-G's components uptake in nucleus.....	94
Figure 4.20: Neutrophil's (Rest WBC) characteristic pattern of MG-G's components uptake in nucleus. ....	95

# List of Tables

Table 1: Major types of leukemic diseases.....	42
Table 2: MG-G staining effects on blood cells components.....	46
Table 3: Resolutions of Zeiss EC Plan-Neofluar objectives based on manufacturer.....	55
Table 4: Measured resolution of Zeiss EC Plan-Neofluar objectives with developed program.....	56
Table 5: Quantitative results of the proposed method for enhancing imaging resolution in microscopy (all resolutions correspond to object plane).....	69
Table 6: Full Factorial Design for MG-G components.....	73
Table 7: Used dataset overview.....	90
Table 8: Reference ranges of lymphocytes from normal population, for MG-G's components uptake indices.....	91
Table 9: Reference ranges of detected leukocytes and erythrocytes amount, within normal population.....	91
Table 10: Confusion matrix for identification of lymphoblasts over lymphocytes.....	92
Table 11: Confusion matrix for differentiation of normal from abnormal lymphocytes.....	93
Table 12: Confusion matrix for differentiation of lymphoid from rest WBCs.....	94
Table 13: Confusion matrix of overall classification results.....	95
Table 14: Analysis of MG-G stain's components uptake for lymphocytes in normal population.....	102
Table 15: Cytometry statistics for normal population.....	103
Table 16: Analysis of MG-G stain's components uptake for lymphoblasts in ALL samples.....	104
Table 17: Analysis of MG-G stain's components uptake for lymphocytes in ALL samples.....	104
Table 18: Cytometry statistics for ALL samples.....	105
Table 19: Analysis of MG-G stain's components uptake for lymphocytes in CLL samples.....	107
Table 20: Cytometry statistics for CLL samples.....	108

# 1 Introduction

Over the last four centuries, the rise and evolution of optical light microscopes was inevitable, as microscopy constitutes an integral diagnostic and imaging tool for many fields of science, such as medicine, biology, chemistry as well as for many applications in industry [1]. Starting back in 17<sup>th</sup> century, when Dutch scientist Antonie van Leeuwenhoek developed the bi-convex lenses of small focal length, in order to achieve high magnifications of small objects [2]. Since then, the design of optical microscopes evolved in their today's form of compound setups.

However, concurrently with optical light microscopy, the need for advanced observations of specimens has led to the development of new setups that are able to reveal specific characteristics and structures of samples under examination. Indicatively, fluorescence microscopes are capable to image specific cellular structures (e.g., intracellular skeleton structures, nucleus organelles, elements of genetic material, etc.), using a combination of appropriate fluorophores and monochromatic illuminations [3]. It is a fact that microscopes are not used as mere observation devices, but employed as major diagnostic instruments in a wide range of biological and medical procedures, such as cytology, pathological anatomy, biopsy or even leukemia diagnosis [4].

The progress on the improvement of optical light microscopes' imaging ability is necessary, as well as on the development of computational methods that are capable to highlight and measure the important diagnostic information quantitatively, while microscopy remains a wide applied, accessible and inexpensive method of examination [5]. More specifically, an optical light microscope is capable to provide optical magnifications of up to 2000x by an appropriate combination of objectives, ocular lenses and immersion oils, while physical phenomena and production imperfections are restricting the retrieved resolution considerably, at these levels of magnification. Additionally, the human eye as organ of visual perception is unable to fully perceive, differentiate and quantify significant diagnostic information, especially in cases as leukemia diagnosis.

The internationally accepted technology residue regards to the physical limitations of the microscopes' resolution and the biological limitations of the examiners' perception and quantification of the imaging information of diagnostic importance [6] is the motivation of this master thesis. This thesis reports, for the first time in the relevant literature to the best of our knowledge, a method for post capturing enhancement of resolution for color and spectral images, beyond the microscopes

imaging limitations based on a single measurement of one-dimensional modulation transfer function combined with Wiener deconvolution algorithm. Additionally, a novel method for improving diagnostic accuracy of Acute Lymphoblastic and Chronic Lymphocytic Leukemia is introduced, based on new spectral indices that are capable to identify and classify cells of diagnostic importance quantitatively. This thesis is organized in three main chapters. The first chapter includes an extensive analysis of the theoretical background used for the development of the aforementioned methods. The second chapter presents the methods for measuring and improving imaging resolution in microscopes, while the third and last main chapter introduces the novel spectral indices for improving Acute Lymphoblastic and Chronic Lymphocytic Leukemia diagnosis and classification.

## 2 Theoretical Background

In this chapter, the theoretical background is analyzed that underlies every main research area of this thesis. Firstly, an introduction is made to concepts of common electro-optical (EO) imaging systems and more precisely how electro-magnetic radiation (EMR) is transformed into digital images and why digital images are degraded due to systems' imperfections and physical limiting phenomena. Consequently, the main aspects of microscopy are explained along with its most widely used applications, as well as methods for analyzing stained microscopy samples quantitatively. Finally, a deep introduction is performed to the procedure of human hematopoiesis and the corresponding types of blood cancers.

### 2.1 Electro-Optical Imaging Systems

Electro-magnetic radiation (EMR) is a form of radiant energy that has characteristics of both waves and photon particles, a property called as wave-particle duality, and propagating through space. In vacuum, EMR is propagated with a characteristic speed, the speed of light, normally in straight lines. EMR is emitted and absorbed by charged particles. As an electromagnetic wave, it has both electric and magnetic field components, which oscillate in a fixed relationship to one another, perpendicular to each other and perpendicular to the direction of energy and wave propagation [Figure 2.1].

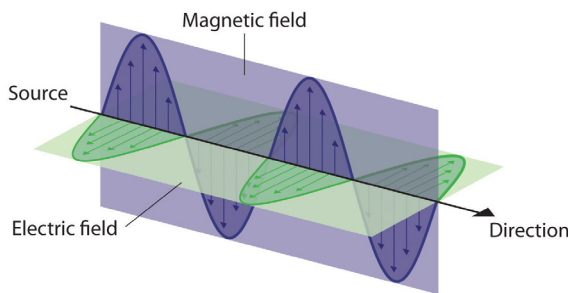


**Figure 2.1:** Electro-magnetic wave components.

The characteristics of an electromagnetic wave are the wavelength  $\lambda$  (physical length of a full oscillation) and the frequency  $\nu$  (number of oscillations per second). Electro-magnetic radiant energy is a continuous flow of particles or wave energy packages, called photons [7]. Photon's energy is calculated as  $E_{\text{photon}} = h \cdot \nu = h \cdot \frac{c}{\lambda}$ , where  $h$  is the Planck's Constant and  $c$  equals to the speed of light in empty space.

Depending on wavelength, the EMR is divided into several different bands (also known as spectral bands), and every band interacts with matter in a different way [7]. All those bands together form the electro-magnetic spectrum [Figure 2.2].

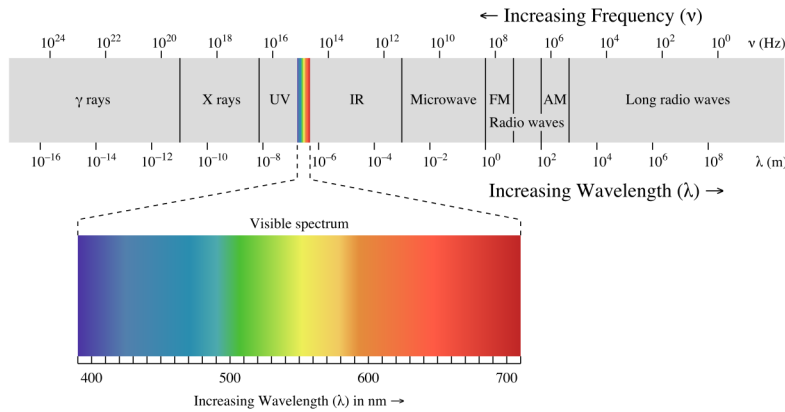


**Figure 2.2:** Electro-magnetic radiation spectrum.

Common electro-optical (EO) imaging systems convert EMR of specific optical wavelengths to electrical signals for source detection and/or analog/digital visual display. They extend human vision in wavelength, signal sensitivity, distance, and environmental conditions. An image of a scene is relayed on a focal plane that has an imaging sensor, which performs the transduction of light to video signals [8]. In general, every electro-optical imaging modality is composed by 1) an optical assembly (i.e. a set-up of optical elements such as lenses, prisms, filters, etc.), that has the ability to collect, limit and focus EMR rays of selected wavelengths onto focal plane, 2) a detection medium that converts photons to electrical signal (for example, a CMOS sensor that is sensitive in Vis-NIR wavelengths) and 3) a digital processing and storage system that is capable to display and save digital images (i.e. a computer, the body of a digital camera, etc.) [Figure 2.3].

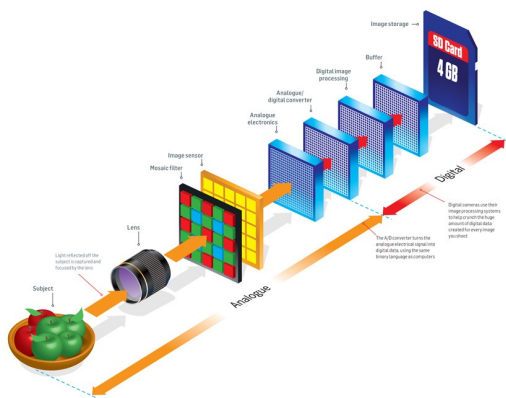


**Figure 2.3:** Common electro-optical imaging system capable to operate within visible part of spectrum.

### 2.1.1 Point Spread Function Model

An image of an object/real scene is composed by imaging a countless number of light-emitting point sources that apart the objects/scene under observation. However, those sources are not imaged as points of light, but as extended patterns of intensity distribution. This effect is known as diffraction of light [9], i.e. interference effect of the diffracted waves. As a result, light energy directed towards focal point is spread into a cone of converging energy focusing into a 3-D pattern of energy distribution (known as Airy's Pattern) that sets the limit to image contrast and resolution in an aberration-free and circular aperture optical system.

This pattern of wave interference that consists of a bright central disc surrounded by several rapidly fading concentric rings and normalized to 1 at its peak, is also known as the Point Spread Function (PSF) of the optical system.

Physical size of the diffraction pattern in the plane of best focus is inversely proportional to the relative aperture  $\frac{1}{f}$ , with the first minima radius given by  $r_{AD}=1.22 \cdot \lambda \cdot F$ , where  $\lambda$  denotes the wavelength of EMR,  $F$  the focal ratio  $\frac{f}{D}$ , and  $f$  and  $D$  denotes the imaging system's focal length and diameter, respectively [10]. In addition, the area from PSF's peak to first minima is also called as Airy's Disc [Figure 2.4].

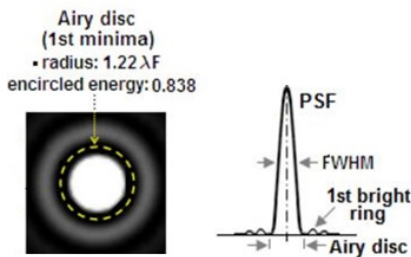


**Figure 2.4:** Example of PSF and its relationship with Airy Disc.

The PSF can be Fourier transformed in two dimensions to yield the two dimensional Optical Transfer Function (OTF) of the optical system {2.1}. OTF is a complex-valued function, having both magnitude and phase [11]. The magnitude is also referred as the Modulation Transfer Function (MTF) and the phase as the Phase Transfer Function (PhTF) {2.2}. In cases of well-corrected optical systems (i.e. aberration-free) that are illuminated by incoherent light sources, the OTF would be symmetric and real for all spatial frequencies and thus, the phase part can be considered as negligible [5].

$$PSF(x, y) \xrightarrow{\mathcal{F}} OTF(u, v) \quad (2.1)$$

where  $x, y$  are spatial coordinates and  $u, v$  frequency coordinates.

$$OTF(u, v) = MTF(u, v) \cdot e^{i \cdot PhTF(u, v)} \quad (2.2)$$

where  $MTF(u, v) = |OTF(u, v)|$ ,  $PhTF(u, v) = \arg[OTF(u, v)]$  and  $\arg[]$  corresponds to phase part of complex-valued function.

## 2.1.2 Modulation Transfer Function Model

Modulation Transfer Function is a measure of the transfer of modulation (i.e. transfer of contrast) from the object/scene under observation to the captured (optical or even digital) image. In addition, measuring MTF is the most widely accepted method (in industry and academia) for evaluating electro-optical imaging systems' performance [12].

When an object is observed through an optical system, the resulting image will be degraded due to inevitable aberrations and diffraction phenomena, as presented previously. The amount of that degradation can be measured quantitatively and be described using the model of MTF. MTF is characterized by two key parameters of imaging performance; resolution and contrast (i.e. modulation) [13].

### 2.1.2.1 Resolution

Resolution [14] is an electro-optical imaging system's ability to distinguish object details. It is often expressed in terms of line-pairs per millimeter (where a line-pair is a sequence of one black line and one white line). This measure of line-pairs per millimeter (lp/mm) is also known as spatial frequency. The inverse of the frequency yields the spacing in millimeters between two resolved lines. Bar targets with a series of equally spaced, alternating white and black bars (for example, a 1951 USAF target [Figure 2.5]) are ideal for measuring resolvable resolution in line pairs per millimeter.

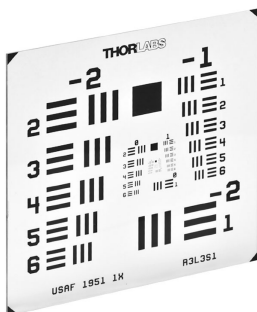


**Figure 2.5:** 1951 USAF bar target.

For all EO systems, when imaging such a pattern, perfect line edges become blurred to a degree [Figure 2.6]. High-resolution images are those that exhibit a

large amount of detail because of minimal blurring. Conversely, low-resolution images lack fine detail.

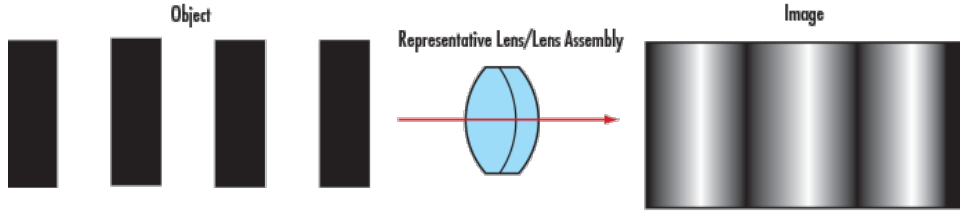


**Figure 2.6:** Perfect line edges before and after EO imaging system.

In addition, in an EO imaging system, two camera sensor pixels are needed for imaging each line-pair, one pixel is dedicated to the colored (black) line and the other to the blank space between pixels [Figure 2.7]. Thus, the maximum possible resolvable resolution is limited by the camera sensor size, and it is equal to twice its pixel size. This is the Nyquist frequency of the sensor, beyond which the sensor's response is useless.

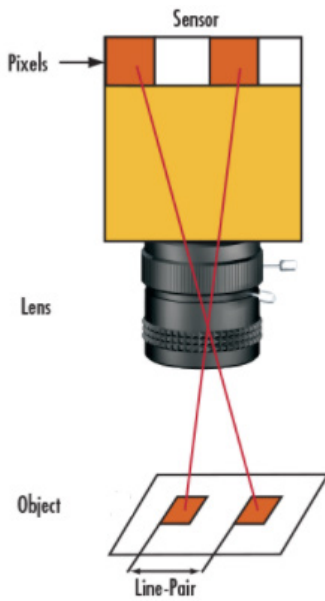


**Figure 2.7:** Imaging of line pairs with a common sensor.

In addition, the resolved resolution of the observed object or scene is calculated by taking into consideration the measured resolution (in  $\mu\text{m}$  {2.3} or lp/mm {2.4}) and the total magnification (TMAG) factor of the system [15].

$$\text{Object Resolution } (\mu\text{m}) = \frac{\text{System Resolution } (\mu\text{m})}{\text{TMAG}} \quad (2.3)$$

$$\text{Object Resolution } (\text{lp/mm}) = \text{System Resolution } (\text{lp/mm}) \cdot \text{TMAG} \quad (2.4)$$

### 2.1.2.2 Contrast/Modulation

Contrast [16] or modulation of an EO imaging system can be described as how faithful the minimum and maximum intensity values are transferred from object plane to image plane. More specifically, normalizing the gray-scaled intensity of a measured bar target by assigning a maximum value to the white bars and zero value to the black bars and plotting these values results in a square wave, from which the notion of contrast can be more easily seen [Figure 2.8].

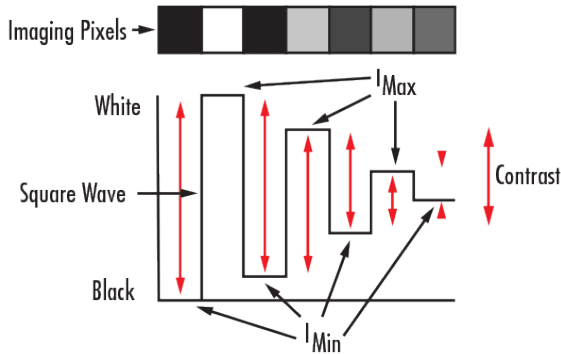


**Figure 2.8:** Contrast/modulation as an ideal square wave.

Mathematically, contrast/modulation is calculated as in {2.5}:

$$\text{Contrast or Modulation} = \frac{I_{max} - I_{min}}{I_{max} + I_{min}} \quad (2.5)$$

According to this explanation, the intensity pattern of [Figure 2.6] will seem after imaging as in [Figure 2.9].

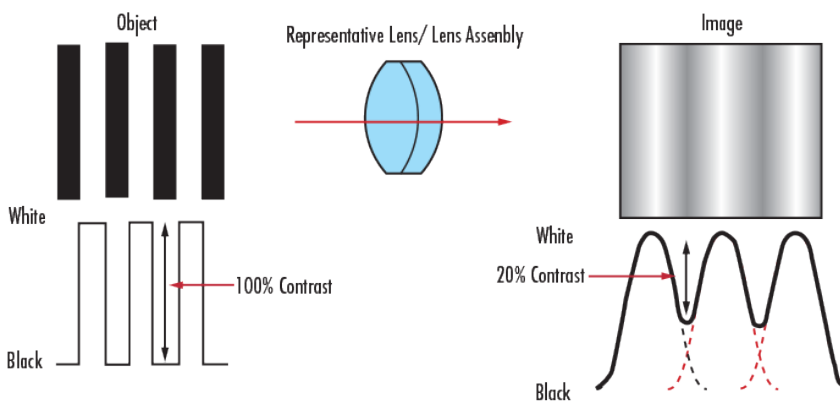


**Figure 2.9:** Contrast of a bar target at object plane and image plane.

### 2.1.2.3 Definition of MTF as a measure of optical performance

Considering the above, MTF is defined as in {2.6}:

$$MTF(f) = \frac{\text{Relative Image Contrast}}{\text{Relative Object Contrast}} = \frac{M_{\text{image}}(f)}{M_{\text{object}}(f)} \quad (2.6)$$

where  $M_{\text{image}}$  and  $M_{\text{object}}$  is the modulation (contrast) of captured object (i.e. on image plane) and the modulation (contrast) of original object (i.e. on object plane) respectively, and  $f$  the different measured spatial frequencies (in lp/mm or um) [13].

Now, that the concepts of modulation (contrast), resolution and spatial frequency are well defined, it can easily be understood that an MTF curve describes the amount of modulation (i.e. contrast) (in y-axis) that an EO imaging system can represent (i.e. transfer) across various spatial resolutions (in x-axis) [Figure 2.10].

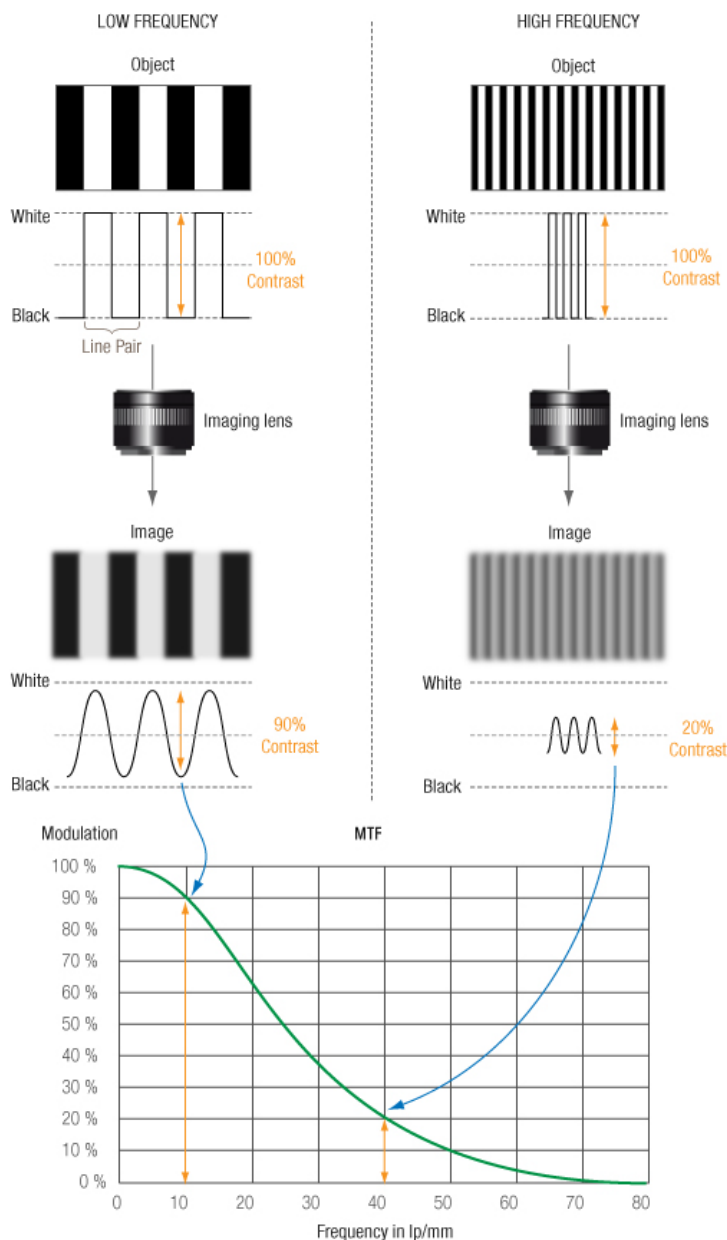


**Figure 2.10:** Graphical explanation of a MTF plot.

An ideal EO imaging system would have high modulation values below the Nyquist frequency and low modulation values for equal or greater frequencies.  $f_C$  is the cut-off frequency of the EO imaging system and is spotted at the frequency where modulation reaches zero. However, if the Nyquist frequency is smaller that defines the cut-off frequency and it is calculated as  $f_N = 1/(2 \cdot \text{Pixel Size})$ . A common point for evaluating and comparing different EO imaging systems is where modulation drops at 50% and frequencies where modulation is less than 15% are irresolvable by humans [17].

Usually, in EO imaging systems the components with lower responses are the optical elements (such as lenses, prisms, etc.) and not the imaging sensor because optical elements' geometry affects more the ability of reproducing high quality images. Specifically, in a common EO imaging system MTF is affected by the lens diameter (D), the focal length (f), the f-stop (f/#), the size of imaging sensor, the field position and from the wavelength of illumination [18]. Finally, the total measured MTF response of a system is the multiplication of all individual MTF responses from different components of the system (such as lens, prisms, imaging sensor, digital processing units, even atmosphere, etc.), as depicted in [Figure 2.11] briefly.

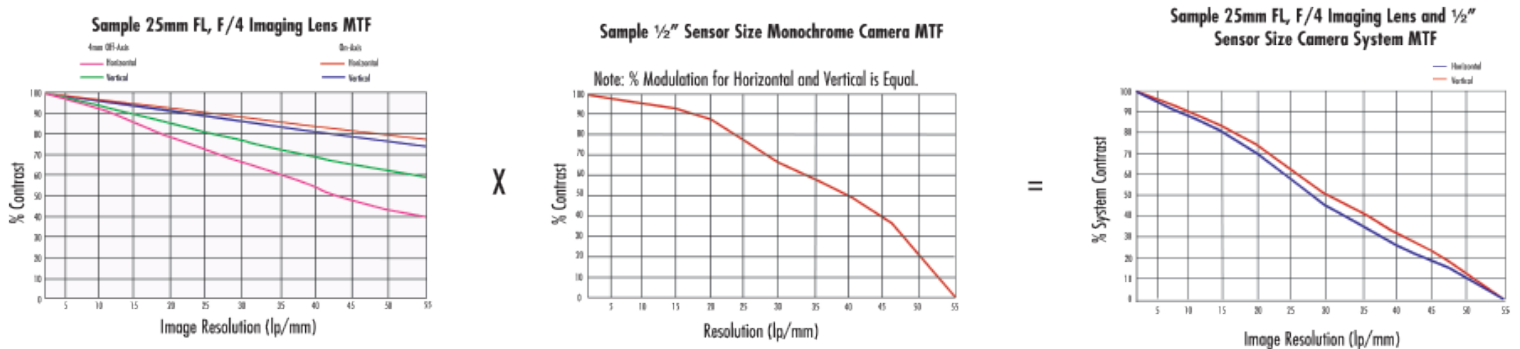


**Figure 2.11:** Overall MTF degradation throughout an imaging system.

### 2.1.3 Image Degradation Model

In subsection 2.1.1, it was analyzed how Point Spread Function corresponds to the physical phenomenon of diffraction. However, even the most perfect procedures cannot produce completely aberration-free optics. Thus, the existence of different types of optical aberrations are common in the optical parts (such as defocus, tilt, spherical aberration, astigmatism, coma, distortion, etc.) [19]. In addition, user-infused abnormalities during capturing (such as motion blur, poor focus, bad illumination), aberrations due to simultaneous illumination with different wavelengths (such as in color imaging) or even physical limitations of used digital sensor (such as size or type), can alter the system's PSF with result serious degradation of image quality.

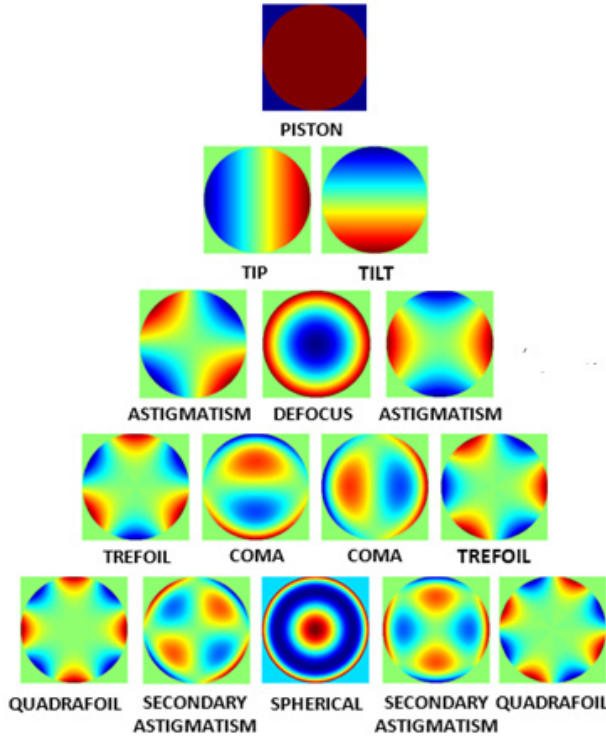


**Figure 2.12:** Different types of optical aberrations.

However, PSF encapsulates every possible reason of image's quality degradation and in fact describes the response of an imaging system to a point source or a point object. In non-coherent imaging systems such as fluorescent microscopes, telescopes, optical microscopes and commercial imaging systems, image formation process is linear in power and described by linear systems' theory [20]. This means that when two objects A and B are imaged simultaneously, the result is equal to the sum of the independently imaged objects. In other words, the imaging of A is unaffected by the imaging of B and vice versa, owing to the non-interacting property of photons. Thus, the image of a complex object can then be seen as a convolution of the true object and the PSF, a fact that leads to the following model of image degradation by an imaging system.

An observed image  $g(x, y)$ , neglecting additive noise due to electronics, can be estimated to be the two-dimensional convolution of the true image  $f(x, y)$  with a linear shift-invariant kernel  $h(x, y)$ , also known as PSF of the imaging system. That is,

$$g(x, y) = f(x, y) * h(x, y) = \sum_{(n,m)} f(n, m) \cdot h(x - n, y - m) \quad (2.7)$$

where  $x, y$  are spatial coordinates. In a graphical representation, the operation of image degradation can be depicted as:

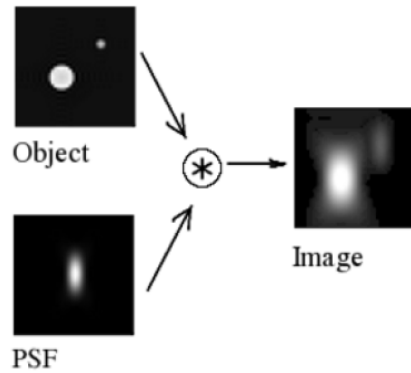


**Figure 2.13:** Image degradation model.

The kernel in {2.7} can depend on  $(x, y)$  (spatially-varying), or can be constant across the image plane (spatially-invariant). Spatially-invariant blur is more common as spatial variations in the kernel are negligible, across optical microscopes' field.

## 2.2 Microscopy

Microscopy [21] is an imaging technique for visualizing and analyzing objects/areas that cannot be seen by the naked eye (objects/areas that are not within the resolution range or vision capabilities of the normal eye). Microscopes are instruments designed to produce magnified visual or digital images of objects too small to be seen by the naked eye.

A microscope must accomplish three tasks:

1. Produce a magnified image of the specimen,
2. Separate the fine details in the image, and
3. Render the details visible to the human eye or camera.

The working principle of every microscope is the magnification, as microscopes produce magnified images of the objects upon are focused.

### 2.2.1 Compound System Design

Every compound microscope contains multiple lens elements and parts [Figure 2.14]. The three basic components of a microscope are the eyepieces (or ocular lenses), the objectives lenses and the illumination unit (consisted from light source, condenser, and aperture). The objective, located closest to the object, relays a real image of the object to the eyepiece (on real image plane a.k.a. intermediate image plane). This part of the microscope is needed to produce the basic magnification. The eyepiece, located closest to the eye, projects and magnifies this real image of the object [21].

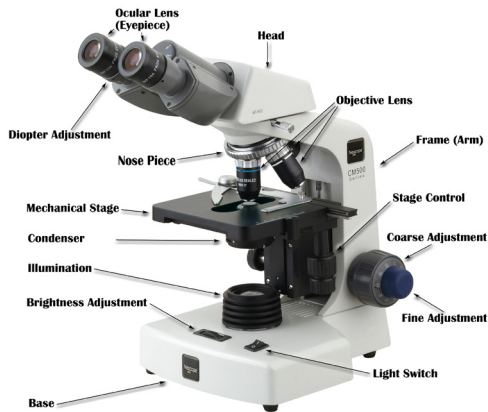


**Figure 2.14:** Anatomy of a compound microscope.

As the microscope magnifies into steps, the magnifying effect is multiplied and the overall magnification of the system can be calculated according to {2.10}:

$$MAGN_{overall} = MAGN_{Objective} \cdot MAGN_{Eyepiece} \quad (2.10)$$

However, accompanying with eyepieces, digital imaging sensors (such as CCD, CMOS or even DSLR body) are mounted on microscopes, in order to view, store and analyze further digital images of specimens under examination [Figure 2.15]. In such cases, images appear extremely large on the observation monitor. The overall magnification is normally very high indeed and can be calculated very easily; it is the product of the optical and electronic magnification [22].

1. The optical magnification is:  $MAGN_{Optical} = MAGN_{Objective} \cdot MAGN_{Adapter}$ .
2. The electronic magnification is the ratio of the monitor diagonal to the diagonal of the active area of the imaging sensor:  $MAGN_{electronic} = \text{MonitorDiagonal} / \text{SensorDiagonal}$ .
3. The overall magnification then is:  $MAGN_{overall} = MAGN_{optical} \cdot MAGN_{electronic}$ .



**Figure 2.15:** A compound microscope combined with an imaging sensor.

### 2.2.1.1 Key Components

- **Eyepieces**

Eyepieces (or ocular lenses) hold a major role in microscopes' design, due to the fact that they are one of the two key components for magnifying the object under examination. Microscope eyepieces generally consist of several lens elements in a housing, with a barrel on one end. By switching eyepieces, the user can adjust what is viewed. For instance, eyepieces will often be interchanged in order to increase or decrease the magnification of a microscope.

- **Objectives**

Objectives allow microscopes to provide magnified, real images and are, perhaps, the most complex component because of their multi-element design. Objectives are available with magnifications ranging from 2x – 200x. They are classified into two main categories: the traditional refractive type and reflective type.

In a refractive design light passing through the system is refracted, or bent, by the optical elements. Each optical element is typically anti-reflection coated to reduce back reflections and improve overall light throughput [Figure 2.17]. On the other hand, reflective objectives utilize a reflective, or mirror-based design. Reflective objectives consist of a primary and secondary mirror system [Figure 2.16] to magnify and relay the image of the object under inspection.

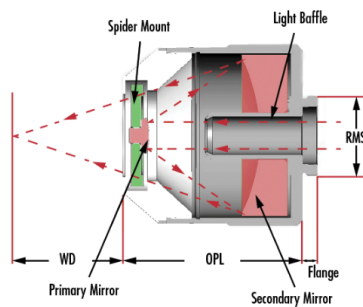


**Figure 2.16:** Reflective objective design.

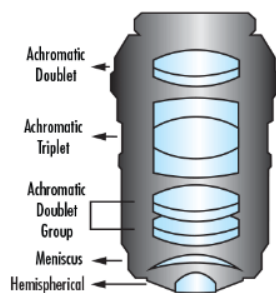


**Figure 2.17:** Refractive objective design.

### 2.2.1.2 Common Microscopy Techniques

- **Brightfield Microscopy**

Many microscopes utilize backlight illumination compared to traditional direct light illumination because the latter usually over-saturates the object under inspection. A specific type of backlight illumination used in microscopy applications is bright-field illumination [23]. In bright-field illumination, incident light from an illumination source, such as a halogen lamp, floods the object under inspection with light from behind [Figure 2.18]. It employs a lens called condenser, in order to aim the source's light. The condenser usually contains an aperture diaphragm to control and focus light on the specimen.

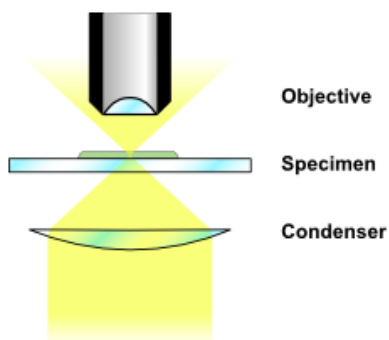


**Figure 2.18:** Brightfield microscopy illumination system.

Bright-field illumination is designed to provide bright and even illumination on the object plane and on the image plane. In bright-field illumination, the specimen's background appears bright [Figure 2.19].

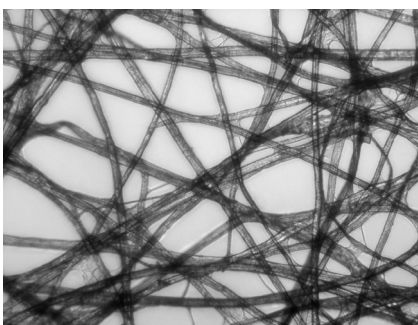


**Figure 2.19:** Sample under brightfield illumination.

- **Darkfield Microscopy**

Dark-field illumination creates contrast between the object and the surrounding field of view. As the name implies, the background is dark and the object is bright. An annular stop is used to create a cone of oblique illumination, thus with no specimen present all the light from the condenser misses the objective entirely, giving a dark background [23]. However, if a specimen containing reflective

structures is placed into the path of this illumination, light that hits such a structure will be reflected at all angles [Figure 2.20]. Some of this light will now reach the objective and so will appear bright.

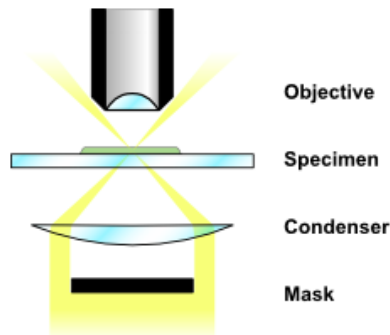


**Figure 2.20:** Darkfield microscopy illumination system.

This method produces a great deal of glare; therefore the specimen often appears as a bright silhouette rather than a bright object, of which little detail can be determined [Figure 2.21].

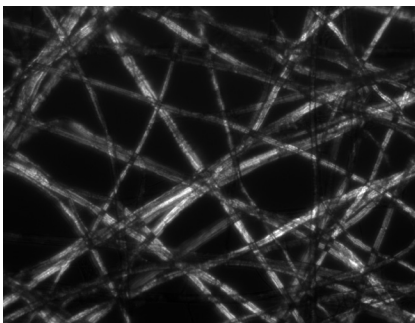


**Figure 2.21:** Sample under darkfield illumination.

- **Fluorescence Microscopy**

A fluorescence microscope [24] is an optical microscope that uses fluorescence, or in addition to, reflection and absorption to study properties of specimens. The specimen is illuminated with light of a specific wavelength (or wavelengths) which is absorbed by the fluorophores, causing them to emit light of longer wavelengths (i.e., of a different color than the absorbed light). The illumination light is separated from the much weaker emitted fluorescence through the use of a spectral emission filter. Typical components of a fluorescence microscope are a light source (xenon arc lamp or mercury-vapor lamp are common; more advanced forms are high-power LEDs and lasers), the excitation filter, the dichroic mirror (or dichroic beam splitter), and the emission filter [Figure 2.22]. The filters and the dichroic mirror are chosen to match the spectral excitation and emission characteristics of the fluorophore used to label the specimen. In this manner, the distribution of a single fluorophore (color) is imaged at a time.

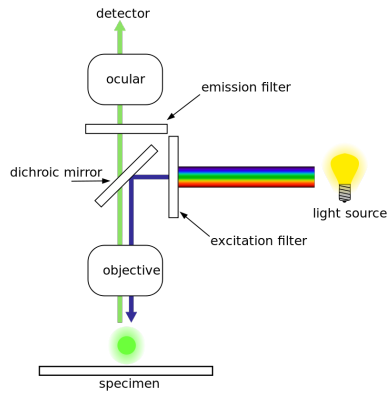


**Figure 2.22:** Basic optical design of a fluorescence microscope.

Multi-color images of several types of fluorophores must be composed by combining several single-color images [Figure 2.23].

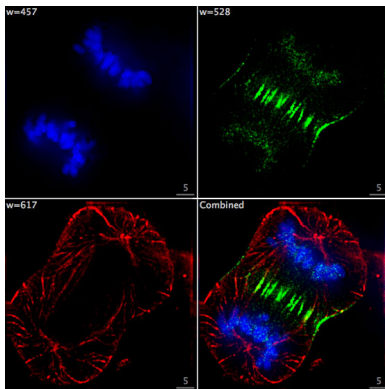


**Figure 2.23:** Sample under fluorescence microscopy.

### 2.2.2 Method for Quantitative Analysis of Stained Microscopy Samples

A biomarker, or biological marker [25], is in general a substance used as an indicator of a biological state. It is a characteristic that is objectively measured and evaluated as an indicator of normal biological processes, pathogenic processes, or pharmacologic responses to a therapeutic intervention. Biomarkers of diagnostic importance can be highlighted with the use of biomedical stains and it is a common practice during examination of biological samples under light microscopes.

An integral part of this thesis, is the usage of a method for analyzing stained biological samples under microscopy examination quantitatively, in order to determine the absolute abundance (often expressed as concentration) of the several biological stains present in the sample. The exact and accurate knowledge of the concentration of these stains is exploited further, in order to introduce new indices for improving specific diagnostic procedures, as is explained in future chapter.

To handle the aforementioned challenge, methods of spectral unmixing are

employed, in order to achieve the desired quantitative analysis of the stained samples under examination. Thus, in this subsection are presented key concepts of this methodology.

### 2.2.2.1 Spectral Imaging and Classification

Spectral imaging (SI) is a modality, hybrid between imaging and spectroscopy, and has been applied to numerous areas of science, now emerging in biomedical engineering. The main idea is acquiring two dimensional images across a wide range of electro-magnetic spectrum (for example UV, Visible, Infrared) using a two-dimensional imaging sensor (i.e., CCD or CMOS). Then, a three-dimensional dataset of spatial and spectral information is gathered. That dataset is called spectral cube. With the spatial information, it is located more accurately the light's interaction with the object under examination, pixel by pixel [26].

It is assumed that each pixel, depending on the light it collected from the object on each wavelength, has its own spectral signature (measurement of emitted, reflected or absorbed EMR at specific wavelengths which can uniquely identify an object), as shown in [Figure 2.24].

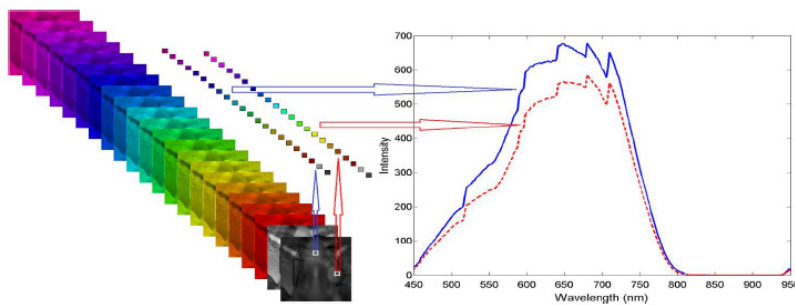


**Figure 2.24:** Spectral signatures extracted from spectral cube.

The images of the spectral cube, can be used to extract unique data concerning the object by classifying the pixels using the spectral signatures pixel by pixel. When light propagates through a biological tissue or sample, undergoes multiple scattering and absorption. Scattering and absorption characteristics are unique for each kind of tissue and when a pathological condition is present, they seem to change depending on the condition's progression. Capturing that reflected or transmitted light with the right tools, in different wavelengths and processing those data, may result to quantitative and significant diagnostic information about the specific biological target's pathology.

As mentioned, for any given material, when exposed to light, the amount of radiation absorbed, reflected, transmitted varies with the wavelength, as shown in picture above. This property of matter gives the opportunity to uniquely identify different physical or chemical substances and separate them using their spectral signatures [27]. This separation is also known as spectral classification.

### 2.2.2.2 Chemometrics

Chemometrics is the use of statistical and mathematical techniques in order to extract information from chemical systems using multivariate statistics and applied mathematics. Chemometrics usually involves linear algebra methods to make qualitative or quantitative measurements of chemical data [28].

In this thesis, chemometrics are used in combination with acquired spectral cubes, in order to unmix and estimate the concentrations of the different stains on stained blood microscopy samples. These concentrations are measured in Molarity (units: mol/L or M), which represents the number of moles of a dissolved substance per liter of solution [29]. The algorithm used is a Statistically Inspired Modification of the Partial Least Square algorithm (SIMPLS), widely used in chemometrics [30], faster than classical PLS implementation and with the same predictive efficiency [31]. The SIMPLS algorithm produces a predictive model as described in {2.11}:

$$Y = B \cdot X + e \quad (2.11)$$

where  $X$  are the absorbance data extracted from acquired spectral cube,  $Y$  are the estimated concentrations of the stains under decomposition,  $e$  is the dumped components of the system and  $B$  is the matrix of coefficients that describe the linear relations between concentrations and absorbances of the stains on the sample under examination.

### 2.2.2.3 Generalization of Beer-Lambert Law

The assumption that the concentrations of the stains in the microscopy samples are related in a manner to the data from a measurement technique (i.e., the cubes from spectral imaging) is the key to quantitative analysis.

Beer-Lambert Law defines a linear relationship between the spectrum and the composition of a sample [32]. It forms the basis of nearly all other chemometrics methods for spectroscopic data. Simply stated, the law claims that when a sample is placed in the beam of a spectrometer, there is a direct and linear relationship between the amount (concentration) of its constituent(s) and the amount of energy it absorbs [Figure 2.25].

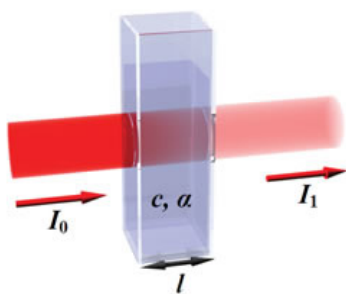


Figure 2.25: Graphical representation of Beer-Lambert law.

In mathematical terms, Beer-Lambert Law is defined as in {2.12}:

$$A = \log\left(\frac{I_0}{I_1}\right) = -\log(T) = \log\left(\frac{1}{T}\right) = a \cdot l \cdot C \quad (2.12)$$

where:

**A:** Absorbance

**I<sub>0</sub>:** Intensity of the incident light.

**I<sub>1</sub>:** Intensity of the transmitted light.

**T:** Transmittance, usually expressed as a percentage %T.

**C:** Concentration of the sample's solution measured in mol/L or M (molarity).

**l:** Path length that the light beam has travelled inside the sample (in cm).

**a:** Molar absorptivity of the solution, which is a constant number also proportional to the respective absorbance wavelengths.

Finally, it should be noted that the Beer-Lambert law is valid under the following conditions:

- The solutions are not dense (absorbance is between:  $0.1 \leq A \leq 0.9$ ).
- The only mechanism for the interaction between a dissolved substance and radiation is absorption.
- The incident radiation to a sample is monochromatic.
- The sample is in a cuvette (quartz glass in our case) with a uniform intersection.
- The absorbing molecules act individually (no chemical reactions between substances).

## 2.3 Human Blood and Leukemic Abnormalities

Human Blood [33] is a constantly circulating fluid, the most important in humans for their lives, that is responsible for several vital operations. Briefly, blood conducts the transportation of oxygen and nutrients between different organs and parts of human body, of the metabolic wastes in order to get eliminated as well as for the distribution of various hormones. In addition, it is responsible for the regulation of body's temperature, tissue's pH and for the prevention of infections through its immune mechanisms.

The lifelong production of human blood and its cells, occurs in haemopoietic tissue and organs as part of a process called hematopoiesis [34]. This procedure is based in a very high level of cells' turnover, demanded by the need to replace mature circulating blood cells at a rapid rate, and is necessitated by the limited lifespan of the mature blood cells.

However, the procedure of hematopoiesis can be disturbed during its different stages, with result serious abnormalities to the production of mature blood cells

[35]. Lymphoma is a category of blood abnormal condition, considered as a form of blood cancer, in which a specific category of blood cells multiply abnormally inside lymph nodes and other tissues. The enlarging tissues and disruption of blood's functions, can eventually cause organ failure. In advanced stages, a lymphoma may be transformed to leukemia, an advanced form of blood cancer, in which the same category of blood cells multiply abnormally and circulate through the blood system. A delayed diagnosis and application of the appropriate treatment, can end up to death with high probability.

### 2.3.1 Eukaryotic Cell Structure

A cell is the basic structural, functional and biological unit of all known living organisms. It is the smallest unit of life that can be replicated independently. Before explaining further various aspects of human's blood physiology, it is necessary to present the basic structure and components of a eukaryotic cell [36], in which category belongs every human blood cell.

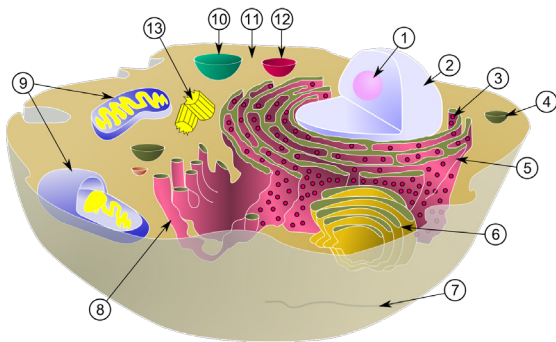


**Figure 2.26:** Eukaryotic cell structure.

1. Nucleoli (consists of RNA chromatin).
2. Nucleus (consists of DNA and RNA chromatin).
3. Ribosome.
4. Cyst.
5. Rough Endoplasmic Reticulum.
6. Golgi Apparatus.
7. Cytoskeleton.
8. Smooth Endoplasmic Reticulum.
9. Mitochondria.
10. Vacuole.
11. Cytoplasm (consists of acidic components).
12. Specific Granules of Immune System Cells (Azurophilic, Neutrophilic, Eosinophilic, Basophilic).
13. Centerpieces in the Central Unit.

Finally, the entire cell is surrounded by a cellular membrane structure.

### 2.3.2 Blood Physiology

Blood is considered as a connective tissue anatomically, due to its origin in the bones and its function. The two major components of blood are [Figure 2.27]:

1. Plasma, which makes up 55% of blood volume.
2. Formed cellular elements, which combine to make the remaining 45% of blood volume. The formed cellular elements are divided further into two major subcategories; the buffy coat and the erythrocytes.

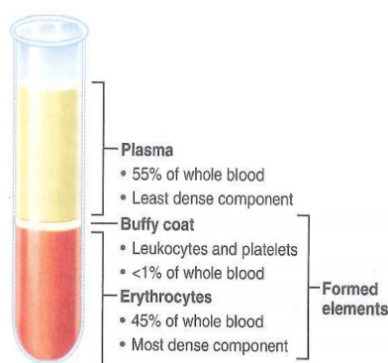


**Figure 2.27:** Main parts of human blood.

#### 2.3.2.1 Plasma

Plasma [33] is made up of 90% water, 7-8% soluble proteins, 1% carbon-dioxide and 1% elements in transit. One percent of the plasma is salt, which helps with the pH of the blood. The largest group of solutes in plasma contains three important proteins. Those are; albumins (60-80%), globulins, and clotting proteins.

Plasma also carries respiratory gases; CO<sub>2</sub> in large amounts (about 97%) and O<sub>2</sub> in small amounts (about 3%), various nutrients (glucose, fats), wastes of metabolic exchange (urea, ammonia), hormones and vitamins.



**Figure 2.28:** Human blood parts separation after centrifugation.

### 2.3.2.2 Buffy Coat

Buffy coat [33] is made up of leukocytes and platelets.

- **Leukocytes**

Leukocytes [37] (or White Blood Cells - WBC) are usually the larger cellular elements of human blood (10-14  $\mu\text{m}$  in diameter) with concentrations of 7 million/mL of blood and they are translucent, since they do not contain hemoglobin. WBC main purpose is for immune response and they are classified into two major subcategories; Granulocytes and Agranulocytes.

Granulocytes are separated into three different types; Neutrophils (60-70% of WBC), Eosinophils (1-4% of WBC) and Basophils (0.25-0.5% of WBC). In addition, agranulocytes are separated into Monocytes (2-6%) and Lymphocytes (25-33%), while the last are distinguished further to T-Cells, B-Cells and Natural Killers.

All these kinds of cells are involved in processes of inflammation and fighting infections and they are existing into peripheral blood normally. On the other hand, various types of precursor cells, such as Myeloblasts, Promyelocytes, Myelocytes, Metamyelocytes, etc. are present in peripheral blood only in case of pathological conditions. A complete presentation of each kind of peripheral blood's WBC with their properties is following:

- i. Neutrophils

The Neutrophilic Granulocytes are typically circular, with low nuclear to cytoplasmic ratio and a diameter of about 14 $\mu\text{m}$ . The granules are stained neutral (very light lilac) and the cytoplasm pinkish. Neutrophils subdivision is based on the structure of their nucleus; Band Neutrophils and Segmented Neutrophils. The band neutrophils, are less developed and more immature than the segmented type, which is mature and divided into 3 to 5 lobes connected by thin chromatin filaments. The nucleoli are absent.

Lack of neutrophils is called neutropenia, while increased number is called neutrophilia. One of the main functions of neutrophils is to protect against bacterial infections, phagocytosing and destroying pathogens. Neutrophils can leave the bloodstream and migrate to surrounding tissues, to fight infections. Neutrophilia has several causes. The mobilization of adherent neutrophils is typical stress characteristic (stress leukocytosis). Acute infections and inflammations may result to mobilization of neutrophils from the bone marrow. Neutropenia is associated with a pharmacological treatment of infections (e.g., parvoviruses, malaria) and autoimmune diseases (e.g. systemic lupus erythematosus). The presence of increased hyper-segmented neutrophil count is usually evidence of lack of vitamin B12 or folic acid (megaloblastic anemia).

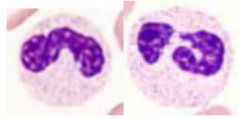


**Figure 2.29:** Stained band neutrophil (left) and segmented neutrophil (right).

ii. Eosinophils

The Eosinophilic Granulocytes are typically circular, with low nuclear to cytoplasmic ratio and a diameter of about  $16\mu\text{m}$ . Their granules are stained as red-orange and they are very densely packed. Nucleus is mature and usually with two lobes connected by thin chromatin filament and nucleoli are absent. Eosinophils are rarely found in the peripheral blood smears.

The eosinophils have an important role in allergy and parasitic infections. Like neutrophils, they are able to phagocytose and migrate. The increased number of eosinophils is characterized as eosinophilia, while reduced number as eosinopenia. Eosinophilia mainly caused by allergy and parasitic diseases. Many pharmacological treatments can also cause eosinophilia. Some neoplastic diseases (e.g. Hodgkin's neoplasia) occasionally cause eosinophilia. The cases where eosinophilia's reason is not detectable, are referred as idiopathic eosinophilia syndromes. Eosinophilia is often detected in cases of stress and acute infections.

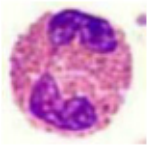


**Figure 2.30:** Stained eosinophil.

iii. Basophils

The Basophilic Granulocytes are typically circular, with low nuclear to cytoplasmic ratio and a diameter that ranges from  $10\mu\text{m}$  to  $14\mu\text{m}$ . The granules stained as dark purple, are very densely packed (obscuring the underlying nucleus and cytoplasm), while nucleoli are absent. They are very rarely encountered in peripheral blood smears.

Basophils are important in hypersensitivity reactions. They can leave the bloodstream and migrate to surrounding tissues. Increased number of basophils is characterized as basophilia. Basophilia is observed in cases of chronic myelocytic leukemia and other myeloproliferative syndromes.

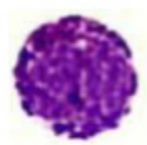


**Figure 2.31:** Stained basophil.

iv. Monocytes

The Monocytes are typically circular, with a diameter of 15 $\mu$ m to 20 $\mu$ m. They are the largest group of peripheral blood cells and they have a lower nuclear to cytoplasmic ratio because of their increased cytoplasm. They have a “kidney shaped” indented nucleus with mature chromatin (clumped). Cytoplasm is abundant, stained as gray to pale blue and with rare to no granules, while vacuoles are commonly noted in cytoplasm.

Increased number of monocytes is known as monocytosis, and decreased number as monocytopenia. Monocytes have the very special ability of immigration. When migrating to the tissues they are called macrophages. Monocytes play an important role in acute and chronic infections. They are important components of cell-mediated immunity. The monocytosis associated with various chronic infections (such as tuberculosis, typhoid fever) and malignant diseases (such as Hodgkin’s). Monocytosis is observed in acute and chronic myelomonocytic leukemia. Monocytopenia occurs in bone marrow aplasia, in hairy cell leukemia and after therapy treatment with steroids.

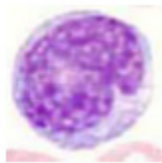


**Figure 2.32:** Stained monocyte.

v. Lymphocytes

Lymphocytes have a round to oval nucleus, usually with high nuclear to cytoplasmic ratio and a diameter of about 10 $\mu$ m. Cytoplasm is scant, stained as light blue and lacks granules. However, the quantity of the cytoplasm to each lymphocyte can vary greatly and that is the cause of the process of separation of lymphocytes in small and large ones. This difference reflects the different lymphocyte activation phases. Lymphocytes are classified in two main morphological types; The cells of one type are relatively small, usually have no granules and therefore exhibit a large nucleus to cytoplasm ratio and the cells of the other type, known as Large Granular Lymphocytes (LGL), are larger, have a smaller nucleus to cytoplasm ratio and contain cytoplasmic basophilic granules. They constitute a percentage of 5-10% of lymphocytes. In addition, there is no morphological distinction between T-Cells and B-Cells.

Lymphocytes are mediators of cellular and humoral immunity. Lymphopenia is observed in cases where the number of lymphocytes is lower than usual, whereas lymphocytosis in cases where the number of lymphocytes is increased. Lymphocytosis observed in lymphoproliferative syndromes, and lymphopenia in cases of infections (such as HIV, tuberculosis, etc.), after radiation treatment and during treatment with immunosuppressive drugs.



**Figure 2.33:** Stained lymphocyte.

- **Platelets**

Platelets, also called thrombocytes, are responsible to stop bleeding by clumping and clotting blood vessel injuries [38]. Platelets have no cell nucleus; they are fragments of cytoplasm that are derived from the megakaryocytes of the bone marrow, and then enter the circulation. These inactivated platelets are biconvex discoid (lens-shaped) structures, with  $2\mu\text{m}$  to  $3\mu\text{m}$  in greatest diameter and a concentration of 250000 cells per square millimeter of peripheral blood. On a stained peripheral blood smear, platelets appear as small dark purple spots, about 20% the diameter of erythrocytes.

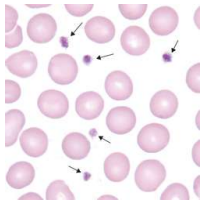


**Figure 2.34:** Stained platelets (marked with arrows).

### 2.3.2.3 Erythrocytes

Erythrocytes [39], also known as Red Blood Cells (RBC), are the most common type of blood cell and their role is to deliver oxygen to the body's tissues and organs via blood flow through the circulatory system. The cytoplasm of RBC is rich in hemoglobin, an iron-containing biomolecule that can bind oxygen and is responsible for the red color of the cells. The cell membrane is composed of proteins and lipids, and this structure provides properties essential for physiological cell function such as deformability and stability while traversing the circulatory system and specifically the capillary network. Mature RBCs are flexible and oval biconcave disks, with concentrations of 5 million cells per square millimeter of peripheral blood. They lack a cell nucleus and most organelles, in order to accommodate maximum space for hemoglobin. On a stained peripheral blood smear, RBCs appear as light reddish disks.

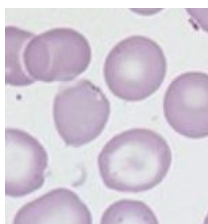


**Figure 2.35:** Stained erythrocytes.

### 2.3.3 Hematopoiesis

Hematopoiesis [40] is a set of processes that are responsible for generating new, mature blood cells. All such cells ultimately derive from a single progenitor cell termed the Multipotential Hematopoietic Stem Cell (HSC) or Hemocytoblast, which undergoes a process of highly regulated division and differentiation that produces the gamut of mature blood cells [Figure 2.36].

During fetal life of humans, hematopoiesis begins in the yolk sac followed by phases in the liver and spleen, and by birth and throughout adult life it takes place in the bone marrow mainly and in the thymus for the development of T-Cells (a subcategory of lymphocytes).

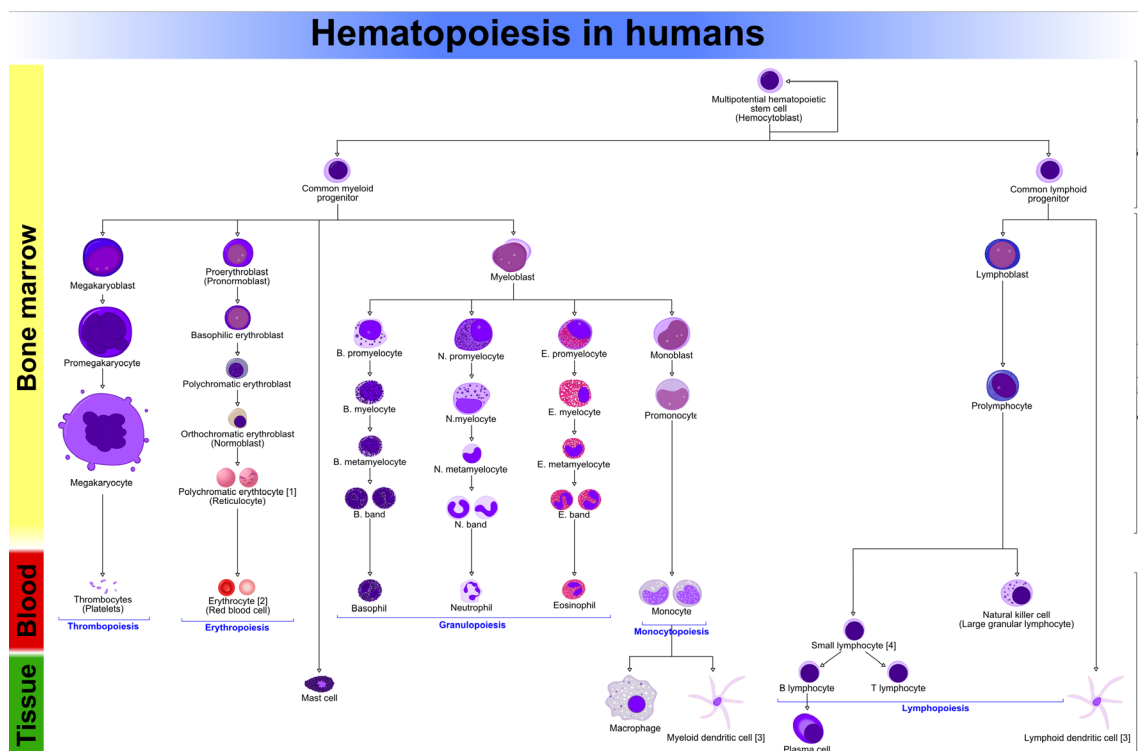


Figure 2.36: The procedure of hematopoiesis in humans.

#### 2.3.3.1 Bone Marrow

Bone marrow [41] is the flexible tissue in the interior of bones. In humans, during the process of hematopoiesis, erythrocytes are produced by cores of bone marrow in the heads of long bones. Statistically, bone marrow constitutes 4% of the total body mass of humans. The hematopoietic components of bone marrow produce approximately 500 billion blood cells per day. These cells use the bone marrow vasculature as a gate to the body's systemic circulation. Bone marrow's role is significant also in lymphatic system, producing the lymphocytes that support the body's immune system.

The bone marrow has two parts; the red marrow that consists mainly of

hematopoietic tissue, and the yellow marrow that is mainly made up of fat cells. Most of WBCs, RBCs and platelets arise from red marrow [Figure 2.37].

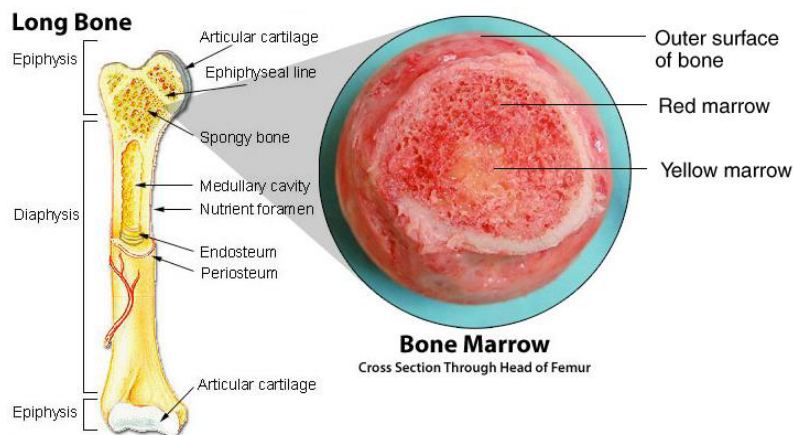


**Figure 2.37:** Structure of human bone marrow.

### 2.3.3.2 Hematopoietic Series

As HSC divides, its descendants begin to differentiate down to particular pathways toward mature blood cells, akin to traveling from a tree trunk, down progressively thinner branches, toward a particular leaf [Figure 2.36]. As these cells differentiate toward a particular cell type, they progressively lose their capacity to develop into the other cell types found in other branches of the differentiation tree.

The overall architecture of this differentiation tree largely matches the basic categories of blood cells with pathways dedicated to making erythrocytes (erythropoiesis), lymphocytes (lymphopoiesis), granulocytes (granulopoiesis), monocytes (monocytopoiesis), and platelets (thrombopoiesis). These basic pathways and the intermediate cell types that define that differentiation pathway are called as Hematopoietic Series [42].

### 2.3.3.3 Blasts

The first cell stages committed to any hematopoietic series are typically termed as "blasts". Blasts committed to the major differentiation pathways have some unique morphological characteristics; however, in general all blasts are fairly similar and appear as large cells with large nuclei. Blasts are also characterized by extremely rapid cell division rates. As differentiation progresses, the rate of cell division declines and the cells acquire the morphological characteristics unique to their ultimate mature cell type. The progressive development of these unique morphological characteristics is used to define stages of differentiation.

In certain pathological scenarios, such as acute leukemia, genetic lesions appear to block the differentiation of these blast cells, thus generating a neoplastic clone of undifferentiated cells with rapid mitotic rates.

### 2.3.4 Leukemia

Leukemia, is a group of cancers of the blood cells. It is the situation in which bone marrow fails to produce healthy and mature leukocytes and as a result, high numbers of abnormal leukocytes are entered the circulation of peripheral blood. These leukocytes are not fully developed and are called “blastic cells” or “leukemia cells” or simpler as “blasts”. Normally, the bone marrow barrier does not permit the presence of blastic cells in the peripheral blood. The suppression of this barrier may be present only in sever abnormal disorders, in which belong the leukemic abnormalities.

Symptoms may include bleeding and bruising problems, feeling tired, fever, and an increased risk of infections. Diagnosis is made by peripheral blood tests or bone marrow biopsy and examination under light microscope. Clinically and pathologically, leukemia is subdivided into a variety of large groups.

The first division is between its acute and chronic forms;

- Acute leukemia is characterized by a rapid increase in the number of immature blood cells. The crowding that results from such cells makes the bone marrow unable to produce healthy blood cells. Immediate treatment is required in acute leukemia because of the rapid progression and accumulation of the malignant cells, which then spill over into the peripheral blood and spread to other organs of the body. Acute forms of leukemia are the most common forms of leukemia in children.
- Chronic leukemia is characterized by the excessive buildup of relatively mature, but still abnormal, WBCs. Typically taking months or years to progress, the cells are produced at a much higher rate than normal, resulting in many abnormal white blood cells. Chronic leukemia mostly occurs in older people, but can occur in any age group.

The second division is between to which type of blood cell is affected;

- Lymphoblastic or lymphocytic leukemia takes place in a type of marrow cell that normally goes on to form lymphocytes, which are infection-fighting immune system cells. Most lymphocytic leukemias involve a specific subtype of lymphocyte, the B-Cells.
- Myeloid or myelogenous leukemia takes place in a type of marrow cell that normally goes on to form RBCs, some other types of WBCs, and platelets.

Combining these two classifications provides four main categories as presented in [Table 1].

Cell Type \ Form	Acute	Chronic
<b>Lymphocytic</b> (or Lymphoblastic) <b>Leukemia</b>	Acute Lymphoblastic Leukemia (ALL)	Chronic Lymphocytic Leukemia (CLL)
<b>Myelogenous</b> (or Myeloid) <b>Leukemia</b>	Acute Myelogenous Leukemia (AML)	Chronic Myelogenous Leukemia (CML)

**Table 1:** Major types of leukemic diseases.

### 2.3.4.1 Acute Lymphoblastic Leukemia

Acute Lymphoblastic Leukemia (ALL) [43] comprises 75% of acute leukemias, and is one of the most successfully treated type of childhood leukemia. Clinical symptoms include fever, weakness or feeling tired, bruising or bleeding easily, pinpoint spots under the skin from bleeding, bone pain, and loss of appetite. ALL occurs from an abnormality during the procedure of lymphopoiesis, where lymphoblasts, one of the first cells in lymphoid series, fails to differentiate further as in [Figure 2.38], get hyper-accumulated in bone marrow and finally enters the circulation of peripheral blood as in [Figure 2.39].

Currently for the classification of acute leukemias apart from the morphologic characteristics, cytochemical, cytogenetic, molecular methods and immunophenotyping are necessary. Morphologically according to French–American–British (FAB) system, three categories of Lymphoblasts are defined;

- L1 morphology blasts are usually smaller, with scant cytoplasm and inconspicuous nucleoli.
- L2 morphology blasts are larger and they demonstrate considerable heterogeneity in size, prominent nucleoli, and more abundant cytoplasm.
- L3 morphology blast are notable for their deep cytoplasmic basophilia, are large cells and frequently display prominent cytoplasmic vacuolation. They are morphologically identical to Burkitt’s lymphoma.

Approximately 85% of children with ALL have predominantly L1 morphology, 14% have L2, and 1% has L3 [44]. The limited heterogeneity of the cells in the light microscope makes usually difficult the morphological distinction of the ALL subtypes. In many cases, even the distinction of L1 lymphoblasts (which are the most common) from normal lymphocytes is also difficult.

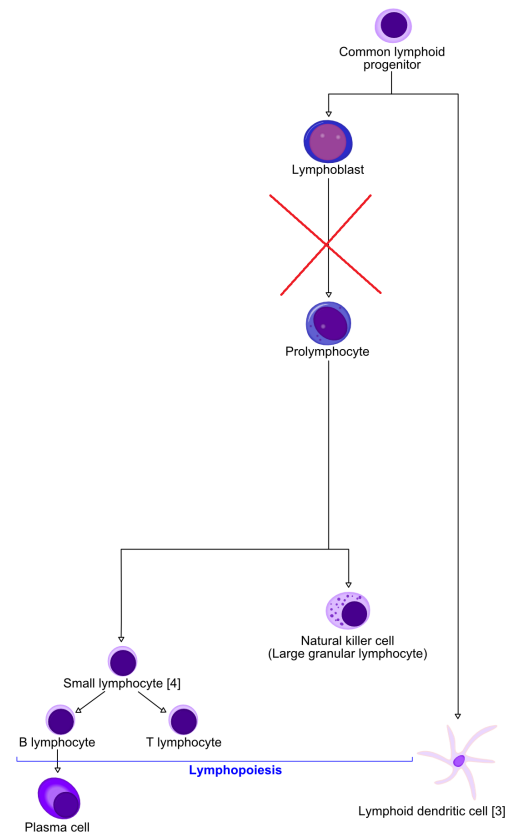


**Figure 2.38:** ALL abnormality in lymphoid series.

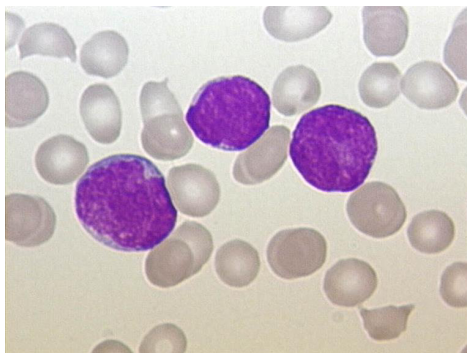


**Figure 2.39:** Stained lymphoblasts in peripheral blood smear.

#### 2.3.4.2 Chronic Lymphocytic Leukemia

Chronic Lymphocytic Leukemia (CLL) [4] is the most common type of leukemia in adults, comprising 25% of all cases diagnosed in North America and Europe. Its incidence increases with age with a median age of 55 years at diagnosis, and is more common in males. Patients are often asymptomatic at the time of diagnosis, especially in the early stages of the disease, but they are progressively more at risk for infection because of defects in humoral and cell-mediated immune systems. Clinical symptoms include bone marrow failure due to anemia, thrombocytopenia and neutropenia, lymphadenopathy and hepatosplenomegaly. In addition, systemic symptoms such as sweats, weight loss, thirst and bruising are common in CLL.

CLL develops primarily from a malignant clone of lymphocytes (specifically, B-Cells) as in [Figure 2.40], which are increased massively in peripheral blood (usually >85% of total WBC), a clinical case also known as lymphocytosis. Specifically, CLL lymphocytes are matured but morphologically abnormal, with very low cytoplasm to nucleus ratio, clumped nuclear chromatin and size comparable to erythrocytes [45]. In addition, the existence of smudged WBCs in peripheral blood smears, are typical in CLL as in [Figure 2.41].

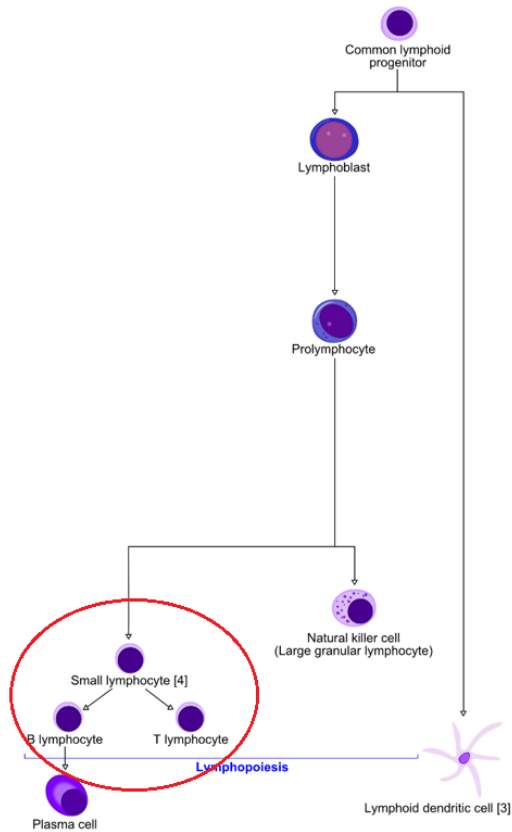


Figure 2.40: CLL abnormality in lymphoid series.

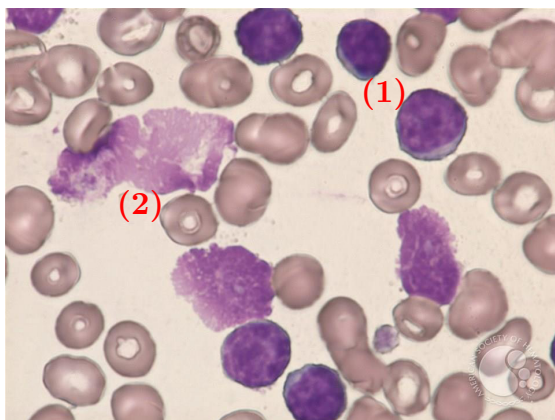


Figure 2.41: Abnormal lymphocytes (1) and smudge cells (2) in CLL.

### 2.3.5 Blood and Bone Marrow Samples Staining and Examination

The most common and widely used diagnostic procedure of blood abnormalities and diseases, such as leukemia, is through identification of morphologic characteristics and differential counting of blood cells. In order to achieve that, blood drawn from peripheral veins (i.e. peripheral blood) alongside with bone marrow samples are stained and examined under light microscopes.

#### 2.3.5.1 May Grünwald – Giemsa Stain

A carefully stained smear is fundamental for the observation and evaluation of blood's cellular morphology. Thus, Romanowsky stain (mainly used in United States) or May Grünwald – Giemsa stain (mainly used in European countries) are the most often utilized stains for peripheral blood and bone marrow samples.

The May Grünwald – Giemsa (MG-G) stain [4] combines the effect of acidic Eosin-Y and basic Methylene Blue (present in May Grünwald), alongside with the metachromatic basic stain of Azure-B (present in Giemsa, which also contains Eosin-Y) as in [Figure 2.42].

The purple color of the cells' nuclei, is due to the molecular interaction between Eosin-Y, Azure-B and Methylene Blue with the DNA complex. The basophil granules are negative charged so they attract the basic stains (Methylene Blue and Azure-B). Their final color after staining ranges between several shades of blue. In addition, the hemoglobin of the RBCs and the eosinophil granules are positive charged therefore they attract the acidic stain (Eosin-Y). Their final color after staining ranges between several shades of red. There also exists granules that attract portions of every stain of the solution (i.e., Eosin-Y, Azure-B and Methylene Blue). Their final color ranges between purple and red and are known as neutrophil grains [46]. The staining effects of MG-G stain are summarized in [Table 2].

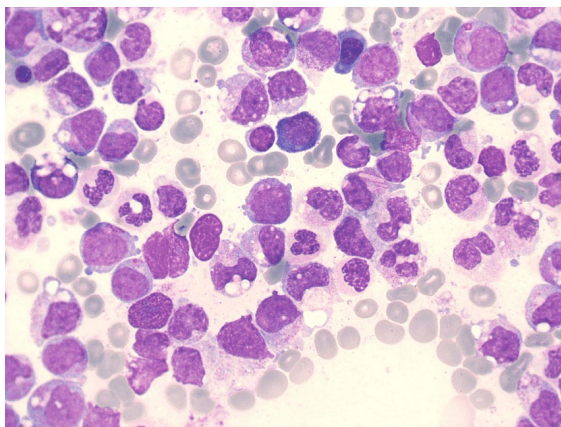


**Figure 2.42:** Peripheral blood smear stained with MG-G.

Component Stain	Nucleoli	Nucleus	Cytoplasm
Eosin-Y	---	Chromatin (DNA, RNA, Proteins)	Hemoglobin Eosinophil Granules Neutrophil Granules
Azure-B	RNA	Chromatin (DNA, RNA, Proteins)	Basophil Granules Neutrophil Granules
Methylene Blue	RNA	Chromatin (DNA, RNA, Proteins)	Basophil Granules Neutrophil Granules

**Table 2:** MG-G staining effects on blood cells components.

### 2.3.5.2 Microscopy Examination Procedure

After staining protocol, samples are ready for examination under microscope following a predetermined procedure. During this process [4]:

- First, a low magnification objective (5x – 10x) is selected, to achieve a large field of view from the smear. The smear is scanned horizontally, in order to locate the point where monolayer of blood cells begins (i.e. areas where blood cells are not overlapped) [Figure 2.44].
- Then, a higher magnification objective (20x – 30x) is selected, to locate areas with relatively high concentration of WBC.
- After locating desired region of interest, a high magnification objective (>40x) is selected, in order to have a clear and detailed image of cells' morphology.
- Finally, the last step is repeated, in a “meander-like” movement [Figure 2.43], until the whole smear gets scanned.

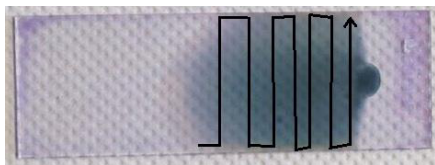


**Figure 2.43:** Meander-like movement, during examination of blood smears.

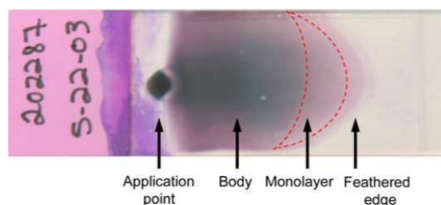


**Figure 2.44:** Examination areas of a blood smear.

## 3 Method for Measuring and Enhancing Imaging Resolution in Microscopy

As explained in *Chapter 2*, every electro-optical imaging system (such as light or fluorescence microscopes), has limited imaging resolution due to physical phenomena (such as diffraction), as well as due to technical imperfections (e.g. poor focus, color aberrations, etc.).

However, unsupervised and computational diagnostic procedures that are based on examination of cells' morphology and pixel-level spectral imaging, as the one developed in this thesis, requires spectral and color images of superior resolution, in order to provide precise and highly accurate analytical and classification results. For those reasons, a novel method was developed for measuring and afterwards using that knowledge for enhancing microscopy imaging, in terms of optical resolution.

### 3.1 MTF Estimation via Slanted Edge Analysis

The standardized method in industry and academia [47] for measuring Modulation Transfer Function of EO imaging systems is based on the analysis of slanted edge [12]. As slanted edge is defined a resolution test target, originally developed by United States Air Force, which contains a dark squared area with sharp edges tilted in front of a bright background and with respect to the horizontal and vertical imaging planes. The optimal orientation [47] of the slanted edge is between  $2^\circ$  to  $5^\circ$  degrees [Figure 3.1].

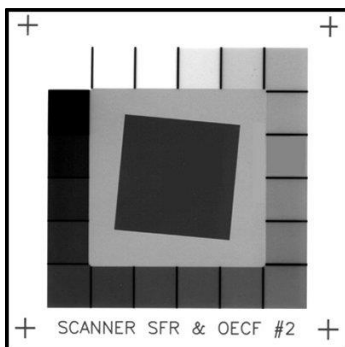


**Figure 3.1:** Example of a slanted edge target.

#### 3.1.1 Method's Analysis

The underlying idea behind analysis of slanted edge can be most clearly seen by considering an example from area of electronics. The MTF (in the sense

of a plot of modulation against spatial frequency) is quite parallel to the matter of the “frequency response” of an electronic amplifier, where the gain of the amplifier is calculated as a function of frequency.

The classical technique for determining the frequency response involves presenting the amplifier with signals of known voltage at different frequencies, and in each case, measuring the output power. But there is a way to determine this with a “one shot” test by submitting to the amplifier what is called an impulse. When this is done, a certain waveform comes out of the amplifier. It is called the impulse response of the amplifier and from this waveform is determined the entire voltage gain function (gain as a function of frequency) because the impulse contains energy at all frequencies (in theory, up to infinity), with a uniform distribution.

Now, if the Fourier transform of the output waveform is taken, the result is a description of the frequency content of that waveform. Given that the input signal contains “all frequencies”, uniformly, that description will be the voltage gain function (or “voltage frequency response”). However, because an “impulse response” is impractical to get applied on an electronic system, variation of that theme is used, where instead of using an impulse as input it is used a step function.

Similarly, in case of EO imaging systems, a “zero-width” bright line, is the optical equivalent of the impulse in the electronic scenario. Unless the EO system has “infinite resolution”, the image of that line on the focal plane will be a pattern of non-zero width, across which the illuminance varies in some way. This is called the Line Spread Function (LSF) of the EO system. By taking its Fourier transform, occurs the modulation as a function of spatial frequency (i.e., the MTF).

However, this “zero width” line is impractical to make, so an appropriate test target is used that is black up to a straight-line boundary and white beyond it - the optical equivalent of the electrical step function (i.e. a sharp edge). The plot of illuminance across that boundary is called the Edge Spread Function (ESF) of the EO system. By measuring this illuminance pattern and taking its first derivative, it occurs the same LSF that described previously. Afterwards by taking its Fourier transform, it occurs again the MTF but through a different way, as depicted in [Figure 3.2].

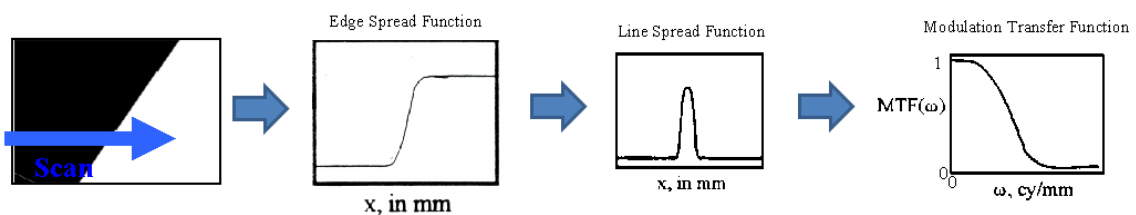


**Figure 3.2:** Calculation procedure of MTF using a slanted edge target.

One last challenge to address is the fact that the imaging sensor is not capable to discern illuminance pattern of the ESF with sufficient resolution. As depicted in

[Figure 3.3], a hypothetical ESF profile (left) that is projected on to an imaging sensor plane (right), lacks serious precision to its representation, due to the finite number of pixels alongside direction of edge pattern. One way to overcome this problem is by increasing the number of pixels, in order to achieve higher resolution.

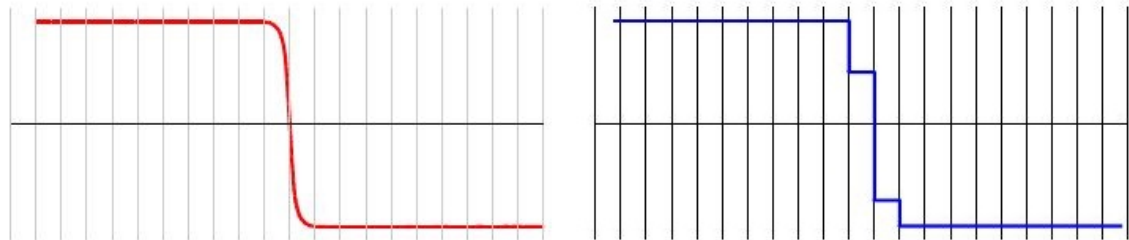


**Figure 3.3:** Real edge (left) and imaged edge (right).

Alternatively, using a slanted version of the edge [Figure 3.4] (i.e. the case of slanted edge analysis) gives the ability to project a different aspect of the edge on every row of pixels (assuming that the edge is identical alongside its vertical dimension). Afterwards, binning pixels vertically into equal sized groups and using these groups as new pixel intensities [Figure 3.4], gives a super-resolved estimation of the ESF, which is sufficient for accurate estimation of system's MTF.

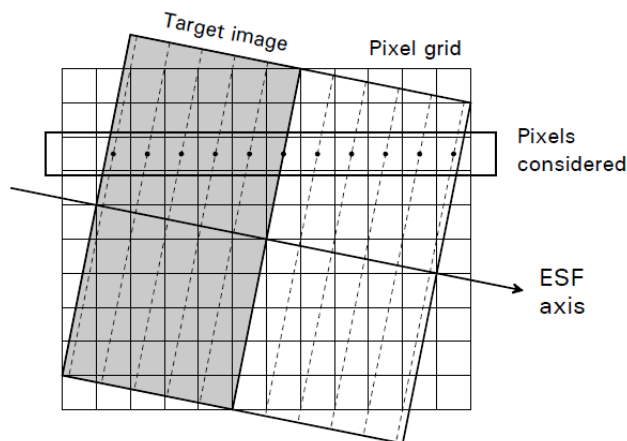


**Figure 3.4:** Projection of a slanted edge on sensor plane.

### 3.1.2 Method's Algorithm

The algorithm of slanted edge MTF estimation method is consisted of ten different steps as presented in the flowchart of [Figure 3.6].

Initially, the algorithm receives as inputs a captured image of the slanted edge target, on which a desired Region of Interest (ROI) is selected, in order to apply the analysis, as well as the pixel size of the sensor, in order to calculate the Nyquist frequency of the system (i.e. the upper resolution limit). An appropriate ROI is

selected by the user, that contains an equally spaced black and white area of the imaged target, with slope between  $2^\circ$  to  $5^\circ$ , contrast of 1:4 minimum and without saturated pixels. Before proceeding to calculations, if the target's image is colored, the luminance information must be extracted (i.e., convert it to grayscale), using the equation of {3.1}.

$$Luminance(x, y) = 0.213 \cdot R(x, y) + 0.715 \cdot G(x, y) + 0.072 \cdot B(x, y) \quad (3.1)$$

where  $x, y$  are pixels coordinates and  $R, G, B$  are the channels of the color image. Afterwards, the 1<sup>st</sup> derivative of the selected ROI is computed, by applying a 1D kernel {3.2} on every row of pixels, in order to find the pixels where the edge is located.

$$1^{st} Derivative Kernel = [-0.5 \quad 0.5] \quad (3.2)$$

Since the pixels of the edge are not located on the same column (because the edge is slanted) and that the 1<sup>st</sup> derivative does not return only one non-zero value alongside the direction of the edge, then the centroid of each row of pixels is computed as in {3.3}, and a line is fitted through the locations of these centroids.

$$Centroid_i = \frac{\sum_1^j i \cdot pixel_{intensity(i,j)}}{\sum_1^j pixel_{intensity(i,j)}} \quad (3.3)$$

where  $i$  are rows and  $j$  are columns of pixels in edge's image.

Using this line to locate the edge, the pixels' values on both sides of the edge are projected as a 1D plot along the edge direction and binned in four groups of pixels for every column of the selected ROI. This projection represents a super-resolved plot of the edge, which correspond to the ESF. Then, applying again the 1<sup>st</sup> derivative kernel of {3.2} on this ESF, the corresponding LSF is extracted. Finally, calculating the Discrete Fourier Transform of the LSF and taking its modulus, gives the desired MTF estimation. Those steps are depicted via images and plots of [Figure 3.5].

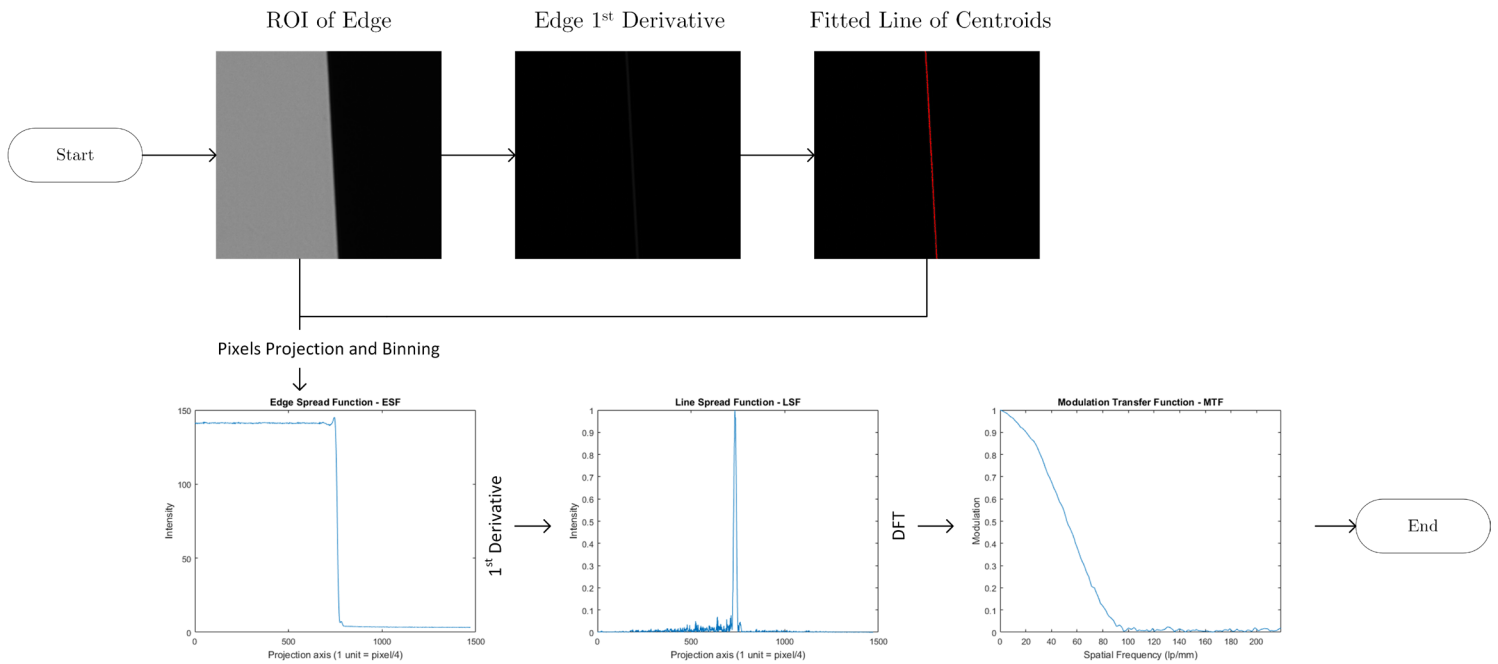


**Figure 3.5:** Visual representation of MTF estimation algorithm.

It must be noted that an important parameter for the correct estimation of MTF in terms of spatial frequencies, is that the total magnification factor of the system must be taken into consideration. MTF without considering magnification represents the transferred modulation in terms of spatial frequency on the image plane (i.e. sensor plane). In order to “translate” those spatial frequencies to the real plane (i.e. object/target plane), spatial frequencies must be multiplied with the total magnification factor of the system.

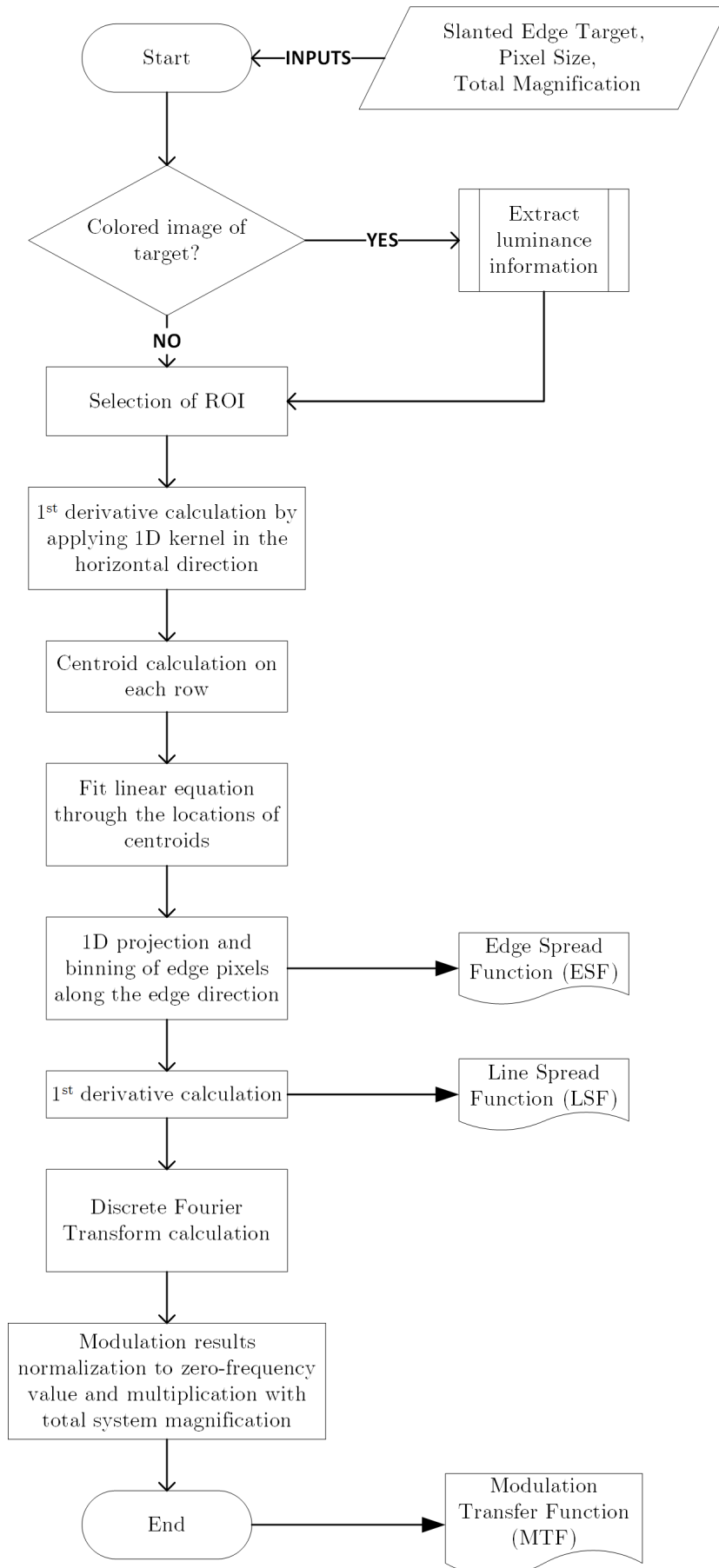


Figure 3.6: Flowchart of slanted edge MTF algorithm.

### 3.1.3 Algorithm Implementation

The algorithm of slanted edge MTF estimation method has been developed as a standalone program, using Mathworks Matlab R2016b. The program receives as inputs the desired image of the slanted edge target, the pixel size of the imaging sensor and the total magnification factor of the EO system.

Afterwards, the user is called to define an appropriate ROI on the target's image and then the program executes the algorithm of subsection 3.1.2., in order to calculate the MTF curve of the system. Alongside with the MTF curve, the resolved resolutions of the system at 50% and 15% of modulation (in lp/mm), on object plane (i.e. on target) as well as on image plane (i.e. on sensor), are calculated. An example of the execution flow of the developed program is depicted in [Figure 3.7].

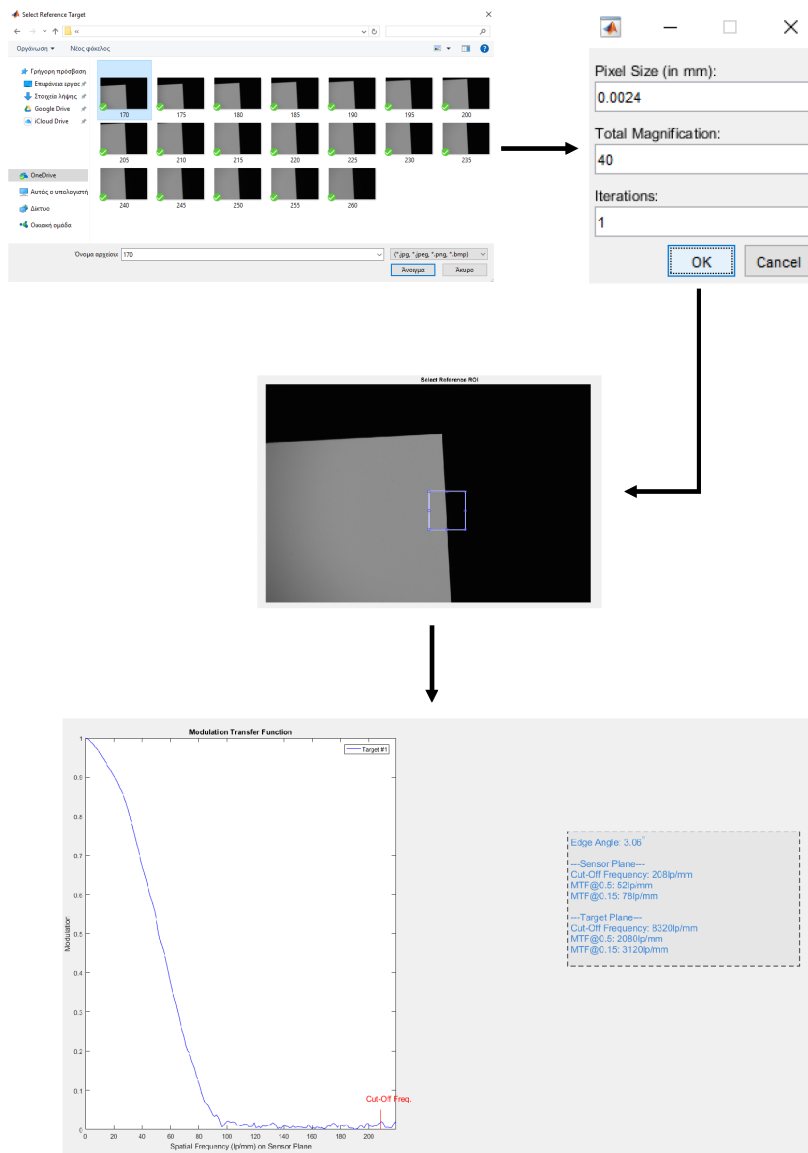


Figure 3.7: Execution flow of slanted edge MTF program.

### 3.1.4 Evaluation of Implementation

For the evaluation of the accuracy of the developed program, a series of experimental measurements were conducted, using a real scientific light microscope, with known resolution through manufacturer's datasheet. The program's accuracy was examined in terms of calculated resolution and measurements repeatability with existence of noise.

The microscope used was a Zeiss Axio Scope A1 Series [Figure 3.8] combined with three Zeiss EC Plan-Neofluar objectives of 5x, 10x and 40x magnification [Figure 3.9]. As target, a custom-made slanted edge MTF target for microscopes was used, manufactured by Thor Labs [Figure 3.10]. This target had a 5° slanted and L-Shaped pattern of edge that is ISO 12233:2014 compatible. It was printed on a soda lime glass using photolithography method and chrome-on-glass as design material, that allows a printing precision of 0.1 $\mu$ m enough even for a 40x objective with 0.5 $\mu$ m resolving power. This target was used for every slanted edge MTF measurement with microscope, in this thesis.



**Figure 3.8:** Zeiss Axio Scope A1 Series.



**Figure 3.9:** Zeiss EC Plan-Neofluar objectives.



**Figure 3.10:** Custom-made slanted edge MTF target for microscopes by Thor Labs.

According to manufacturer’s datasheet [48], the microscope’s maximum resolutions (where MTF tends to zero) in  $\mu\text{m}$  and lp/mm on object plane (i.e. on target) as well as on image plane (i.e. on sensor) for every tested objective are summarized in [Table 3].

Objective \ Resolution	$\mu\text{m}$ (object plane)	lp/mm (object plane)	$\mu\text{m}$ (image plane)	lp/mm (image plane)
Zeiss EC Plan-Neofluar 5x	1.8	555.56	9	111.12
Zeiss EC Plan-Neofluar 10x	1.1	909.09	11	90.9
Zeiss EC Plan-Neofluar 40x	0.5	2000	20	50

**Table 3:** Resolutions of Zeiss EC Plan-Neofluar objectives based on manufacturer.

In comparison, the maximum resolutions estimated using the developed program are summarized in [Table 4]. As depicted, the estimated resolutions are almost identical to those in manufacturer’s datasheet, with a maximum deviation of 8.3% for maximum magnification power. Those minor deviations are expected because the program calculates as maximum resolvable power the frequencies where MTF equals to 5%, which expected to be slightly less than manufacturer’s calculated resolution (where MTF tends to zero).

Objective \ Resolution	$\mu\text{m}$ (object plane)	lp/mm (object plane)	$\mu\text{m}$ (image plane)	lp/mm (image plane)
Zeiss EC Plan-	1.91	523	9.55	105

Neofluar 5x				
Zeiss EC Plan-Neofluar 10x	1.13	880	11.3	88
Zeiss EC Plan-Neofluar 40x	0.54	1840	21.6	46

**Table 4:** Measured resolution of Zeiss EC Plan-Neofluar objectives with developed program.

Finally, the developed program has been tested for the repeatability of its measurements with existence of noise. The analysis ran in five captured frames of the same target for every one of the three objectives. Those frames were captured with 30 seconds delay between each other and all the parameters of the experimental setup were unaffected.

As depicted in [Figure 3.11], [Figure 3.12] and [Figure 3.13], the calculations of MTF are almost identical between different frames (every color represents a different frame) and any differences exist for modulation values greater than 5%, where the fine details of the image are irresolvable and any information are due to the sensor’s electronics noise.

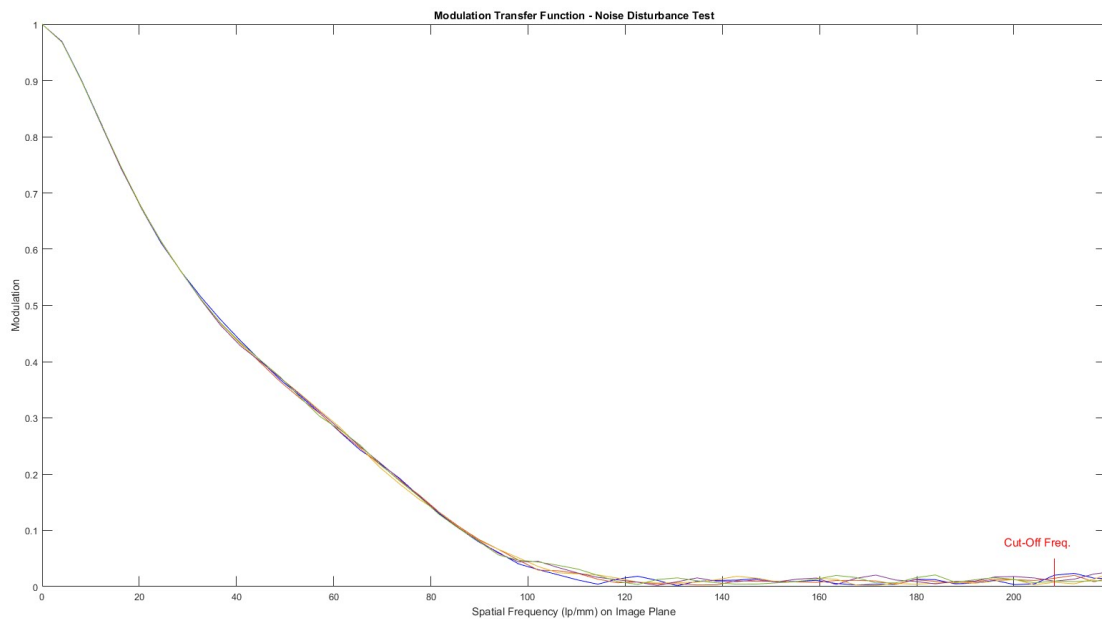


**Figure 3.11:** MTF measurements repeatability for 5x objective.

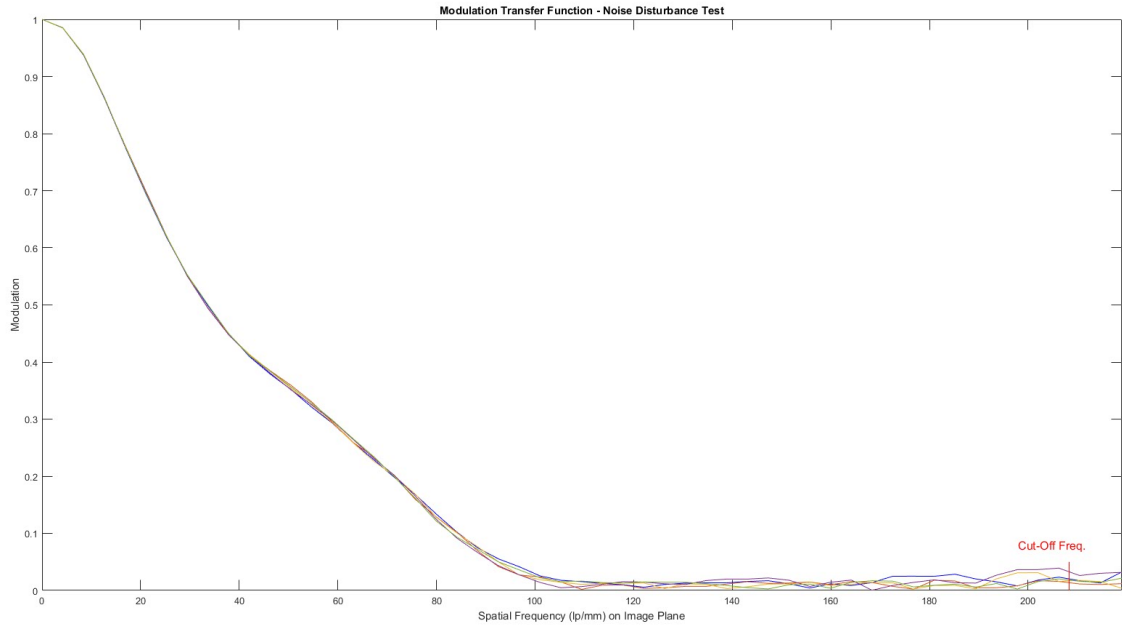


Figure 3.12: MTF measurements repeatability for 10x objective.

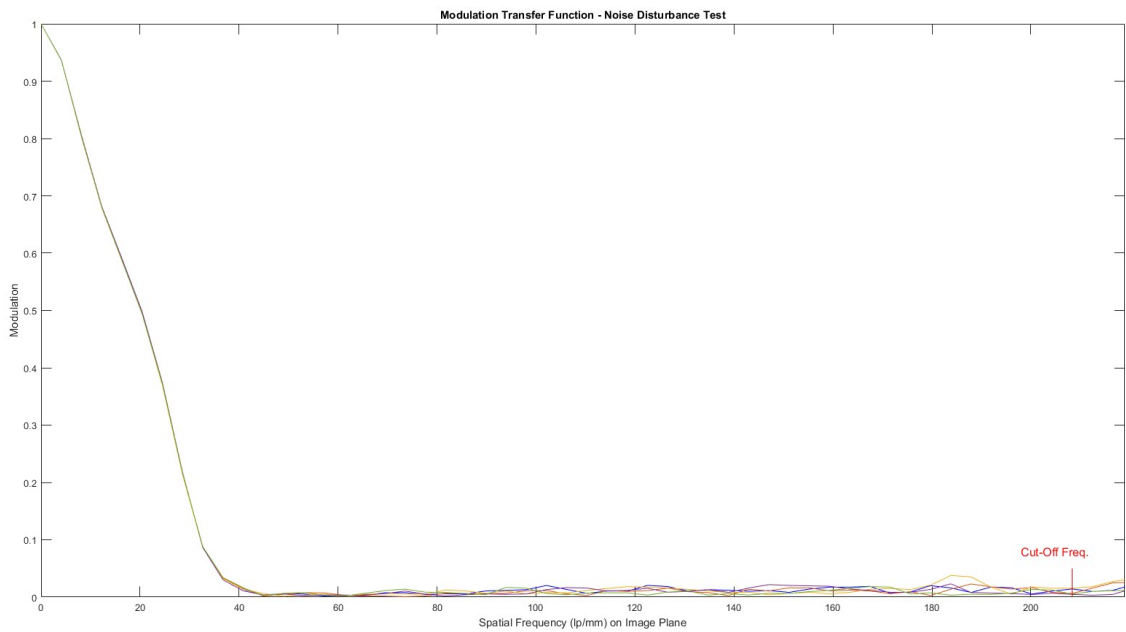


Figure 3.13: MTF measurements repeatability for 40x objective.

### 3.2 Deconvolution for Enhancing Microscopy Imaging Resolution

Since its introduction in 1983, deconvolution microscopy has become a key image processing tool for visualizing the cellular structures of fixed and living specimens in three dimensions and increase microscopes imaging at a sub-resolution scale. The last 20 years have seen the development of many different

applications based on deconvolution microscopy, including a wide variety of optical setups and deconvolution methods, such as Wiener filtering, nearest neighbors' estimation algorithms, constrained iterative algorithms, statistical algorithms and blind deconvolution algorithms [49].

As deconvolution microscopy provides, in essence, a means of overcoming the limits and distortions of optical microscopy, in this thesis Wiener deconvolution is employed, as a non-iterative and fast algorithm to enhance microscopy images, a key preparatory step for acquiring spectral and color images of superior resolution.

A crucial parameter for the characterization of any EO imaging system and a preliminary task for image deconvolution in microscopy, is the appropriate determination of PSF [49]. The PSF can be determined in three ways, namely experimental, theoretical and analytical [50]. In the experimental approach, fluorescent sub-resolution microspheres are used for this purpose [51], a method applicable only to fluorescence and confocal microscopy. This is methodologically difficult to do and such microspheres are not usable in brightfield and darkfield microscopes. The theoretical determination, in turn, responds to a set of mathematical equations that describe the physical model of the optics, as studied indicatively in [52] [53] [54]. The model's parameter values are filled with the instrument data-sheet and the capture conditions. The modeling of certain aberrations and the absence of noise are its main advantages, however complex optical setups cannot be modeled accurately. The third way to determine PSF was originated from parametric blind deconvolution algorithms; it has the advantage of estimating the model parameters from real data, but again some knowledge about the PSF is necessary [55].

Thus, we developed and present, for the first time in the relevant literature to the best of our knowledge, a novel method for extracting the complete two-dimensional PSF of an optical microscope experimentally, based on a single measurement of one-dimensional MTF curve, alongside with the experimental compensation of noise effects during the process of deconvolution.

### **3.2.1 Wiener Deconvolution Model**

Wiener deconvolution [56] is an application of the Wiener filter to the noise problems inherent in deconvolution. It is utilized in the frequency domain, given by the DFT of the image and attempts to minimize the impact of deconvolved noise at frequencies, which have a poor signal-to-noise ratio (SNR).

The mathematical formulation of the Wiener filter is defined as in {3.4}:

$$P(u, v) = \frac{1}{OTF(u, v)} \cdot \left[ \frac{|OTF(u, v)|^2}{|OTF(u, v)|^2 + K_{NSR}} \right] \quad (3.4)$$

where  $OTF(u, v)$  is the two-dimensional optical transfer function of the system (i.e. the PSF in the frequency domain),  $u$  and  $v$  are the frequency coordinates and  $K_{NSR}$  is an a priori calculated constant related to the noise-to-signal ratio of the EO imaging system.

The operation of Wiener deconvolution is relative easy to be perceived. Equation in {3.4} contains two fractions; the left fraction outside brackets is the ideal inverse filter, as Wiener filter tries to minimize the root mean square error between the original and the restored image. As an accurate estimation of OTF is required, this RMSE error can be minimized through simple inverse filtering.

The right fraction inside brackets is for suppression of noise's effect. Wiener filter is unable to reconstruct frequency components that have been degraded by noise, but only to suppress them. As the noise increases, the noise-to-signal ratio increases too (i.e., the  $K_{NSR}$ ). Then, the term inside the square brackets drops but inversely proportional to the magnitude of frequency components.

High signal-to-noise ratio will result to high attenuation in corrupted frequencies and low signal-to-noise ratio will result to low attenuation. However, if there is zero noise (i.e. zero noise-to-signal ratio), the term inside the square brackets always equals to 1, which means that the Wiener filter is simply the inverse of the system, as expected.

Finally, the restored image is defined as the Inverse Discrete Fourier Transform of {3.5}:

$$R(u, v) = I(u, v) \cdot P(u, v) \quad (3.5)$$

where  $R(u, v)$  is the restored image in frequency domain and  $I(u, v)$  is the degraded image in frequency domain.

### **3.2.2 Two-Dimensional OTF Extraction Method**

The MTF determined by slanted edge analysis is one-dimensional. However, to restore images based on PSF compensation (or OTF according to {2.1}, if working in frequency domain), a two-dimensional approach must be employed. As explained in subsection 2.1.2., in cases of well-corrected optical systems (i.e. mainly existence of defocus and color aberrations) that are illuminated by incoherent light sources, the OTF is considered as symmetric and real for all spatial frequencies and thus, the imaginery part of OTF is negligible [5]. Based on that, one-dimensional MTF equals to one-dimensional OTF and

thus, the two-dimensional OTF can be determined by multiplying the vertical-orbit MTF by horizontal-orbit MTF dectractively [57], using {3.6}:

$$OTF(u, v) = MTF_v \cdot MTF_u \tag{3.6}$$

where  $MTF_u$  is the MTF value at spatial frequency  $v$  and  $MTF_v$  is the MTF value at spatial frequency  $v$ . Due to OTF symmetry, vertical and horizontal MTFs are equal each other.

Before multiplication of {3.6} the MTF values must be mirrored beyond the Nyquist frequency, as OTF spectrum is symmetrical around its DC component (i.e. its zero frequency). In addition, the MTF values below 5% of modulation are smoothed with smoothing spline [59], as any fluctuations in MTF values are existed due to the influence of noise. The steps of this method are presented in [Figure 3.14].

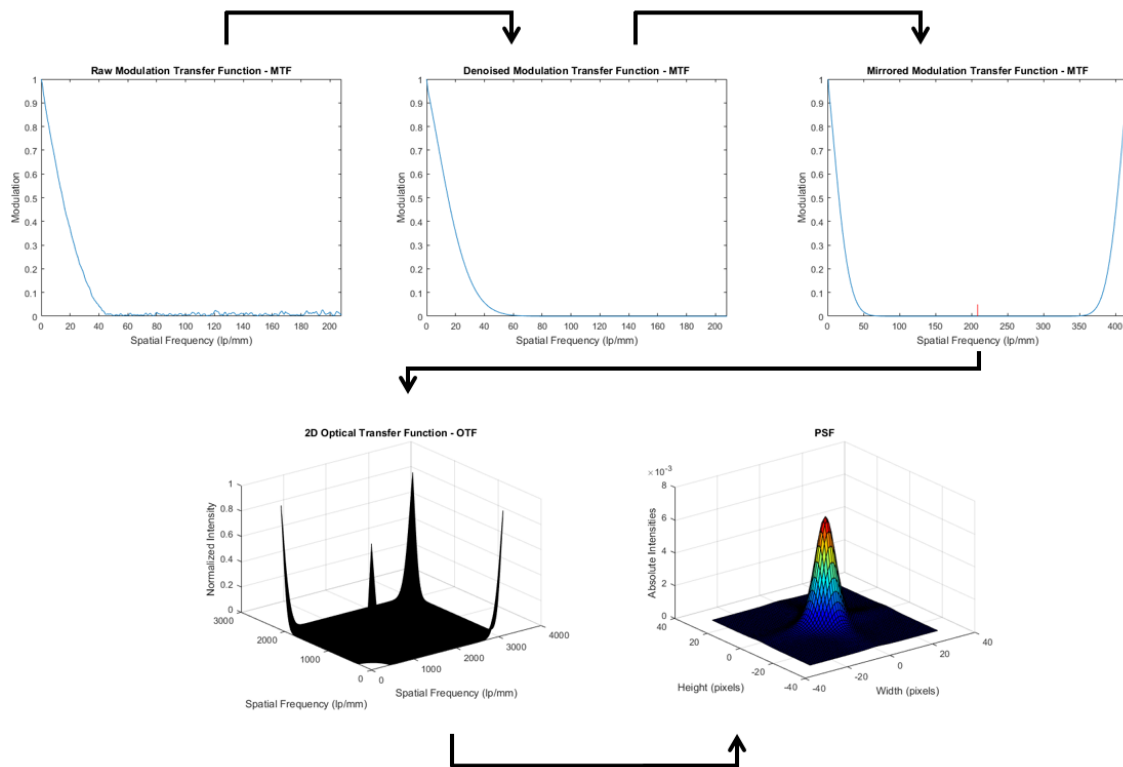


Figure 3.14: Visual representation of 2D OTF estimation method.

### 3.2.3 Noise to Signal Ratio Estimation Method

The amount of noise in microscopy images, can be estimated using the following experimental approach. It is known that NSR is defined as the ratio of

power of a signal (meaningful information) and the power of background noise (unwanted signal), as in {3.7}.

$$NSR = \frac{P_{noise}}{P_{signal}} \quad (3.7)$$

In the case of imaging, undesirable signal is the deviation of pixel values due to imaging sensor's noise and the meaningful information is the pixel values of the imaged object. Thus, an alternative approach to definition of NSR is as the reciprocal of the coefficient of variation, i.e., the ratio of standard deviation to mean, of an imaged test field [58], as in {3.8}.

$$NSR = \frac{\mu}{\sigma} \quad (3.8)$$

where  $\mu$  is the signal mean or expected value and  $\sigma$  is the standard deviation of the noise. In this thesis, a direct way to calculate this ratio is by imaging an empty field through microscope, where the signal mean is simply the average value of pixels intensity of the empty imaged field and standard deviation of the noise is the standard deviation of the pixels intensities around the mean value, due to the sensor's noise. One important point for the accuracy of the measurements is that the imaged field must be flatted (i.e., there must be no variations to pixels intensities due to different distribution of illumination, field of view, etc.). After calculating NSR using this method, is simply employed in equation {3.4} of Wiener Filter as  $K_{NSR}$  constant.

### **3.2.4 Implementation and Results**

The method described previously was developed as a standalone procedure, using Mathworks Matlab R2016b, combined and tested using a prototype microscope setup, with brightfield, spectral and fluorescence imaging capabilities along with a zoom-based magnification via a single objective. This is the *Lumnia Series BF-FL-Hem Multi-Modal Microscope* developed by *Holoptica P.C.* and depicted in [Figure 3.15].

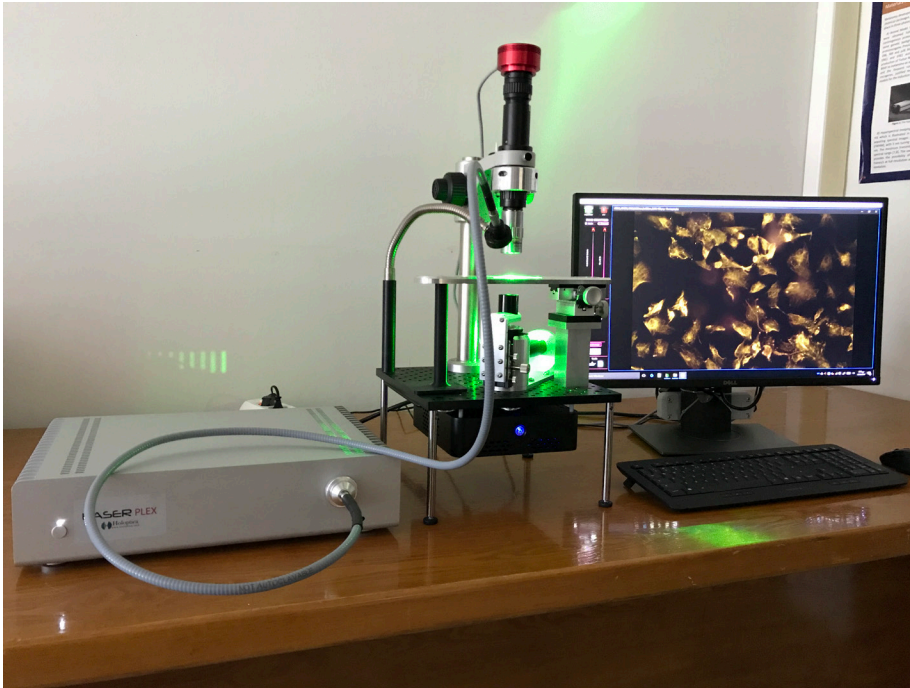


**Figure 3.15:** Lumnia BF-FL-Hem Multi-Modal microscope by Holoptica P.C.

This microscope provides together with the captured images, information about the overall magnification power of the system, the camera settings (i.e., gain in dB and shutter in ms) and the wavelength of illumination. In the developed program, the standalone procedure was calibrated for different magnifications, wavelengths and camera settings, in order to provide completely unsupervised deconvolution results.

#### **3.2.4.1 OTF Calibration over Magnifications and Wavelengths**

Calibration was performed for optical magnifications ranging from 10x up to 24x, in which the fine details retrieved by the *Lumnia Microscope* are visible for further resolution enhancement and the Field of View (FOV) is enough to have flat illumination across the whole image.

The calibration of the proposed method is based on *a priori* calculated one-dimensional MTF curves, across consequence magnifications and for every wavelength of illumination available from the microscope's LED light source. Those MTF curves are stored into look-up tables, that are available during initialization phase of method's execution, and based on that the corresponding two-dimensional OTF is calculated using {3.6}.

The one-dimensional MTF curves had been estimated using the implementation of subsection 3.1.3 and the custom-made slanted edge of [Figure 3.10]. MTF was measured experimentally, for magnifications between 10x - 24x and using a step of 0.5x approximately, as depicted in [Figure 3.16]. Afterwards, based on measured modulation values and for every spatial frequency up to Nyquist Limit, the

intermediate values of modulation were estimated, using cubic spline data interpolation [59]. This procedure provided a detailed estimation of MTF curve for every possible magnification of the microscope (specifically, for every different ADC value of microscope's zoom sensor).

In addition, this calibration procedure had been executed for every wavelength of illumination separately (i.e., for 465nm, 505nm, 530nm, 600nm, 640nm, 685nm), as well as for every one of the three sensor's channels using broadband white LED. Finally, before storing MTF curves into look-up tables, an appropriate smoothing spline [59] was applied for frequencies where modulation was less than 5%, in order to reduce the effect of noise in MTF measurements as explained in subsection 3.1.4, while preserving MTF dropping trend.

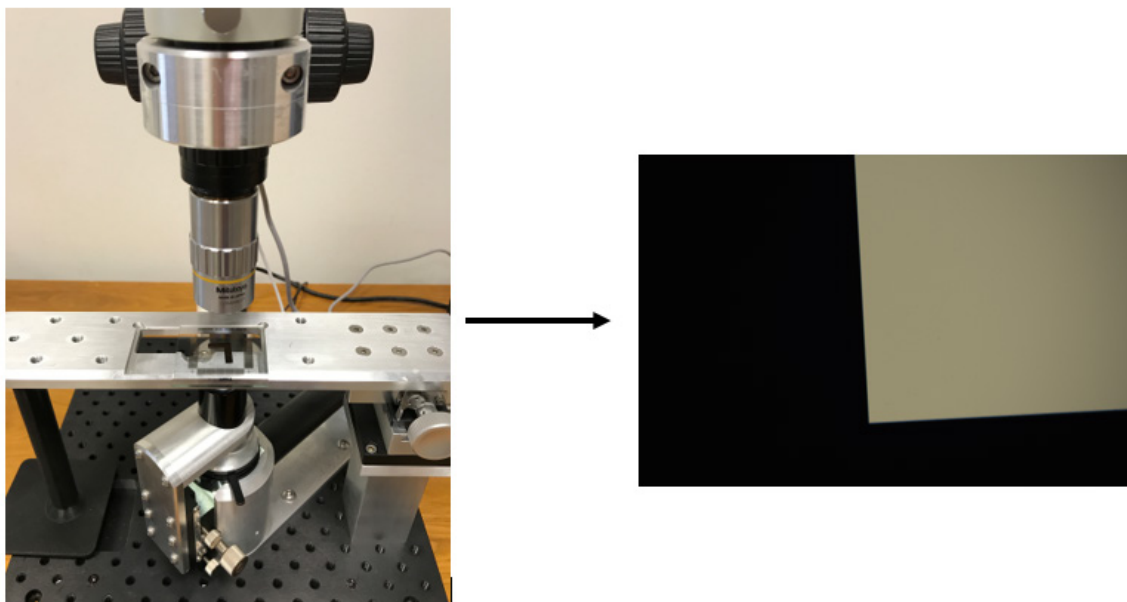


**Figure 3.16:** Measuring of MTF on Lumnia Microscope.

The outcome of the described calibration procedure were six two-dimensional look-up tables (i.e., one for every monochromatic LED), where rows are the modulation values for frequencies up to Nyquist Limit and columns are the different magnifications of the microscope. An additional three-dimensional look-up table was calculated for the broadband white LED, where the third dimension represents the three different channels of the imaging sensor. An example of measured MTF curves between 10x to 24x with the corresponding interpolated MTF curves using the proposed procedure, are depicted in [Figure 3.17] and [Figure 3.18] respectively.

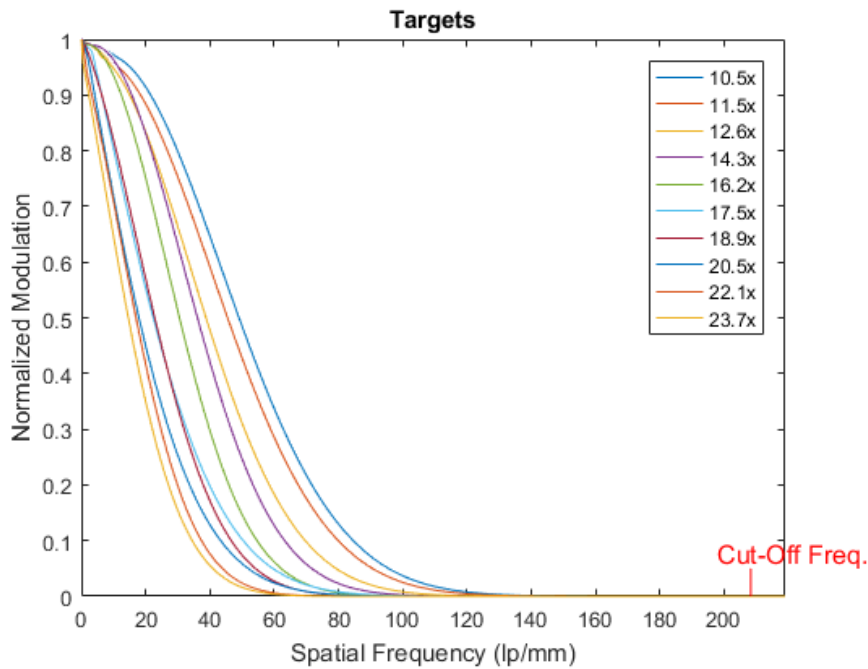


**Figure 3.17:** Measured MTF curves across different magnifications, using 530nm LED.

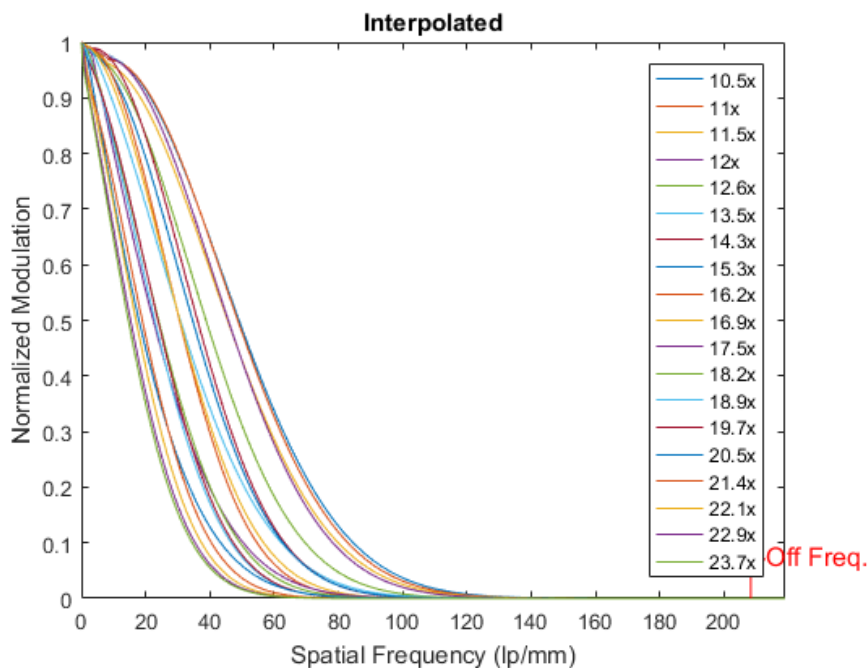


**Figure 3.18:** Interpolated MTF curves across different magnifications, using 530nm LED.

### 3.2.4.2 $K_{NSR}$ Calibration over Camera Sensor Gains and Channels

As explained in subsection 3.2.1, Wiener filter contains an appropriate additive parameter for minimizing the impact of deconvolved noise at frequencies where NSR is poor. This parameter, the  $K_{NSR}$  constant, had been estimated using the method described in subsection 3.2.3.

The calibration is based on *a priori* measured values of  $K_{NSR}$  for different gain settings of the imaging sensor, which is the main source of noise [60]. In addition, as the imaging sensor of *Lumnia Microscope* is colored and it is known that every channel has different response to gain settings (i.e., different amount of noise per channel), the corresponding  $K_{NSR}$  had been measured across consequence gain settings, for every different wavelength of illumination and for every sensor's channel separately. Those  $K_{NSR}$  values are stored into look-up tables again, that are available during deconvolution phase of execution.

$K_{NSR}$  was measured experimentally, for gains between 0dB – 200dB and using a step of 10dB. Afterwards, based on measured  $K_{NSR}$  values, the intermediate values were interpolated, using cubic spline data interpolation [59]. This procedure provided a detailed estimation of  $K_{NSR}$  curve for every possible gain setting of the microscope's imaging sensor.

The outcome of the described calibration procedure were seven two-dimensional look-up tables again (i.e., one for every monochromatic LED and one for the broadband white LED), where rows are the  $K_{NSR}$  values for gain settings up to 200dB and columns are the three different channels. An example of measured  $K_{NSR}$  curves between 0dB to 200dB using the broadband white LED, is depicted in [Figure 3.19].

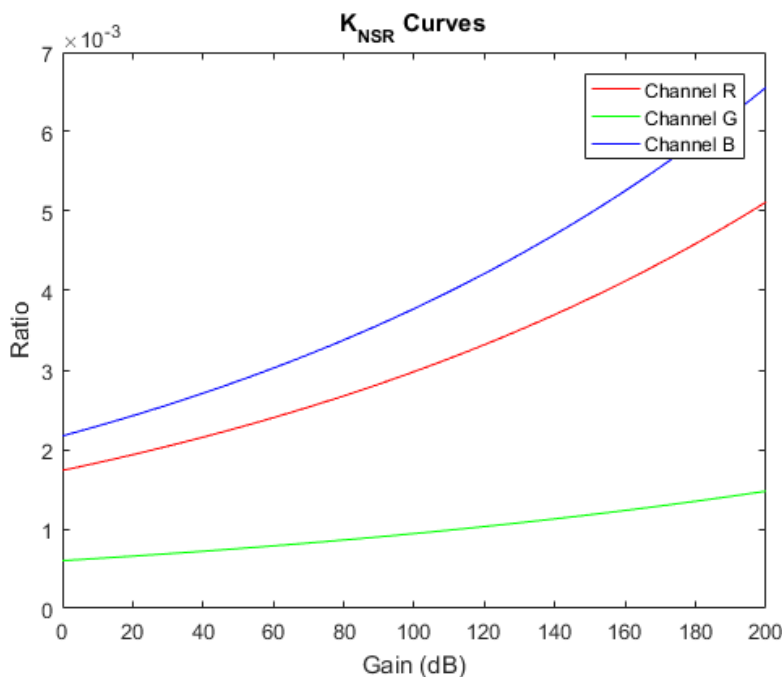


**Figure 3.19:** Measured  $K_{NSR}$  curves across different gain settings, using broadband white LED.

### 3.2.4.3 Method Implementation and Flowchart

The developed program, except its usability as an add-on procedure via Matlab functions callbacks, it provides a graphical user interface [Figure 3.20]. The

program receives as input the desired image for resolution enhancement, that was captured using the *Lumnia Microscope*. It retrieves the corresponding illumination wavelength, gain setting and the total magnification factor of the system during acquisition, that are stored in a text file with the image. Afterwards, the program executes the procedure as depicted in flowchart of [Figure 3.21] and it displays the deconvolved image alongside with the initial image. Finally, it provides the options to store the result and to visualize the corresponding 3D surface plot of PSF used during deconvolution.

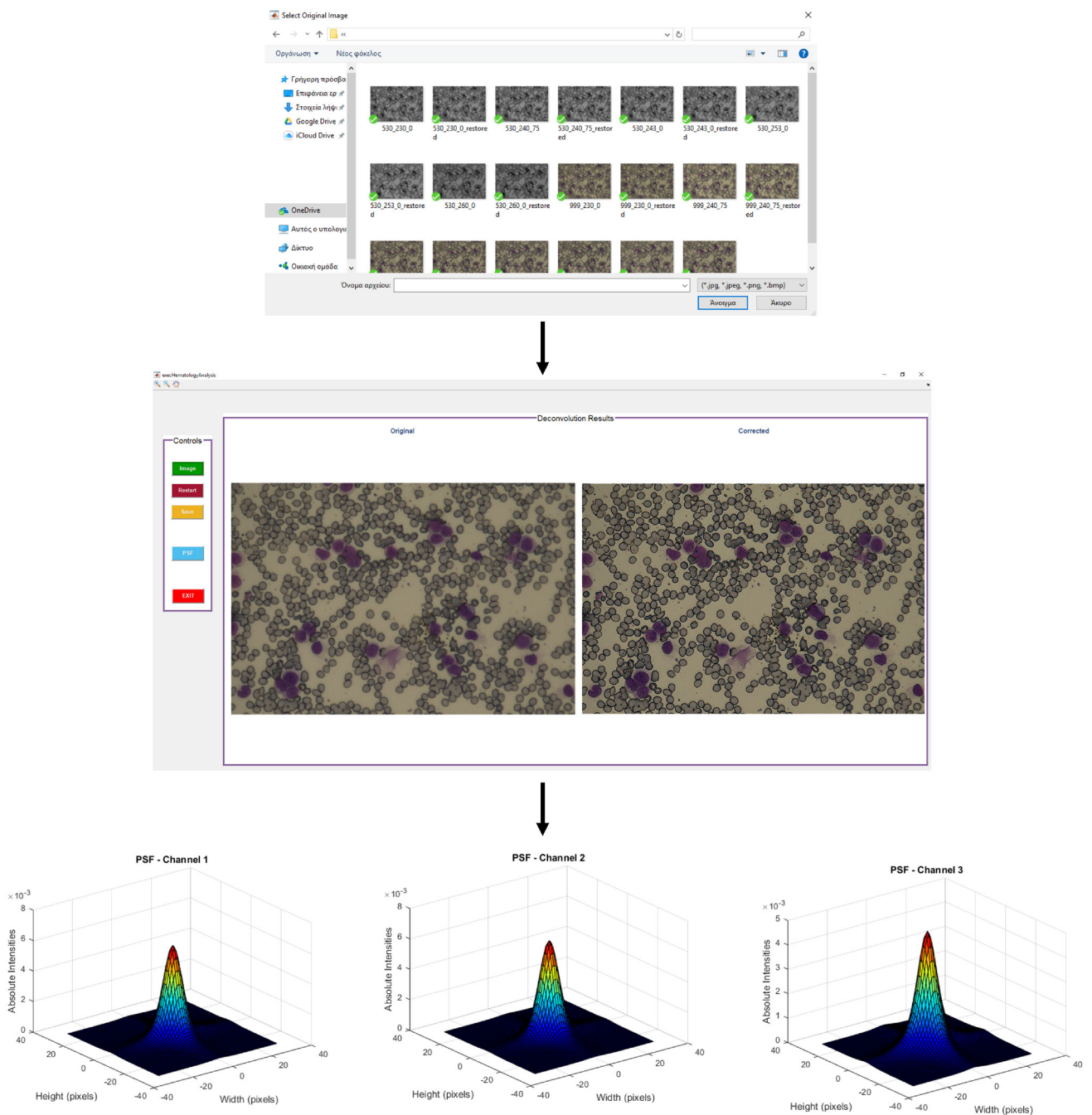
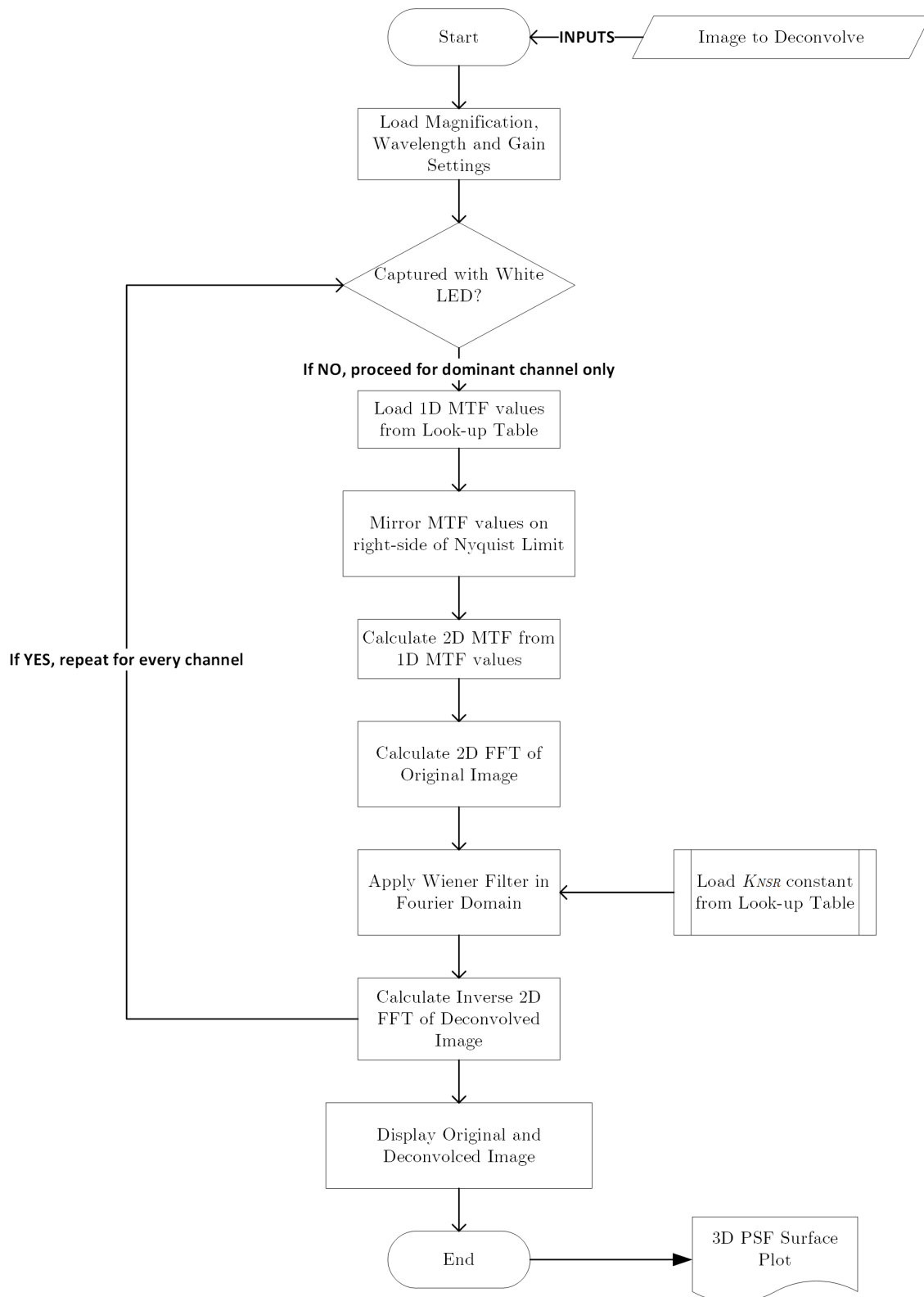


Figure 3.20: Program execution for enhancing imaging resolution in microscopy.



**Figure 3.21:** Algorithm flowchart for enhancing resolution in microscopy.

### 3.2.4.4 Brightfield and Fluorescence Deconvolution Examples

The proposed procedure has been evaluated with real microscope samples, in color, spectral and fluorescence imaging modes. In the case of color imaging, a sample

of MG-G stained peripheral blood smear was imaged using the broadband white LED and in the case of spectral imaging using the 530nm LED. Additionally, in the case of fluorescence, a stained sample of cell series with Alexa 555 fluorophore was imaged, using a narrowband LASER light source at 532nm excitation wavelength. Three visual examples of resolution enhancement using the proposed deconvolution method are presented in [Figure 3.23], [Figure 3.22] and [Figure 3.24].

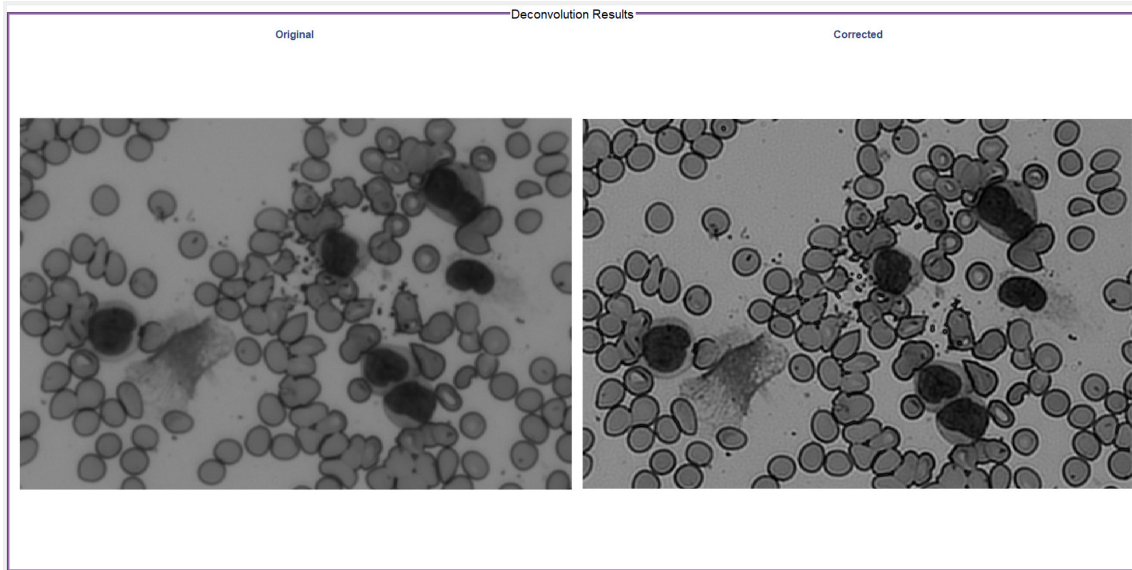


**Figure 3.22:** Deconvolution results on spectral image of 530nm.

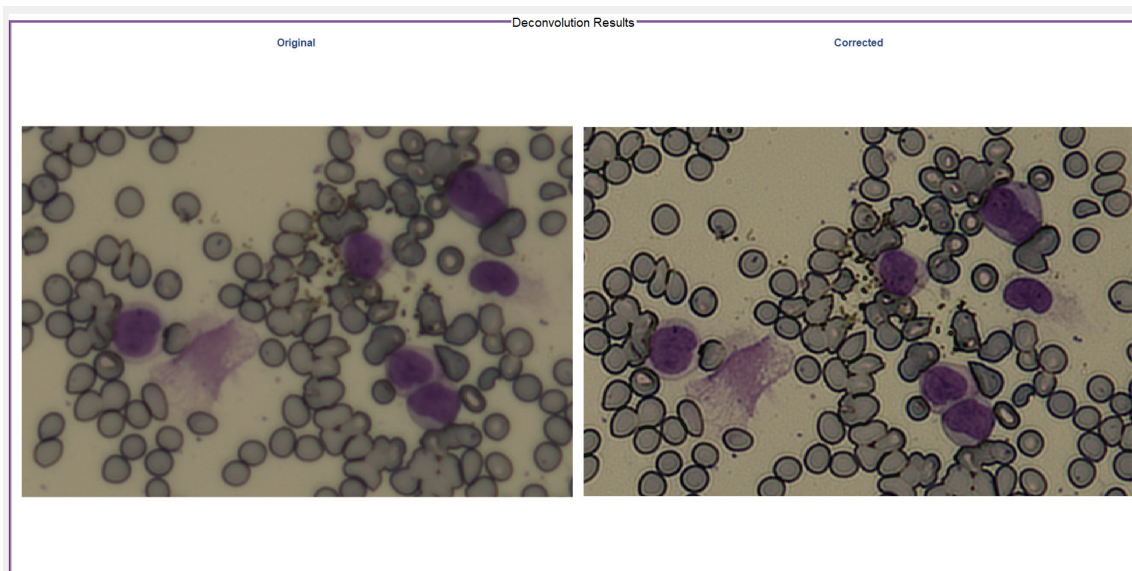


**Figure 3.23:** Deconvolution results on color image.

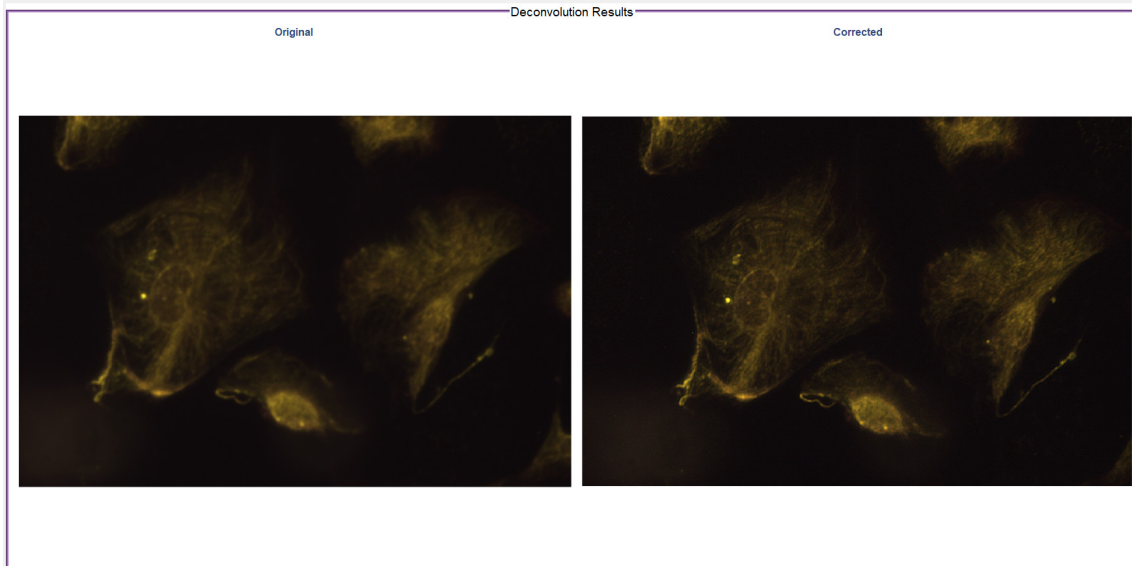


**Figure 3.24:** Deconvolution results on fluorescence image of 532nm excitation wavelength.

In addition, in order to evaluate the performance of our algorithm in terms of optical resolution quantitatively, brightfield and spectral images captured at four different magnifications were deconvolved. The corresponding resolutions were compared in terms of lp/mm at 50% of modulation using slanted edge analysis, between original and deconvolved images. The results are presented in [Table 5]. It is depicted that the proposed method is capable of enhancing the imaging resolution of the microscope beyond its optical limits, at least by 111% in terms of retrieved optical resolution and thus reveals important features of the samples (such as, organelles of cells nucleus and fine cytoskeletal structures). This sets a solid basis to produce spectral and color images of superior resolution, in order to provide precise and highly accurate analytical and classification results for leukemia samples, using the method developed and presented in *Chapter 3*.

Magnification	530nm LED			White LED		
	Original (lp/mm)	Deconvolved (lp/mm)	Improvement (%)	Original (lp/mm)	Deconvolved (lp/mm)	Improvement (%)
<b>20.5x</b>	369	943	156%	389	820	111%
<b>21.4x</b>	356	877	146%	363	813	124%
<b>23x</b>	338	862	155%	358	798	123%
<b>23.8x</b>	310	855	176%	333	785	136%

**Table 5:** Quantitative results of the proposed method for enhancing imaging resolution in microscopy (all resolutions correspond to object plane).

---

## 4 Method for Improving Leukemia Diagnosis

The diagnosis of leukemia relies upon a multiparametric approach involving a number of different examinations. Nowadays, common diagnostic procedures for identification of leukemic abnormalities are based on routine morphological examination and evaluation of peripheral blood and bone marrow samples, along with repeated complete blood counts (CBC), differential blood counts (DBC) and clinical observations of the symptoms. In addition, more advanced and sensitive diagnosis is conducted through identification of immunologic, cytogenetic and molecular characteristics, which are increasingly employed to help refine diagnosis, establish prognosis and determine the most appropriate treatment, including rational therapies targeting the underlying genetic lesion [61].

However, morphological distinctions of the abnormal WBCs using light microscopy, remains the mainstream examination modality to identify and classify different types of leukemia, along with cytochemistry tests and flow cytometry procedures [62]. On the other hand, pathologists' criteria for leukemias diagnosis based on light microscopy images, are mostly qualitative and highly depended to their experience and their analytical skills. This fact may lead to errors, albeit infrequently in modern times, either in the diagnosis or classification of leukemia [6]. A misdiagnosis of leukaemia subjects patients to the risks of cytotoxic therapy and the risk of mistakes is reduced by a collaborative approach to diagnosis in which there is systematic clinical and morphological review of all possible cases of leukemia by senior members of staff and by recognising the circumstances in which diagnostic problems may occur.

In the past, several studies tried to identify the spectral signatures of the WBCs across various types of leukemia, in order to improve its diagnostic accuracy. Indicatively, studies were conducted for spectral morphometric characterization of abnormal lymphocytes in CLL [63], for identification of "blastic cells" using color images analysis [64], or even for spectral characterization of ALL in childhood [43].

It is understandable that the development of a computational method, based on spectral examination of blood cells, is capable to provide highly accurate quantitative parameters for improving leukemia diagnosis. Thus, for the first time in the relevant literature to the best of our knowledge, we developed and introduce a method that identifies and indicates "blastic cells" and differentiates normal from abnormal lymphocytes, which are present in ALL and CLL diseases respectively,

---

based on novel quantitative spectral indices of peripheral blood smears, measured using optical light microscopy.

## 4.1 Presentation of Microscope System

As presented in subsection 3.2.4., the microscope setup where the proposed method developed, deployed and tested is the *Lumnia Series BF-FL-Hem Multi-Modal Microscope* as depicted in [Figure 3.15]. This microscope has a multi-wavelength tunable LED light source, which combined with a six-megapixel imaging sensor, creates an excellent setup for spectral imaging on peripheral blood smears.

Along with the microscope, a prototype spectral unmixing program for estimating the pseudocolor images of concentrations for every component on samples stained with MG-G, has been developed in the past [65] [66]. This program utilizes the SIMPLS algorithm presented in subsection 2.2.2.2, in order to calculate the concentrations for every one of the three components (i.e., Methylene Blue, Azure B, Eosin Y) with pixel-level accuracy. The microscope is capable to acquire spectral images on 465nm, 505nm, 530nm, 600nm, 640nm and 685nm, the exact same wavelengths where the SIMPLS algorithm has the greatest weights for estimating the concentrations of MG-G components, as studied and developed in [66].

In addition, a seventh spectral band of 980nm is employed, in order to measure the transmitted light  $I_\theta$ , for precise application of Beer Lambert's Law as analyzed in subsection 2.2.2.3 and as presented in [65]. The outcomes of the aforementioned program are three monochrome pseudocolor images (i.e., one for every stain component) with pixel intensities between 0 to 255, which correspond from the lowest to the highest possible concentrations of these components on the sample [Figure 4.1]. These pseudocolor images along with the six spectral images were used as inputs to the proposed method.

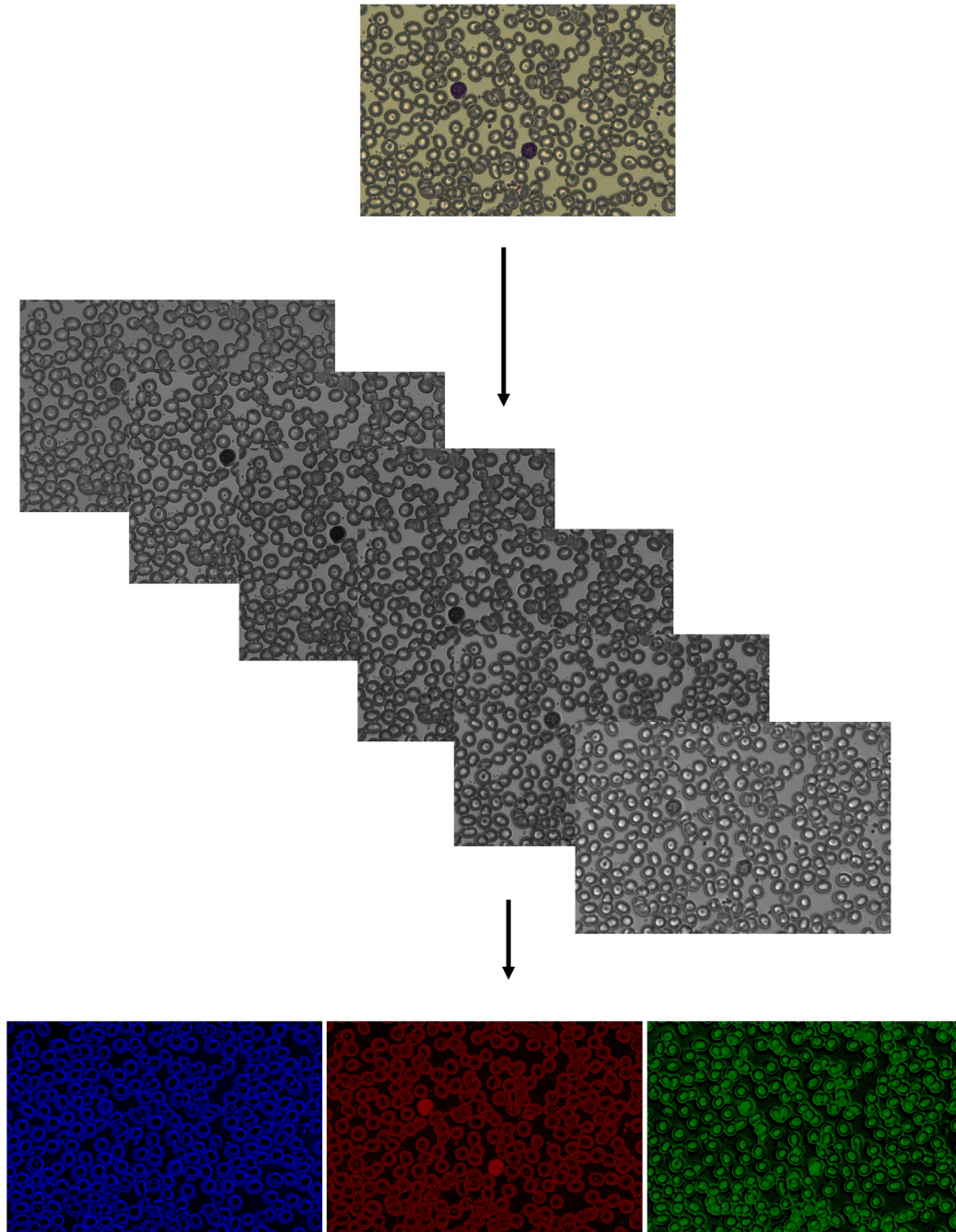


**Figure 4.1:** Spectral unmixing procedure and concentrations estimation, using SIMPLS algorithm, on MG-G stained samples.

## 4.2 System Training with Experimental MG-G Stain Mixtures

A critical step before proceeding to the development of the proposed method, was the appropriate training of the system (i.e., of the spectral unmixing program), with an experimental dataset of absorbance spectra based on real mixtures of the MG-G components, which are used by hematologists. Originally,

the spectral unmixing program was trained based on bibliographic absorbance spectra of the Methylene Blue, Azure B and Eosin Y components separately [66], and based on those spectra the corresponding spectra of their mixtures had been estimated algorithmically, in order to simulate different mixtures of the components.

In this thesis, in order to achieve precise training of the system, we ordered [67], [68], [69] and prepared in the lab, mixtures of the exact same components that are used by the hematologists, when applying the MG-G staining protocol. The experimental design used, was the Full Factorial Design [31] according to which the response variables (here the absorbances) are measured for all possible combinations of highest and lowest concentrations of the components.

The number of possible combinations, in order to form an experimental dataset according to full factorial design is  $2^m$  where  $m$  is the number of factors (i.e., number of components). A more representative example of full factorial design for three components is displayed in [Table 6]. For the highest possible concentration, 'H' was set and for the lowest admissible one 'L', which correspond to concentrations that gives absorbance of 0.9 and 0.1 respectively (in order to be within the linear limits of Beer Lambert's Law as explained in 2.2.2.3).

Combination	Methylene Blue	Azure B	Eosin Y
1	H	H	H
2	H	H	L
3	H	L	H
4	H	L	L
5	L	H	H
6	L	H	L
7	L	L	H
8	L	L	L

**Table 6:** Full Factorial Design for MG-G components.

Additionally, along with the eight combinations of the above mixtures, the absorbance spectra of every component were measured separately and for concentrations that have absorbance between 0.1 and 0.9 and with a step of 0.1. These 27 pure absorbance spectra (9 spectra for every of the 3 components in MG-G), along with the 8 mixtures absorbance spectra, were used as experimental training set for the SIMPLS algorithm, in order to calculate the  $B$  regression coefficients matrix in {2.11}, with high accuracy.

The laboratory setup [Figure 4.2] that was used for measuring these absorbance spectra was employed two halogens lamps with emission spectrum from 400nm up to 1000nm and an Ocean Optics USB4000-VIS-NIR spectrometer [70] that is sensitive to measure between 350nm and 1000nm.

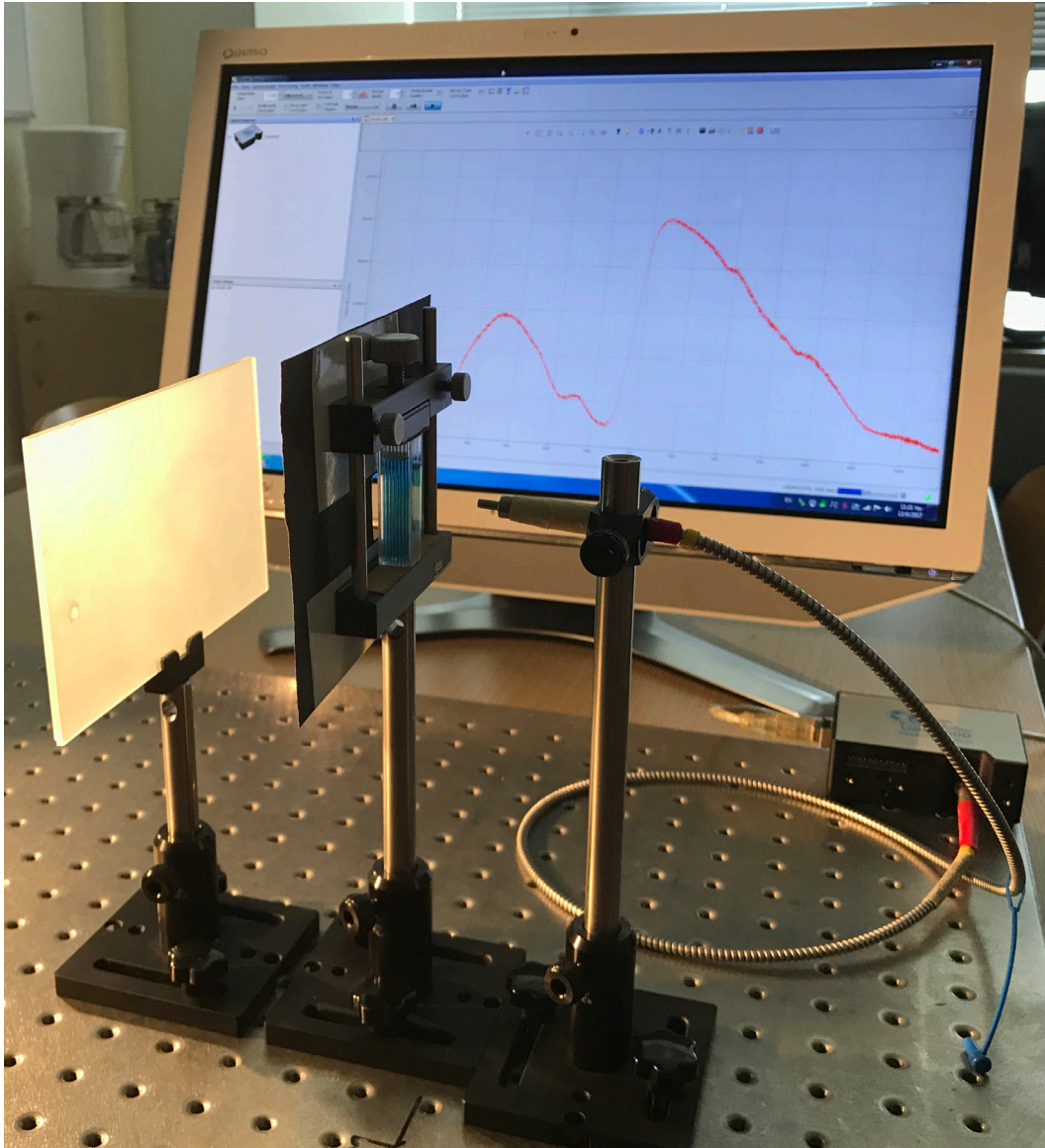


**Figure 4.2:** Laboratory setup for measuring MG-G components absorbance spectra.

Finally, in [Figure 4.3], [Figure 4.4] and [Figure 4.5] are presented the measured pure absorbance spectra of Methylene Blue, Azure B and Eosin Y respectively and in [Figure 4.6] the measured absorbance spectra of the mixtures that resulted according to full factorial design.

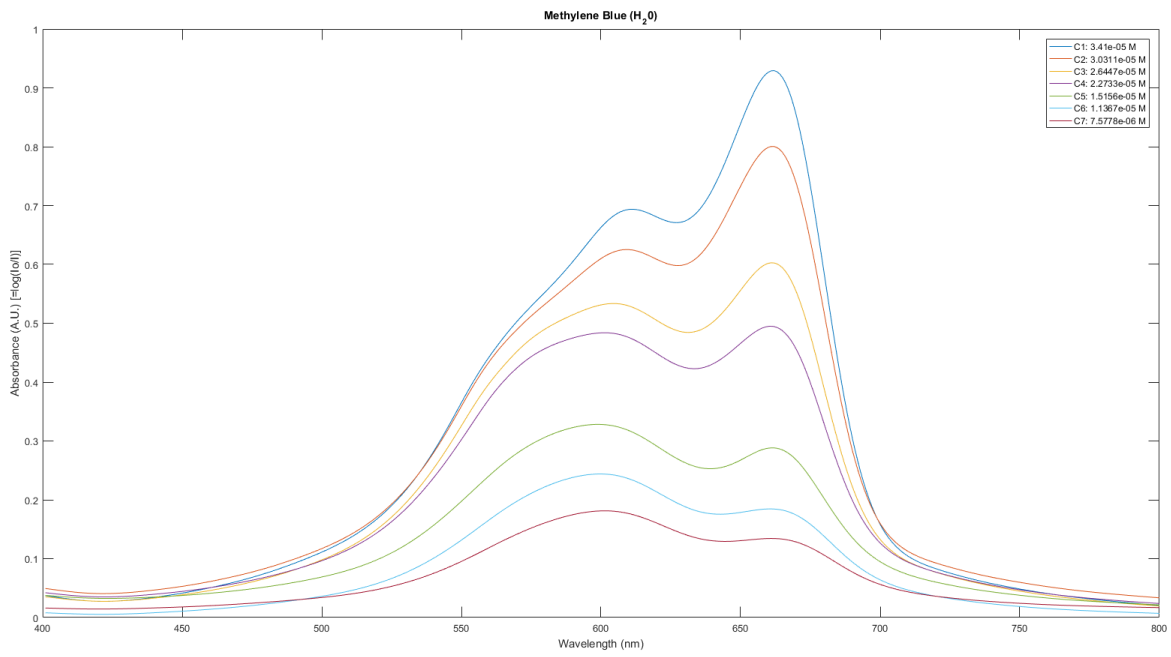


**Figure 4.3:** Methylene Blue measured absorbance spectra.

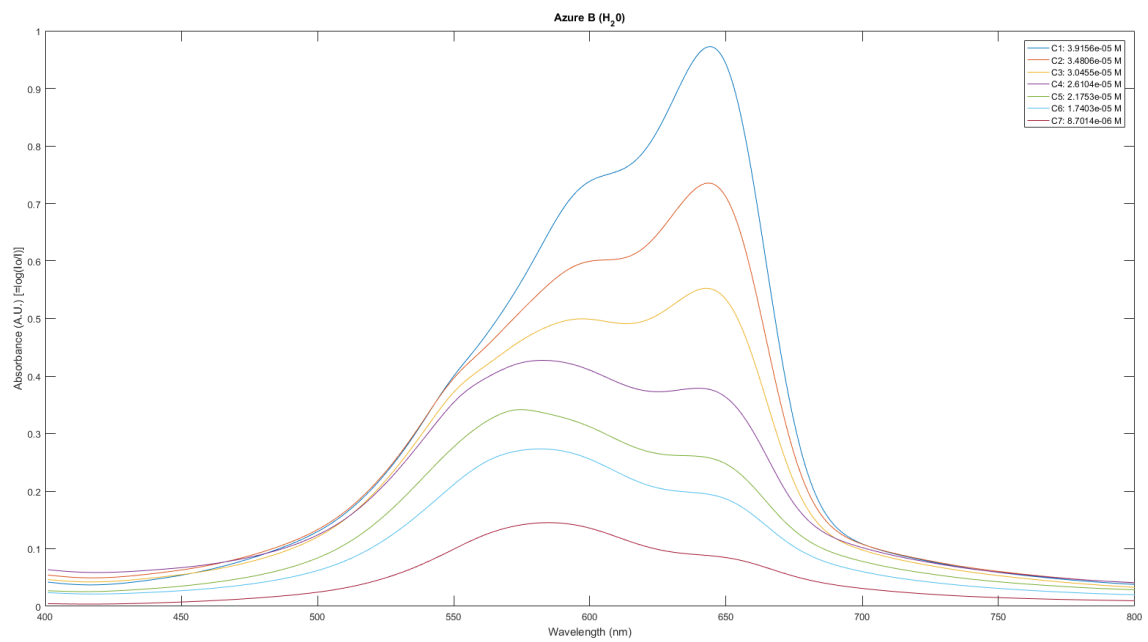


**Figure 4.4:** Azure B measured absorbance spectra.

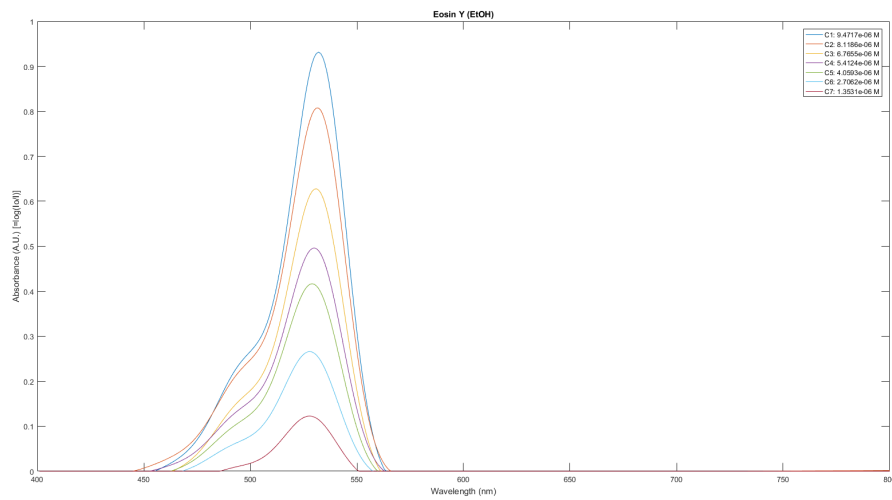


**Figure 4.5:** Eosin Y measured absorbance spectra.

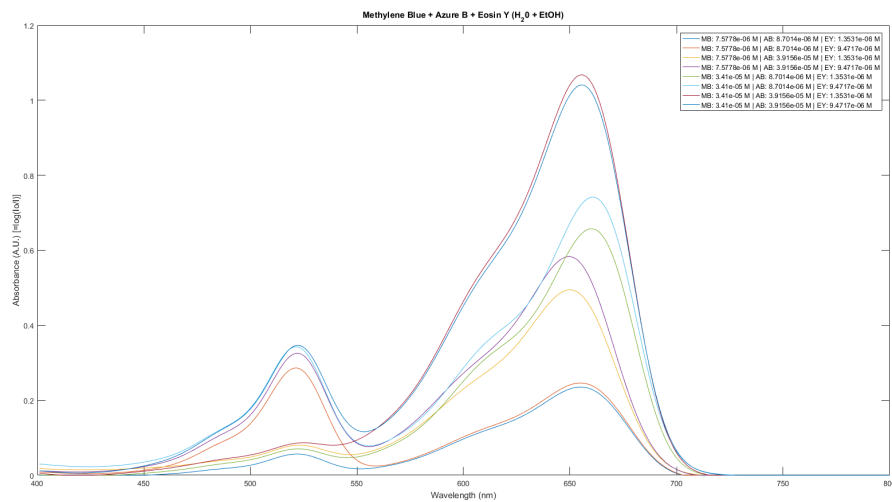


**Figure 4.6:** MG-G components mixtures measured absorbance spectra.

### 4.3 Method for Identification and Separation of Blood Cells

The first part of the developed procedure performs identification and separation of WBCs and RBCs in a blood smear under microscope examination and it decomposes WBCs in their two primary components (i.e., the nucleus and the cytoplasm) for further examination as presented in subsection 4.4. In addition, it performs and provides CBC statistics for WBCs and RBCs, giving an immediate knowledge for the amount of the basic blood cells in the examined hematological sample. A detailed flowchart of the proposed method is presented in [Figure 4.7], followed by a detailed analysis of every module separately.

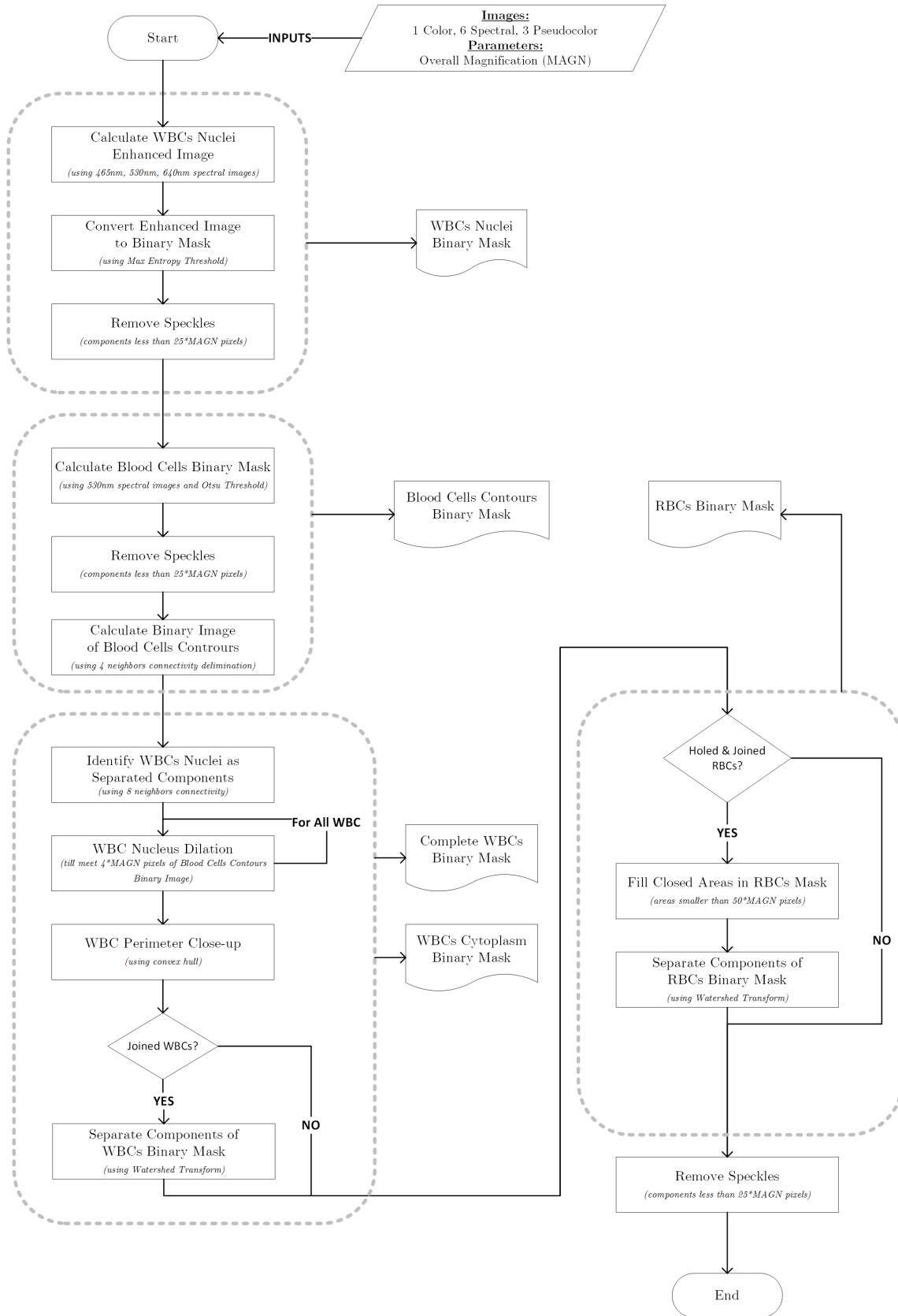


Figure 4.7: Flowchart of blood cells identification and separation method.

The proposed method is composed from four processing modules, each one of them

performing distinct steps towards the precise estimation of critical masks and information for the analysis and classification performed next. The method receives eleven inputs; the color image, the six spectral images, the three pseudocolor images and the overall magnification with which the area under examination had been captured.

#### 4.3.1.1 WBCs Nuclei Binary Mask Estimation Module

The first module of the proposed method estimates a binary mask that indicates the nuclei of the lymphocytes. This is accomplished by fusion of spectral information available in images captured at 465nm, 530nm and 685nm.

On 465nm, the observed differences between the red blood cells and the lymphocytes are minimal. Hemoglobin of red blood cells absorbs almost the same amount of light as the nuclei and cytoplasm of lymphocytes. The 530nm is a key spectral band of the analysis. The WBC's nucleus absorbs strongly and thus becomes dark and formed clearly. The RBCs are darkened too, as Eosin Y works as a counterstain, but the real change is on the nucleus of the WBCs. Finally, at 685nm only some parts of the WBCs remain relative dark due to absorbance of nucleus chromatin (stained with Methylene Blue), while the RBC have again similar absorbance as in 465nm.

Combining these three spectral images as in {4.1}, an enhanced image of WBCs nuclei is estimated as depicted in [Figure 4.8]. Afterwards, using an appropriate thresholding technique, a binary mask that indicates the exact location of WBCs nuclei is exported. The Maximum Entropy threshold [71] was used, which tries to select the appropriate pixel intensity value  $t$ , which divides the image in two classes, with every class maximizing the metric of entropy in it {4.2}. Thus, the one class contains pixels of high intensity values that are close each other (i.e., the pixels of WBCs nuclei) and the other class contains pixels of low intensity values that again are close each other (i.e., the pixels of the rest image).

$$EnhancedImage(i, j) = \frac{Image_{465nm}(i, j) + Image_{685nm}(i, j)}{2 \cdot Image_{530nm}(i, j)} \quad (4.1)$$

where  $i, j$  are coordinates of pixels.

$$Entropy_{pixels} = - \sum_j P_j \cdot \log_2(P_j) \quad (4.2)$$

where  $P_j$  is the probability that the difference between two adjacent pixels of the class is equal to  $j$ .

As this procedure may identify small objects of the sample (mostly platelets and speckles due to noise), a final step of thresholding is applied at the binary mask.

This step rejects connected components with area less than  $25MAGN$  pixels, which relate to 8 pixels connectivity. Here, the total magnification of the system is taken into consideration, in order to discard small objects dynamically, as their area in pixels cannot be thresholded by a constant, due to the fact that is directly proportional to the magnification. Finally, existed “holes” inside detected nuclei are filled using 8 pixels encirclement as filling criterion, as they are areas that did not identified as parts of nuclei successfully.

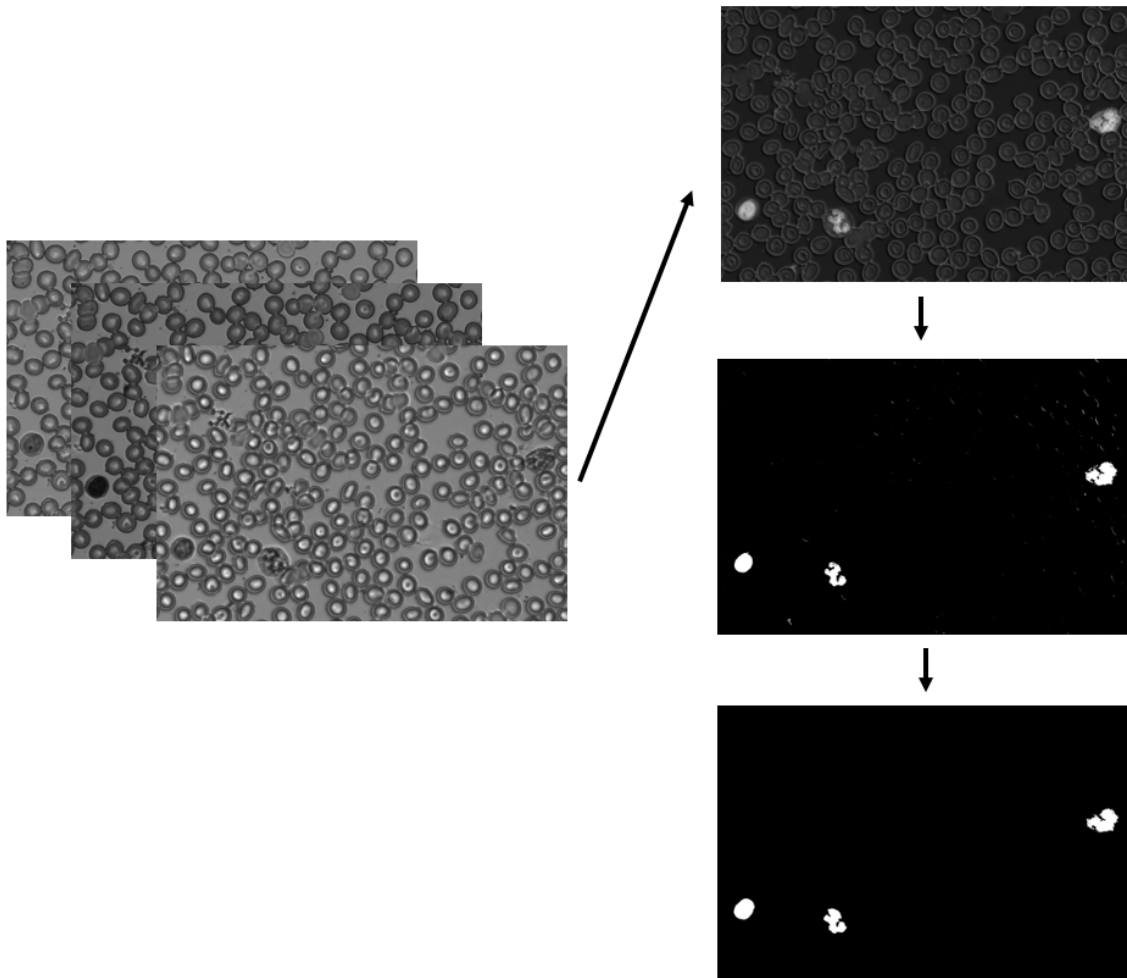


**Figure 4.8:** Steps of WBC nuclei binary mask estimation module.

#### 4.3.1.2 Blood Cells Contours Binary Mask Estimation Module

The second module of the proposed method estimates a binary mask that indicates the contours of WBCs and RBCs of the sample. This is accomplished by using spectral information available in image captured at 530nm.

As explained previously, the spectral information available at 530nm is the most meaningful, due to the fact that all components of blood are at their peak absorbance. Thus, applying a threshold using Otsu’s Method [71] results a binary mask that contains the blood’s components separated from the background. Specifically, Otsu’s Threshold tries to select the appropriate pixel intensity value

$t$ , which divides the pixels of an image into two classes and minimizes the intra-class variance simultaneously. In the case of the proposed method, the two classes contain pixels with high intensity values (i.e., the background) and pixels with lower intensity values (i.e., the blood components that absorb light) respectively, as depicted in [Figure 4.9].

Additionally, as in the first module, a final step of thresholding is applied at the binary mask, in order to reject connected components with area less than  $25 \cdot MAGN$  pixels, which are encircled with 8 pixels. Finally, at the remained binary image, every pixel that relates to other pixels with 4 pixels connectivity, is eliminated. This procedure returns an image that contains only the contours of the blood's components.

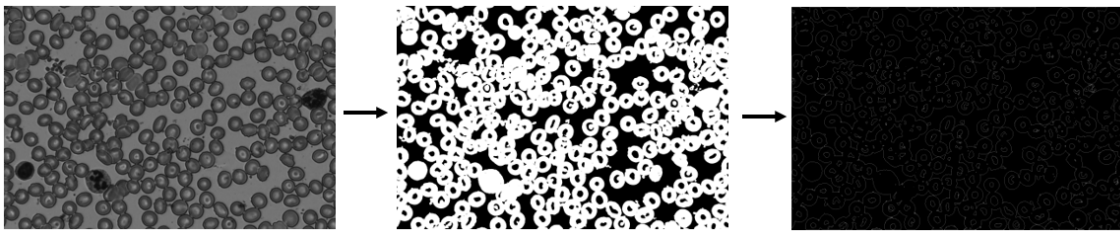


**Figure 4.9:** Steps of blood cells contours binary mask estimation module.

#### 4.3.1.3 Complete WBCs and WBCs Cytoplasm Binary Masks Estimation Module

The third module of the proposed method concentrates on the estimation of a binary mask that indicates the cytoplasm of WBCs. Due to the previous knowledge of WBCs nuclei and blood cells contours, this procedure is almost straightforward.

The logic is to start from the nucleus, which is centered inside WBC and by dilating its mask repeatedly, the corresponding binary mask of the complete WBC to occur. The repetition of dilation is terminated when a total of  $4 \cdot MAGN$  joined pixels between the dilated mask and the contour mask is met (i.e., the mask of contours acts as a fragment factor for the repeating dilation). This procedure is performed for every leukocyte separately, which is easy to do as by having a binary mask that contains all WBCs' nuclei, the different leukocytes can be located as many isolated components of this mask [Figure 4.10]. For the procedure of dilation, a circular object with radius of 5 pixels was used as structural element.

A vulnerable aspect of this approach is that for leukocytes with non-circular nuclei (such as Neutrophils, Eosinophils, Basophils and Monocytes) may occur incomplete masks, due to the dilation of their nuclei's masks. In order to overcome this problem, an additional step is applied, with which a close-up is performed around the detected leukocytes. This close-up is based on the calculation of the convex hull on the outer perimeter of every leukocyte, which represent the final binary mask of the complete WBC, as depicted for the lymphocyte at the bottom

of [Figure 4.10].

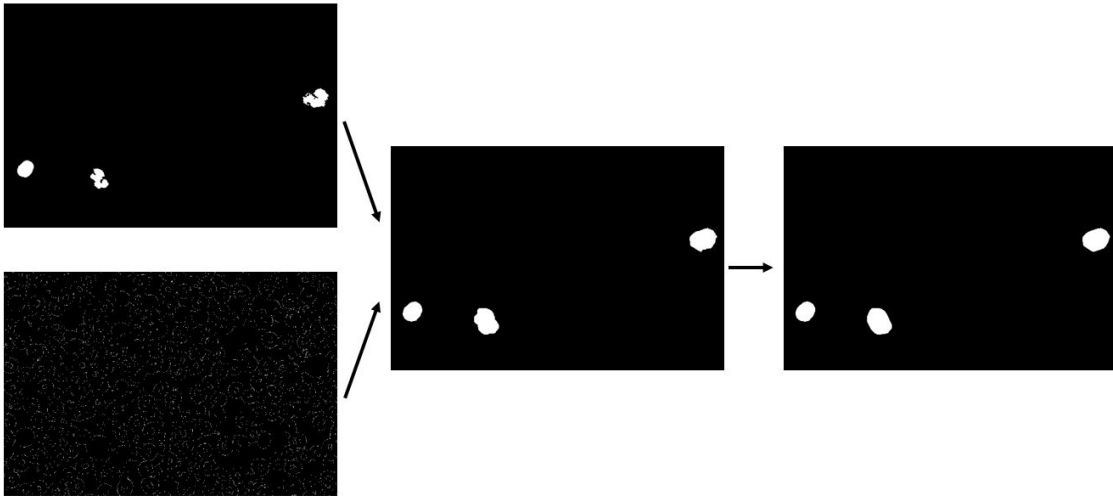


**Figure 4.10:** Steps for estimation of complete WBC binary mask.

A final and optional step of this module, that is executed after request of the user, performs the further separation of joined leukocytes. It is common in samples of CLL, a huge number of leukocytes to be existed, which may be joined on their perimeter. The proposed method analyzes and classify every WBC separately, thus it is important, the binary mask of WBCs, not to contain joined leukocytes. To handle scenarios like that, the proposed method can perform cells segmentation by applying the watershed transform [72] on complete WBCs' binary mask. Specifically, as the watershed transform cannot be applied on binary images directly, first the distance transform [73] of the complement of the binary mask is computed, in order to create texture inside leukocytes, based on pixels' Euclidean distance from the first non-zero pixels on their perimeter. Then, the watershed transform is calculated on the image that contains the distances, as depicted in [Figure 4.11] and by that, the binary mask is estimated with the separated cells.

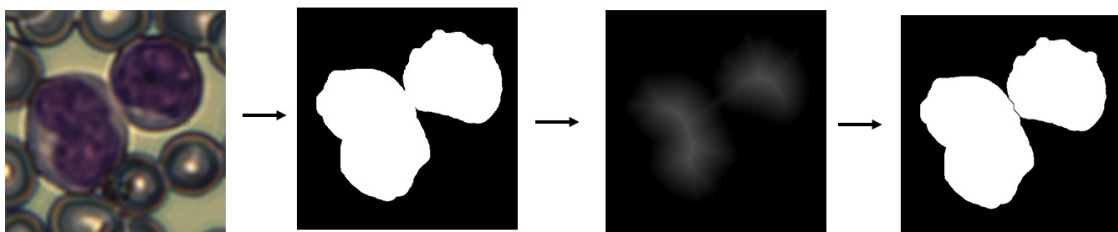


**Figure 4.11:** Watershed transform on joined leukocytes.

Along with the binary mask of the complete WBCs, the binary mask of the WBCs cytoplasm can be calculated by subtracting the one of the WBCs nuclei from the one of the completed WBCs, as in [Figure 4.12].

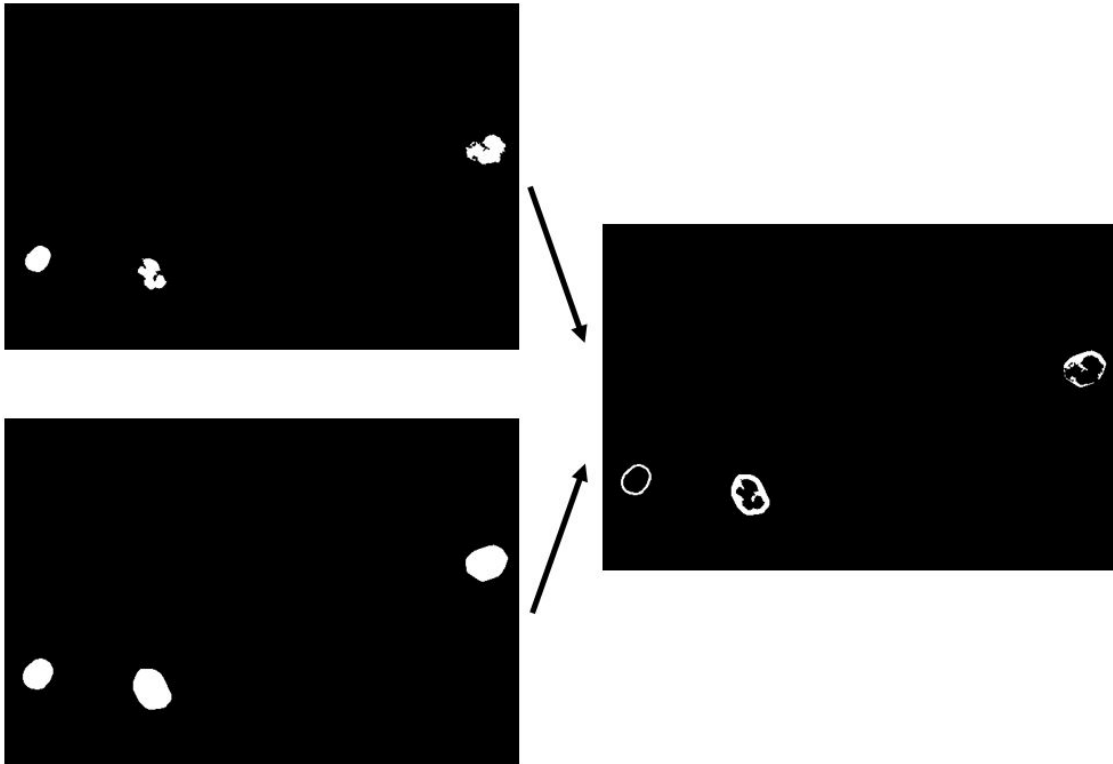


**Figure 4.12:** WBC cytoplasm binary mask extraction.

#### 4.3.1.4 RBCs Binary Mask Estimation Module

The fourth and last module of the proposed method estimates a binary mask that indicates the RBCs of the sample. The mask of this module is useful only for reasons of cytometry, as explained in the next subsection.

The extraction of RBCs binary mask is simple relatively, as from module two, an initial blood cells binary mask is existed and from module three, a complete WBCs binary mask. Thus, using those two masks and subtracting the second from the first one, the desired RBCs mask is estimated.

However, as depicted in [Figure 4.9], for high values of magnification, the transmitted light penetrates through the slim central cavity of RBCs and thus those areas have pixel intensities almost identical with the background values. This phenomenon has as a result the thresholding procedure to fail and the extracted binary mask to contain holes in the center of RBCs.

In order to overcome this problem, an additional step is applied, with which areas smaller than  $50 \cdot MAGN$  are filled using 8 pixels encirclement as filling criterion, while the ability for manual refinement of this threshold is given to the user. Afterwards, using the same method of watershed transform as in 4.3.1.4, the joined RBCs are separated and finally small objects (such as platelets and speckles due to noise) are rejected, if they have area less than  $25 \cdot MAGN$  pixels. The procedure of this module and the corresponding steps are presented in [Figure 4.13].



**Figure 4.13:** Steps of RBCs binary mask estimation module.

#### 4.4 Method for Stains Uptake Analysis and WBC Classification

The second part of the developed procedure performs quantitative analysis of the uptake of the MG-G stain's components on every leukocyte separately. In addition, it provides cytometry statistics for the area under examination as an approach for conducting basic CBC through microscope images. Finally, based on the aforementioned analysis, it classifies the WBC of the lymphoid series quantitatively, in classes of lymphoblastic cells, abnormal and normal lymphocytes. As in 4.3, first a detailed flowchart of the proposed procedure is presented in [Figure 4.14], followed by a detailed analysis of every module separately.

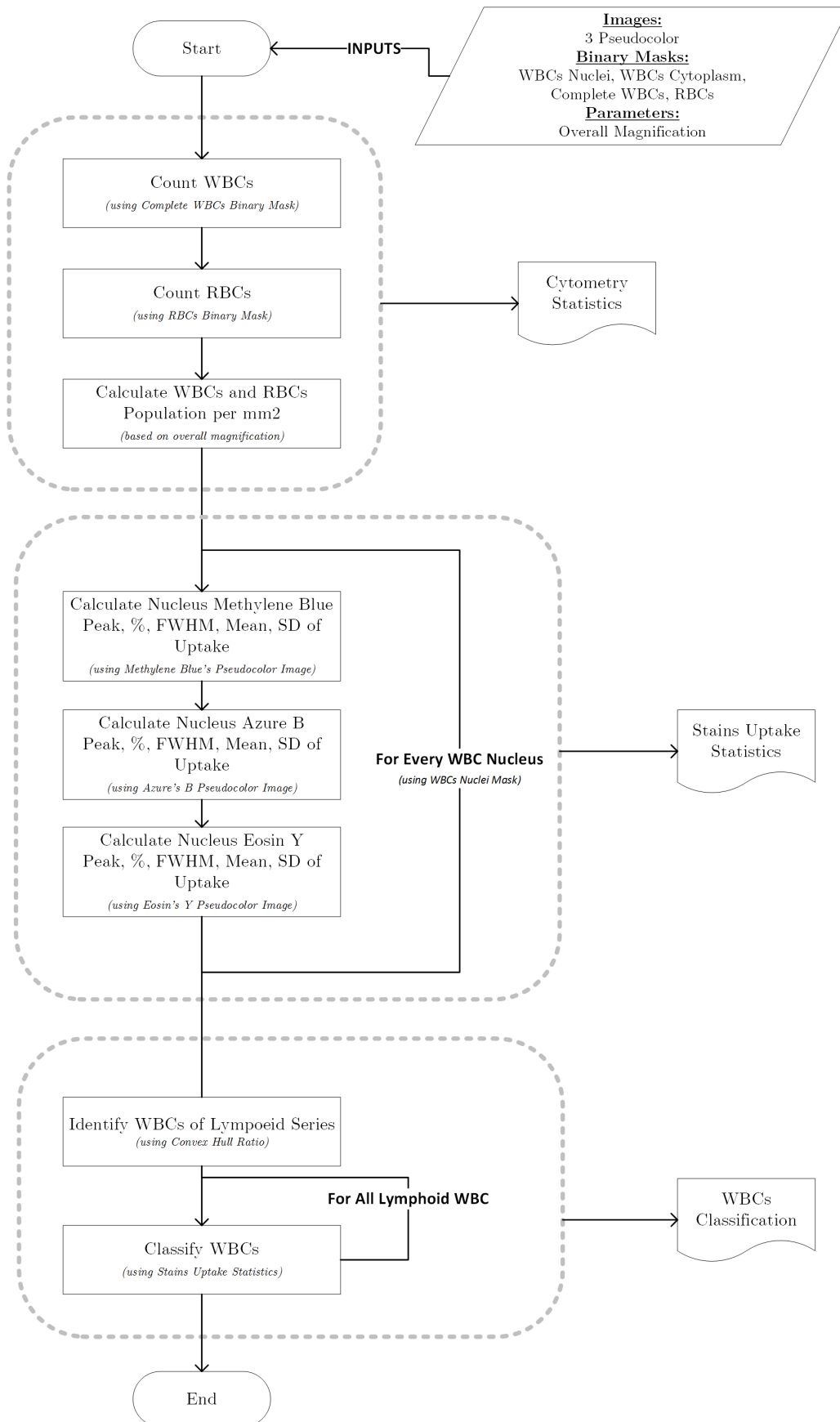


**Figure 4.14:** Flowchart of leukocytes classification and stains uptake analysis method.

#### 4.4.1.1 Cytometry Statistics Calculation Module

The first module of the proposed method performs a series of calculations that correspond to a basic CBC, in terms of WBCs and RBCs amount existed in the area under examination. More precisely, it calculates their absolute number, their percentage and their amount per square millimeter. As for the last one calculation (i.e. number of cells per  $\text{mm}^2$ ), the method takes into consideration the current magnification and the FOV of the system. These calculations are straightforward to be performed, as from the method of blood cells separation, binary masks are available that indicate the WBCs and RBCs precisely.

#### 4.4.1.2 Stains Uptake Indices Calculation Module

The second module is the most important. It performs a complete uptake measurement of the MG-G stain's components (i.e. Methylene Blue, Azure B and Eosin Y) on detected WBCs nuclei, with pixel-level accuracy. As the cellular differences between blastic cells in ALL, abnormal lymphocytes in CLL and normal lymphocytes are indicated in cell's nucleus mainly, the proposed method performs this analysis in pixels that correspond to leukocytes' nuclei. Since, the WBCs nuclei binary mask is available through module presented in subsection 4.3.1.1, this analysis can be performed directly and with high accuracy.

For every WBC, five indices are calculated for every MG-G's component, which mapping the uptake behavior in the cell's nucleus. These indices are:

- *Peak Uptake*, which measures the concentration of the stain's component with the higher presence in the nucleus.
- *Peak Percentage*, which measures the percent of the nucleus area that has the aforementioned peak uptake.
- *FWHM (Full Width at Half Maximum)*, which depicts how susceptible is the cell's nucleus in the stain's component. Malignant cells (such those in CLL) are expected to have narrower FWHM, in comparison with that in normal cells.
- *Mean Uptake*, which measures the average concentration of the stain's component in the cell's nucleus.
- *SD Uptake (Standard Deviation)*, which describes how much the concentrations are diverging from the mean uptake.

The aforementioned indices are calculated through concentrations provided per pixel by pseudocolor images and which take values between 0 to 255. These values of pixel intensities are related directly to concentrations expressed in  $\text{mol/L}$  or  $M$ , but they are preferred in the calculation procedures.

#### 4.4.1.3 WBCs Classification Module

The third and last module of the proposed method refers to the classification algorithm of leukocytes, based on a subgroup of the aforementioned quantitative

uptake indices.

The proposed algorithm targets to differentiate the abnormal lymphocytes in a blood smear from the normal ones and to locate blastic cells (i.e., lymphoblasts). That way, users (i.e., hematologists) have except of a set of 15 quantitative indices for WBCs and an additional characterization of leukocytes in four classes of interest; *Normal Lymphocytes*, *Abnormal Lymphocytes*, *Lymphoblasts* and *Other WBC*.

As in ALL the presence of lymphoblasts in the peripheral blood is an immediate indication of this leukemic abnormality as explained in 2.3.4.1, and the presence of abnormal lymphocytes (such as small with clumped chromatin as described in 2.3.4.2) is an immediate indication of CLL disease, this classification provides an instantaneous characterization of the clinical situation of the patient's sample under examination, even in cases when this is not feasible through the judgement of doctors.

The algorithm is consisted of two parts. The first part tries to differentiate the leukocytes of lymphoid series (i.e., lymphocytes and lymphoblasts) from the rest of the WBC. This is achieved by employing a metric that we call as *Lymphoid Ratio*, presented in {4.3}.

$$\text{Lymphoid Ratio} = \frac{\# \text{ pixels of nucleus}}{\# \text{ pixels of nucleus' convex hull}} \quad (4.3)$$

This ratio takes values from 0 to 1. The numerator refers to the area covered by the leukocyte's nucleus and the denominator refers to the convex hull that encloses this area. For cells of lymphoid series, nucleus is expected to be shaped as circular or elliptical and thus its convex hull will cover a similar area with the nucleus, resulting to a high ratio. On the other hand, in the rest of WBCs (such as monocytes and polymorphonuclear granulocytes), the irregular, kidney-shaped or lobes-shaped morphology of their nucleus will result to convex hull with significant difference in the area from that covered by the nucleus, resulting to a mid to low ratio.

The second part of the algorithm tries to differentiate the normal lymphocytes from the abnormal lymphocytes and to identify the lymphoblasts. For the lymphoblasts, as it is expected to have lower concentrations of Eosin Y in comparison with matured lymphocytes (in [43] is proved that lymphoblasts have significant lower absorption in 540nm in comparison with lymphocytes, almost the same spectral band where Eosin Y has its absorption peak), the *Eosin's Y Mean Uptake* will be lower. Thus, the identification is conducted based on this parameter. Additionally, as abnormal lymphocytes are characterized from many small rims and points of clumped chromatin which is stained with Eosin Y and Azure B mainly as presented in [Table 2], the concentrations of these components on abnormal lymphocytes nuclei, are expected to be higher. Thus, the

differentiation is conducted based on fusion of *Eosin's Y FWHM* and *Azure's B Peak Uptake* indices. The pseudocode of the proposed algorithm is:

### ***WBC Classifier***

---

```

start
  if (Lymphoid_Ratio < 0.88) then
    Class ← 'Other WBC'
  else
    if (Eosin_Y_Mean_Uptake ≤ 69) then
      Class ← 'Lymphoblast'
    else
      if (Eosin_Y_FWHM ≥ 27) or (Azure_B_Peak_Uptake ≥ 60) then
        Class ← 'Abnormal Lymphocyte'
      else
        Class ← 'Normal Lymphocyte'
      end
    end
  end
end
finish

```

The exact thresholds of the *WBC Classifier* algorithm were identified, after detailed examination and analysis of leukemic and normal samples, as presented in 4.6.

## **4.5 Method Implementation**

The method described in the aforementioned subsections had been developed as a standalone program, using Mathworks Matlab R2016b and Mathworks Matlab GUIDE for GUI design, combined and tested on *Lumnia Microscope*. In the developed program, all the information and indices described, are available through different partitions of the program's window, as depicted in [Figure 4.15].

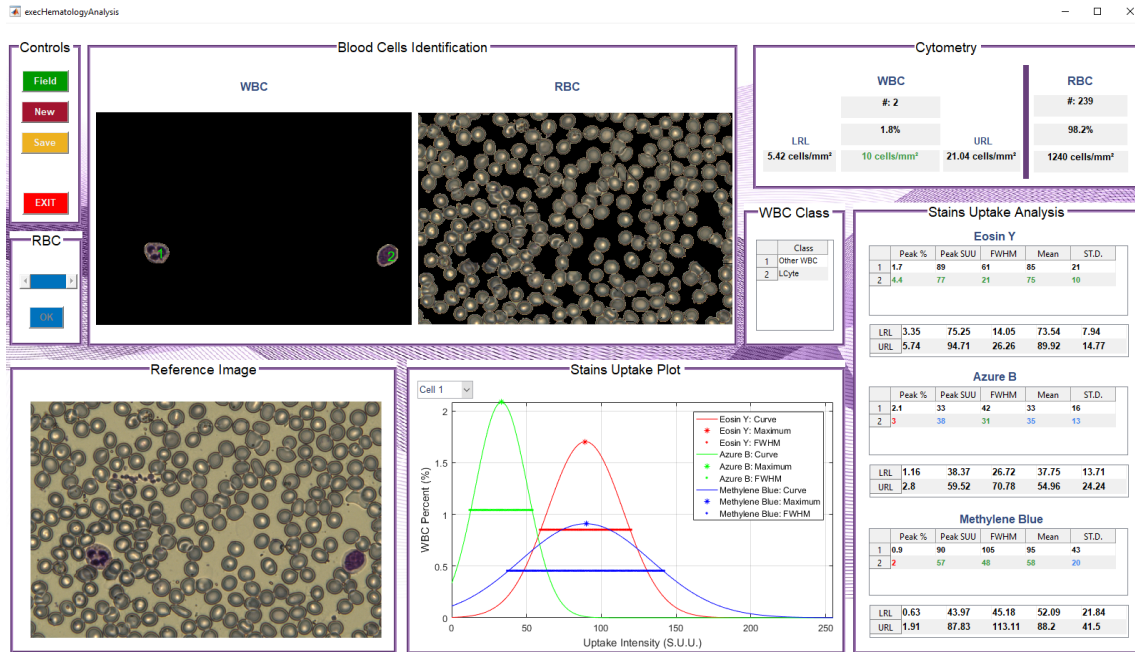


**Figure 4.15:** Developed program for blood cells identification, separation and classification.

As seen above, the program is divided in eight partitions. The first partition on the upper left part of the window corresponds to basic controls. From these push buttons, the user has the ability to select folders with images that correspond to the desired areas for analysis, he can restart the program, save the current results of analysis and classification in a *.xlsx* file and of course to terminate the program. By selecting a desired folder for analysis, the program initiates its execution and performs the procedures presented in subsection 4.3., in order to estimate the binary masks of WBCs and RBCs.

The truncated color images using these masks are displayed in a partition named *"Blood Cells Identification"* in the upper center part of the window, alongside with the original color image for reference in a partition named *"Reference Image"*. During these estimations, the user is asked by the program, if WBCs and RBCs are requiring separation, as explained in subsections 4.3.1.3 and 4.3.1.4 respectively. If so, the user clicks on *"Yes"* and the program performs these separations via watershed algorithm. In addition, the user has the ability to refine the threshold used for filling holes inside RBCs mask as described in 4.3.1.4, using the controls on the middle left partition of the window.

After the completion of binary masks estimation, the program provides the cytometry results for WBCs and RBCs on the upper right partition of the window, named as *"Cytometry"*. Alongside with these numbers, the Lower Reference Level (LRL) and the Upper Reference Level (URL) are provided, which have been estimated after analysis of normal samples, as presented in the following subsection 4.6.1.

Furtherly, the stains uptake analysis and classification of detected leukocytes are

performed using the procedures in subsection 4.4. The five quantitative indices for every MG-G's component (i.e., Eosin Y, Azure B and Methylene Blue) alongside with the corresponding Reference Levels [74] of normal lymphocytes, are presented in the center-lower right partition of the window named as “*Stains Uptake Analysis*”, while the classification results in a centered partition named as “*WBC Class*”.

Finally, a plot that depicts the distribution in nucleus of the uptake for the three MG-G's components of a selected WBC, is presented in the lower center partition of the window named as “*Stains Uptake Plot*”. By selecting a desired WBC from the drop-down list in the upper left part of this partition, the program calculates and plots the different uptake intensities in relation to the percentages of the WBC's nucleus area that have those intensities. In addition, it marks with a “\*” the peak value of the every component and with a horizontal line the FWHM range of every component, as depicted in [Figure 4.16].

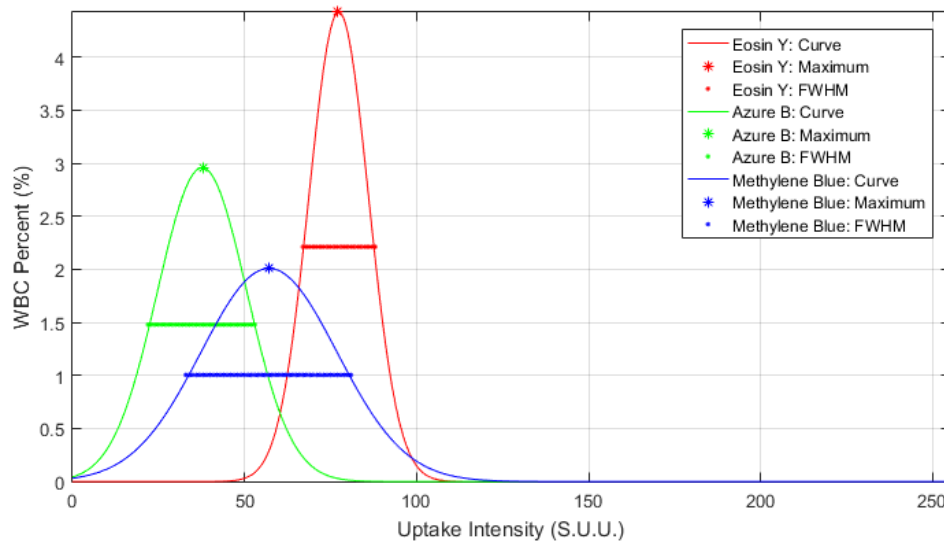


**Figure 4.16:** Example of stains uptake plot, for a normal lymphocyte.

In the developed program, the detected leukocytes are marked with green numbers in their color image, as references. Those numbers correspond to indexed rows of the tables with stains uptake indices and classification results. Also, the indices of the lymphocytes that lay outside the reference ranges are marked with red color (if they are above the corresponding URL), with blue color (if they are below the corresponding LRL) or with green color (if they are within the corresponding reference range).

## 4.6 Results on Leukemic Samples

The evaluation of the proposed method, in terms of sensitivity and specificity, was measured using several samples of peripheral blood smears from

patients with Chronic Lymphocytic Leukemia and Acute Lymphoblastic Leukemia. In addition, for the establishment of the normal reference ranges of the stains uptake indices for normal lymphocytes and for the cytometry statistics, a set of peripheral blood smears were analyzed from normal persons.

More specifically, samples from 4 patients ailing with CLL, 2 patients ailing with ALL and 3 normal persons, were analyzed. Those samples were collected and characterized, in cooperation with hematologists from *General Hospital of Thessaloniki "G. Papanikolaou"* and were analyzed with the proposed method using *Lumnia Microscope*. For every sample, 20 different areas of interest were selected within monolayer region. An overview of the used dataset, is presented in [Table 7].

<b>Analyzed Normal Persons</b>	3
<b>Analyzed ALL Patients</b>	2
<b>Analyzed CLL Patients</b>	4
<b>Total Analyzed Areas</b>	180

**Table 7:** Used dataset overview.

#### 4.6.1 Analysis of Normal Population

The indices of MG-G's components uptake on lymphocytes identified by our algorithm inside analyzed areas of normal population, were used to determine the lower and upper limits of the corresponding reference ranges. Reference ranges [74] is a solid basis for comparison for a physician or other health professional to interpret a set of test results for a particular patient. In medicine, reference ranges are used for blood tests extensively and their limits for a desired metric using a set of  $n$  samples, are calculated as in {4.4}, {4.5}:

$$LRL = m - t \cdot \sqrt{\frac{n+1}{n}} \cdot SD \quad (4.4)$$

$$URL = m + t \cdot \sqrt{\frac{n+1}{n}} \cdot SD \quad (4.5)$$

where  $m$  is the mean value of the metric,  $SD$  is the standard deviation of the metric and  $t$  is the Student's t-distribution value [75] for the 97.5% percentile with  $(n-1)$  degrees of freedom.

In [Table 8], the calculated reference ranges of MG-G's components uptake indices are presented, based on the lymphocytes of normal population. Additionally, the complete results of uptake analysis per lymphocyte in normal population, can be

found in [Table 14] of Appendix A.

Stain Component		URL	LRL
<b>Eosin Y</b>	Peak Uptake	5.7	3.4
	Peak Percent	95	75
	FWHM	26	14
	Mean Uptake	90	74
	SD Uptake	15	8
<b>Azure B</b>	Peak Uptake	2.8	1.2
	Peak Percent	60	38
	FWHM	71	27
	Mean Uptake	55	38
	SD Uptake	24	14
<b>Methylene Blue</b>	Peak Uptake	1.9	0.6
	Peak Percent	88	44
	FWHM	113	45
	Mean Uptake	88	52
	SD Uptake	44	19

**Table 8:** Reference ranges of lymphocytes from normal population, for MG-G's components uptake indices.

Finally, as for the results of cytometry, the corresponding reference ranges of detected leukocytes and erythrocytes per  $\text{mm}^2$ , inside analyzed areas of normal population is presented in [Table 9], while the complete cytometry results per analyzed area and normal person, can be found in [Table 15] of Appendix A.

Cells per $\text{mm}^2$	URL	LRL
<b>WBC</b>	21	6
<b>RBC</b>	1517	1043

**Table 9:** Reference ranges of detected leukocytes and erythrocytes amount, within normal population.

#### 4.6.2 Acute Lymphoblastic Leukemia Results

For the diagnosis of ALL, the proposed method tries to identify any lymphoblast existed in the sample under examination, based on *Eosins' Y Mean Uptake*, which clearly takes very low values in comparison with lymphocytes (refer to [Table 14], [Table 17] and [Table 19] in Appendixes A, B and C). In [Table 10], the results of this case are presented.

Identification Method		Proposed Algorithm	
		Lymphocytes	Lymphoblasts
Hematology Atlas	Lymphocytes	273	3
	Lymphoblasts	0	32

**Table 10:** Confusion matrix for identification of lymphoblasts over lymphocytes.

It is shown that the proposed algorithm, from a total of 308 leukocytes of lymphoid series (i.e., normal lymphocytes, abnormal lymphocytes and lymphoblasts) across all analyzed areas available, identified lymphoblasts with high accuracy, resulting to sensitivity of 100% and specificity of 98.91%. As validation to the results of the proposed algorithm, every leukocyte was identified manually, using morphological hematology atlases as reference [4]. Indicatively, a characteristic pattern of MG-G's components uptake on a lymphoblast's nucleus, is presented in [Figure 4.17].

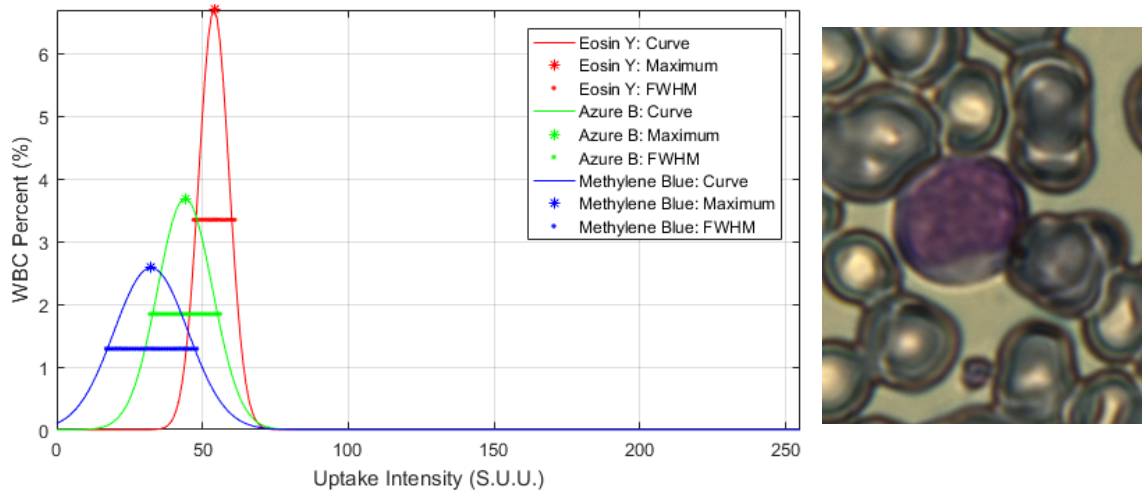


**Figure 4.17:** Lymphoblast's characteristic pattern of MG-G's components uptake in nucleus.

Additionally, the complete results of uptake analysis per lymphocyte and lymphoblasts within ALL samples, can be found in [Table 16] and [Table 17] of Appendix B. Finally, in terms of cytometry, the complete results per analyzed area and patient ailing with ALL, can be found in [Table 18] of Appendix B.

### 4.6.3 Chronic Lymphocytic Leukemia Results

As CLL is characterized by the existence of high amounts of mature but abnormal lymphocytes, the proposed method tries to locate abnormal lymphocytes and to differentiate them from the normal ones, that are existed in the samples under examination.

The differentiation between normal and abnormal lymphocytes is based on that within CLL samples, there are normal lymphocytes alongside to abnormal ones.

Thus, after defining the reference ranges of normal lymphocytes as presented in 4.6.1, exclusion of normal lymphocytes is possible through uptake indices within those ranges. Then, the remaining lymphocytes can be considered as potentially abnormal and by selecting appropriate thresholds for *WBC Classifier* algorithm, quantitative differentiation is feasible from the normal ones. In [Table 11], the results of this case are presented.

Identification Method		Proposed Algorithm	
		Normal Lymphocytes	Abnormal Lymphocytes
Hematology Atlas	Normal Lymphocytes	95	3
	Abnormal Lymphocytes	44	131

**Table 11:** Confusion matrix for differentiation of normal from abnormal lymphocytes.

It is shown that, the proposed algorithm, from a total of 273 lymphocytes (i.e., normal lymphocytes and abnormal lymphocytes) across all analyzed areas available, identified abnormal lymphocytes very accurately, resulting to sensitivity of 74.86% and specificity of 96.94%. Indicatively, a characteristic pattern of MG-G's components uptake on an abnormal (CLL) lymphocyte's nucleus, is presented in [Figure 4.18], alongside with [Figure 4.19], where a normal (mature) lymphocyte's nucleus is presented.

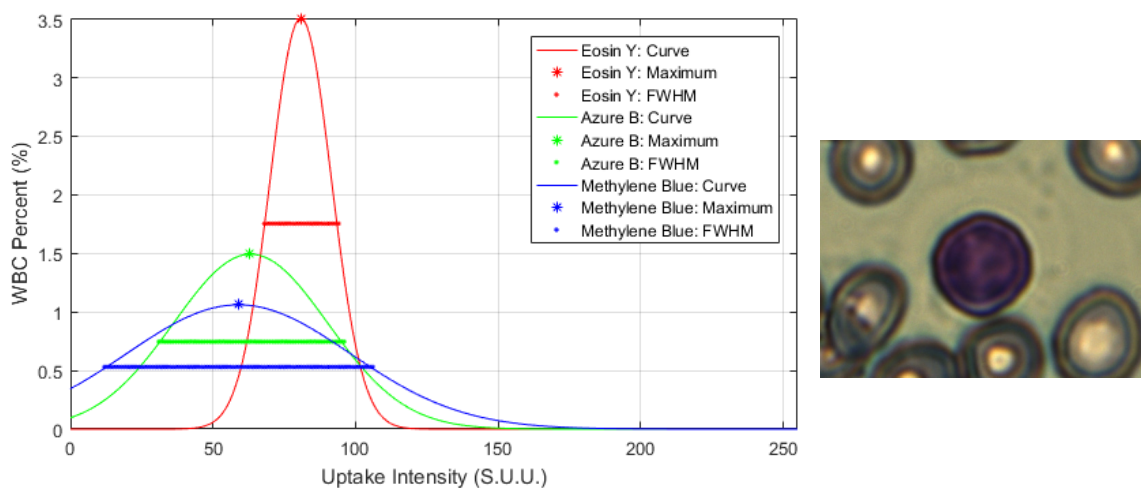


**Figure 4.18:** Abnormal (CLL) lymphocyte's characteristic pattern of MG-G's components uptake in nucleus.

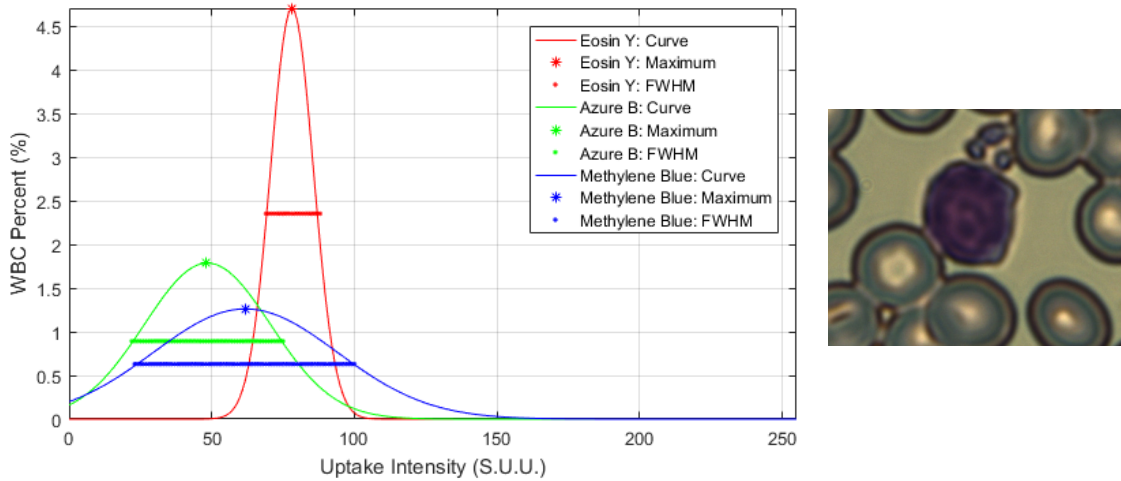


**Figure 4.19:** Normal (mature) lymphocyte's characteristic pattern of MG-G's components uptake in nucleus.

Again, the complete results of uptake analysis per lymphocyte within CLL samples, can be found in [Table 19] of Appendix C. Finally, in terms of cytometry, the complete results per analyzed area and patient ailing with CLL, can be found in [Table 20] of Appendix C.

#### 4.6.4 Overall Classification Results

Before closing, the efficiency of the proposed algorithm was studied, to differentiate leukocytes of lymphoid series from the rest leukocytes using ratio in {4.3}. The results of this case are presented in [Table 12], where is depicted that the algorithm's specificity is 98.09% and sensitivity is 86.78%.

Identification Method		Proposed Algorithm	
		Lymphoid WBC	Rest WBC
Hematology Atlas	Lymphoid WBC	308	6
	Rest WBC	16	105

**Table 12:** Confusion matrix for differentiation of lymphoid from rest WBCs.

Indicatively, a characteristic pattern of MG-G's components uptake on a neutrophil's nucleus (Rest WBC), is presented in [Figure 4.20].

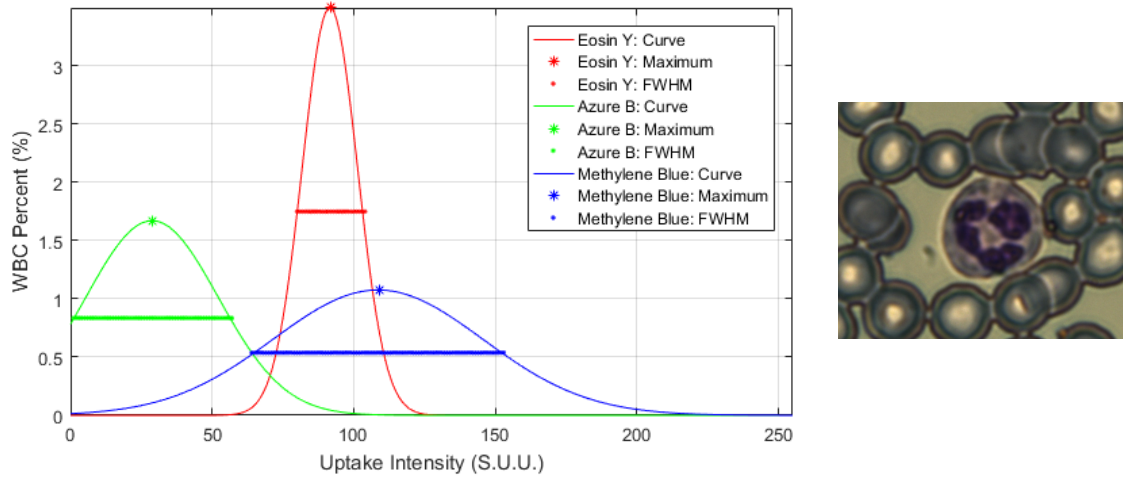


**Figure 4.20:** Neutrophil’s (Rest WBC) characteristic pattern of MG-G's components uptake in nucleus.

Finally, in [Table 13] are presented the overall results of classification for the proposed algorithm, across normal lymphocytes, abnormal lymphocytes, lymphoblasts and rest WBCs.

Identification Method		Proposed Algorithm			
		Normal Lymphocytes	Abnormal Lymphocytes	Lymphoblasts	Rest WBC
Hematology Atlas	Normal Lymphocytes	95	3	0	0
	Abnormal Lymphocytes	44	131	3	4
	Lymphoblasts	0	0	32	2
	Rest WBC	5	11	0	105

**Table 13:** Confusion matrix of overall classification results.

---

## 5 Conclusions and Future Work

In the first part of this thesis, a novel method was developed and evaluated for measuring the performance of microscopes, in terms of retrieved optical resolution. The standardized method in industry and academia [43] for evaluating optical performance in EO imaging systems is through the analysis of slanted edge for estimation of MTF, a key parameter of imaging performance.

Driven by this fact, the proposed approach for estimating MTF via slanted edge analysis in optical microscopy was through the implementation of ISO 12233:2014 method and using a custom-made slanted edge MTF target for brightfield microscopes. It was shown that the proposed approach estimates resolution very accurately and with deviations of 8.3% maximum, from the resolution values provided by the manufacturer of the microscope used in the evaluation procedures. Additionally, by employing the knowledge of this approach, a post capturing enhancement was made feasible for color and spectral images, in order to achieve superior resolution beyond the optical limits of the used microscopes, as a key preparatory step for the accurate and quantitative study and diagnosis of leukemic diseases.

Towards this target, it was introduced for the first time in the relevant literature to the best of our knowledge, a method for extracting the complete two-dimensional optical transfer function of a microscope system, through a single measurement of 1D MTF, using this *a priori* knowledge estimated by the aforementioned approach. In addition, the compensation of 2D OTF was achieved, through image deconvolution in frequency domain, by using Wiener deconvolution. It was measured that the proposed method achieved enhanced optical resolution of up to 176% for a brightfield microscope at 23.8x of total optical magnification, which corresponds to at least 50% distinctive ability at 855 lp/mm of spatial frequency.

In the second part of this master thesis, a novel method was developed and presented based on spectral imaging and quantitative measurement of stain components' uptake in blood smears stained with May Grünwald - Giemsa mixture. This method introduces, for the first time in the relevant literature, spectral indices extracted through chemometrics regression algorithm combined with spectral imaging, for mapping the uptake behavior of MG-G's stain components on leukocytes in a peripheral blood sample under examination, alongside with CBC statistics using optical microscopy.

Summarizing, our method is capable to identify and separate leukocytes and erythrocytes in a microscopy blood smear and their sub-parts (i.e. nucleus and cytoplasm), while it uses spectral information exclusively, in order to locate and differentiate them. Furthermore, an algorithm was introduced that takes advantage of these spectral mapping indices and blood cells separation. It was

---

trained and evaluated on samples with Acute Lymphoblastic Leukemia and Chronic Lymphocytic Leukemia, in terms of identifying and differentiating critical cells for the diagnosis of these diseases. It was concluded that the proposed algorithm achieves 100% sensitivity and 98.91% specificity in cases of ALL by detecting lymphoblasts accurately and sensitivity of 74.86% and specificity of 96.94% in cases of CLL by differentiating and indicating abnormal lymphocytes from the normal ones. Thus, the presented methods can be easily employed as an additional analytical tool for minimizing errors and increasing accuracy, either in the diagnosis and in the classification of ALL and CLL leukemia [6].

In the future, this study could be extended to perform diagnosis also for additional types of leukemia (such as Acute Myelogenous or Chronic Myelogenous) or even for critical types of lymphomas, which may evolve into leukemia and through this approach contribute in the early diagnosis and treatment. Additionally, an alternative interesting and important case of study would be the potential correlation between the proposed spectral indices and the diagnostic characteristics revealed by molecular and more sensitive examinations, as light microscope remains a wide used, accessible and inexpensive method of diagnosis.

---

# References and Bibliography

- [1] D. Vodopich and R. Moore, "Online Learning Center: Biology Laboratory Manual," McGraw-Hill Global Education Holdings LLC., 2017. [Online]. Available: <http://highered.mheducation.com>.
- [2] D. Clifford, "A Protozoological Bicentenary: Antony van Leeuwenhoek and Louis Joblot," *Parasitology*, pp. Vol. 15, pp: 308-319, 1923.
- [3] K. Spring and M. Davidson, "Introduction to Fluorescence Microscopy," Nikon MicroscopyU, 2008.
- [4] J. Meletis, Atlas of Hematology, Athens: Nereus Publishers LTD, 2009.
- [5] Nature Methods | Editorial, "The quest for quantitative microscopy," Springer Nature, 2012.
- [6] J. Chessells, "Pitfalls in the diagnosis of childhood leukaemia," *British Journal of Haematology*, pp. pp. 506-511, September 2001.
- [7] W. Greiner, Quantum Mechanics: An Introduction, Springer, 2001.
- [8] M. Dudzik, "Volume 4: Electro-Optical Systems Design, Analysis, and Testing," in *The Infrared & Electro-Optical Systems Handbook*, Bellingham, Washington USA, SPIE Optical Engineering Press, 1993.
- [9] L. Pedrotti, "Module 1.4: Basic Physical Optics," in *Fundamentals of Photonics*, SPIE Optical Engineering Press, 2008.
- [10] V. Mahajan, Aberration Theory Made Simple, SPIE Optical Engineering Press.
- [11] C. William, Introduction to the Optical Transfer Function, SPIE Optical Engineering Press, 2002.
- [12] P. Burns, "Slanted-Edge MTF for Digital Camera and Scanner Analysis," in *PICS Image Processing, Image Quality and Image Capture Systems Conference*, Portland, USA, 2000.
- [13] S. Warren, "Chapter 15.8: The Modulation Transfer Function," in *Modern Optical Engineering*, New York, USA, McGraw-Hill Education, 2008.
- [14] D. Fried, "Optical resolution through a randomly inhomogeneous medium for very long and very short exposures," *Journal of Optical Society of America*, pp. Vol. 56:1372-9, 1966.
- [15] R. Sidney, "Lenses and Optical Systems for Photography, Film, Video, Electronic and Digital Imaging," *Applied Photographic Optics*, Focal Press, p. 40, 2002.
- [16] A. Michelson, "Studies in Optics," University of Chicago Press, Chicago, USA, 1927.
- [17] H. N. Nasse, "How to Read MTF Curves," Camera Lens Division, Carl Zeiss Corp., December 2008.
- [18] G. D. Boreman, Modulation Transfer Function in Optical and Electro-Optical Systems, Bellingham, WA: SPIE Press, 2001.
- [19] Edmund Optics, "Comparison of Optical Aberrations," Edmund Optics Press, 2011.
- [20] D. Simpkins, "Modeling and Estimation of Spatially-Varying Point-Spread Functions Due to Lens Aberrations and Defocus," Master of Science Thesis, Notre Dame, Indiana, 2011.
- [21] D. B. Murphy, Fundamentals of Light Microscopy and Electronic Imaging, Wiley-Liss Publications, 2001.
- [22] C. Balas, "Course Lectures: Advanced Topics In Electronic Imaging," School of Electrical and Computer Engineering, Technical University of Crete, Chania, GR, 2016.
- [23] S. Bradbury and B. Bracegirdle, Introduction to Light Microscopy, BIOS Scientific

- Publishers, 1998.
- [24] Edmung Optics, "Optical Microscopy Application: Fluorescence," [Online]. Available: <https://www.edmundoptics.com/resources/application-notes/microscopy/optical-microscopy-application-fluorescence/>.
- [25] A. Jeffrey, "Biomarkers and surrogate endpoints," *British Journal of Clinical Pharmacology*, pp. 491-494, 2005.
- [26] C. Balas and G. Epitropou, "Chapter 7: Multi-Hyperspectral Imaging," in *Handbook of biomedical optics*, CRC Press, 2011.
- [27] N. M. Short, "Electromagnetic Spectrum: Spectral Signatures," [Online]. Available: [https://www.fas.org./irp/imint/docs/rst/Intro/Part2\\_5.html](https://www.fas.org./irp/imint/docs/rst/Intro/Part2_5.html).
- [28] D. B. Hibbert and J. J. Gooding, *Data analysis for chemistry*, Oxford University Press.
- [29] T. Kratsev, "Chemometrics," [Online]. Available: <http://classification.sicyon.com/References/Chemometrics.pdf>.
- [30] S. Jong, "SIMPLS: An Alternative Approach to Partial Least Squares Regression," *Chemometrics and Intelligent Laboratory Systems*, p. Vol. 18, 1993.
- [31] F. Abatzi, "Diploma Thesis: Spectral Deconvolution and concentration mapping in complex biochemical stains," School of Electronic and Computer Engineering, Technical University of Crete, Chania, GR, 2014.
- [32] L. Beer, "Determination of the absorption of red light in colored liquids," *Annalen der Physik und Chemie*, pp. Vol. 86: 78-88, 1852.
- [33] B. Yanagisawa, "Blood and Hematopoiesis," Johns Hopkins Pathobiology Program, 2014.
- [34] M. Gordon, "Chapter 1: Stem Cells and Haemopoiesis," in *Postgraduate Hematology*, Oxford, UK, Blackwell Publishing Ltd, 2005.
- [35] M. Hoffman, "Human Anatomy: Blood - Red and White Cells, Plasma, Circulation, and More," WebMD.
- [36] Scitable by Nature Education, "Essentials of Cell Biology," Nature, [Online]. Available: <https://www.nature.com/scitable/ebooks/essentials-of-cell-biology-14749010/118237915>.
- [37] H. H. Rashidi and J. C. Nguyen, "Hematology Outlines: An Online Textbook & Atlas of Hematology," 2012. [Online]. Available: <http://hematologyoutlines.com>.
- [38] A. Michelson, *Platelets (3rd Edition)*, Elsevier, 2013.
- [39] L. Dean, *Blood Groups and Red Cell Antigens*, Bethesda, USA: National Center for Biotechnology Information, 2005.
- [40] L. I. Zon, *Hematopoiesis: A Development Approach*, Oxford: Oxford University Press, 2001.
- [41] C. Janeway, P. Travers and M. Walport, *Immunobiology: The Immune System in Health and Disease*. 5th edition., New York: Garland Science, 2001.
- [42] D. W. Wilson, "Pathway Medicine: An Introduction to Clinical Medicine," [PathwayMedicine.org](http://PathwayMedicine.org), 2016.
- [43] N. Katzilakis, E. Stiakaki, A. Papadakis, H. Dimitriou, E. Stathopoulos, E. Markaki, C. Balas and M. Kalmanti, "Spectral characteristics of acute lymphoblastic leukemia in childhood," *Leukemia Research* 28, Elsevier, pp. 1159-1164, 2004.
- [44] C. Pui, "Acute Lymphoblastic Leukemia," *Pediatric Clinics of North America*, pp. 831-846, 1997.
- [45] J. D. Cavenagh and A. T. Lister, "Chapter 2: Chronic Lymphocytic Leukemia - Diagnosis and Management," in *Current Clinical Oncology: Chronic Leukemias and Lymphomas*:

---

*Biology, Pathophysiology, and Clinical Management*, Totowa, NJ, USA, Humana Press Inc..

- [46] I. Georgoulis, *Laboratory Hematology*, Rotonta, 2012.
- [47] International Organization for Standardization, "ISO 12233:2014, Photography - electronic still picture cameras – resolution measurements.," ISO, Geneva, Switzerland, 2014.
- [48] Carl Zeiss, "Objectives from Carl Zeiss: Exceeding Your Expectations," Carl Zeiss Microscopy GmbH, Jena, Germany, 2007.
- [49] J. Sibarita, "Deconvolution Microscopy," in *Advances in Biochemical Engineering/Biotechnology*, Paris, France, Springer, 2005, pp. 202 - 242.
- [50] Q. Wu, F. Merchant and K. Castleman, *Microscope Image Processing*, NY, USA: Academic Press: New York, 2008.
- [51] R. Cole, T. Jinadasa and C. Brown, "Measuring and interpreting point spread functions to determine confocal microscope resolution and ensure quality control," *Nature Protocols*, pp. 1929-1941, 10 November 2011.
- [52] B. Hanser, M. Gustafsson, D. Agard and J. Sedat, "Phase-retrieved pupil functions in wide-field fluorescence microscopy," *Journal of Microscopy*, pp. 32-48, 2004.
- [53] K. Mortensen, L. Churchman, J. Spudich and H. Flyvbjerg, "Optimized localization analysis for single-molecule tracking and super-resolution microscopy," *Nature Methods*, pp. 377-381, 2010.
- [54] J. Wei, B. Bitlis, A. Bernstein, A. de Silva, P. Jansson and J. Allebach, "Stray light and shading reduction in digital photography - a new model and algorithm," *SPIE Electronic Imaging*, January 2008.
- [55] J. Swindells, M. Razaz and K. Tovey, "Modelling PSF of Scanning Electron Microscopes for Image Restoration," in *9th European Signal Processing Conference*, Rhodes, Greece, 1998.
- [56] M. Maule, "Wiener Filter Applied to Deconvolution," Universidade Federal do Rio Grande do Sul - Instituto de Informática, Brasil, 2012.
- [57] G. Xingfa, L. Xiaoying, M. Xiangjun, Y. Tao, S. Jijuan, Z. Yong, X. Hua and G. Ding, "In flight MTF monitoring and compensation for CCD camera on CBERS-02," *Science in China Ser. E Engineering and Materials Science*, pp. Vol. 48, Supp. 1, pp: 29-43, 2005.
- [58] J. T. Bursberg, *Astronomical Optics*, 2nd Edition, p. 433: Academic Press, 199.
- [59] C. de Boor, *A Practical Guide to Splines*, New York, USA: Springer-Verlag, 1978.
- [60] T. York, "Fundamentals of Image Sensor Performance," Washington University in St. Louis, School of ECE, 2011.
- [61] J. Mason and M. Griffiths, "Molecular diagnosis of leukemia.," *Expert Review of Molecular Diagnostics.*, pp. pp. 511-526, 12 June 2012.
- [62] H. Gisslinger and et al, "Clinical impact of bone marrow morphology for the diagnosis of essential thrombocythemia: comparison between the BCSH and the WHO criteria.," *Nature: Leukemia*, pp. pp. 1-7, 12 February 2016.
- [63] Z. Malik, C. Rothmann, T. Cycowitz, Z. Cycowitz and A. Cohen, "Spectral Morphometric Characterization of B-CLL Cells Versus Normal Small Lymphocytes," *The Journal of Histochemistry & Cytochemistry*, pp. 1113-1118, 1998.
- [64] L. Putzu and C. Ruberto, "White Blood Cells Identification and Classification from Leukemic Blood Image," in *Proceedings of International Work-Conference on Bioinformatics and Biomedical Engineering*, Granada, 2013.

- 
- [65] E. Vardoulakis, "Integrated hyper spectral microscopy system: application accuracy improvement in leukemia diagnosis," Technical University of Crete, School of ECE, Chania, Greece, 2016.
- [66] D. Gkotsoulis, "Development of hyperspectral microscopy for improving the diagnostic accuracy in leukemia diagnosis," Technical University of Crete, School of ECE, Chania, Greece, 2016.
- [67] Sigma-Aldrich, "Methylene blue certified by the Biological Stain Commission," [Online]. Available:  
<http://www.sigmaaldrich.com/catalog/product/sial/m9140?lang=en&region=GR>.
- [68] Sigma-Aldrich, "Azure B certified by the Biological Stain Commission," [Online]. Available:  
<http://www.sigmaaldrich.com/catalog/product/sigma/a4043?lang=en&region=GR>.
- [69] Sigma Aldrich, "Eosin Y certified by the Biological Stain Commission, Dye content 90 %," [Online]. Available:  
<http://www.sigmaaldrich.com/catalog/product/sial/119830?lang=en&region=GR>.
- [70] Ocean Optics Inc., "USB4000-VIS-NIR Application-ready Spectrometer for the Visible and near-IR," [Online]. Available: <https://oceanoptics.com/product/usb4000-vis-nir/>.
- [71] P. K. Sahoo, S. Soltani, K. C. Wong and Y. C. Chen, "A Survey of Thresholding Techniques," *Computer Vision, Graphics, and Image Processing*, pp. Vol. 41, pp. 233-260, 1998.
- [72] F. Meyer, "Topographic distance and watershed lines," *Signal Processing*, pp. Vol. 38, pp. 113-125, July 1994.
- [73] C. Maurer, Q. Rensheng and R. Vijay, "A Linear Time Algorithm for Computing Exact Euclidean Distance Transforms of Binary Images in Arbitrary Dimensions," *IEEE Transactions on Pattern Analysis and Machine Intelligence*, pp. Vol. 25, No. 2, pp. 265-270, February 2003.
- [74] M. Häggström, "Establishment and clinical use of reference ranges," *The New England Journal of Medicine*, 2014.
- [75] S. Senn and W. Richardson, "The first t-test," *Statistics in Medicine*, pp. 785-803, 1994.

# Appendix A: Normal Population Samples Analysis

Sample	Area	Normal Population - Lymphocytes															Cell Index
		Eosin Y					Azure B					Methylene Blue					
		Peak (%)	Peak (Int.)	FWHM (Int.)	Mean (Int.)	STD (Int.)	Peak (%)	Peak (Int.)	FWHM (Int.)	Mean (Int.)	STD (Int.)	Peak (%)	Peak (Int.)	FWHM (Int.)	Mean (Int.)	STD (Int.)	
A	2	5.8	83	16	81	9	2.3	45	40	42	16	1.2	72	85	76	32	1
A	2	4.4	91	21	88	12	1.7	50	51	48	21	1.2	89	78	89	35	3
A	3	4.5	83	20	80	11	2.1	43	41	40	18	1.2	82	81	86	33	1
A	4	4.6	82	20	81	9	2.1	51	42	45	18	1.0	65	98	72	36	1
A	4	4.2	85	21	84	12	1.5	49	65	49	23	1.0	69	96	73	37	2
A	5	4.1	97	21	92	14	1.5	49	61	48	22	1.0	90	98	93	37	1
A	7	4.3	86	21	82	12	1.8	44	53	41	19	1.0	81	99	84	36	2
A	11	4.6	82	20	79	10	1.9	51	46	47	18	0.9	64	105	72	39	2
A	11	4.5	78	22	77	10	2.2	54	38	47	18	0.9	49	108	65	40	3
A	12	4.9	77	20	76	9	1.9	49	50	45	19	1.0	55	103	64	36	2
A	14	4.7	87	19	84	11	2.6	52	38	48	16	1.7	63	52	70	27	1
A	15	5.0	81	19	80	10	2.1	57	40	51	19	1.1	61	89	68	33	1
A	15	5.3	84	17	80	11	1.6	47	59	46	21	1.3	68	77	72	31	2
A	15	4.7	78	19	75	11	1.8	48	53	46	20	1.3	62	77	66	32	3
A	17	3.6	76	26	74	11	2.4	41	38	40	15	1.4	62	70	65	27	1
A	17	4.9	81	19	79	9	2.1	46	43	41	18	1.4	64	65	73	31	2
A	18	4.0	87	22	83	13	2.0	52	48	49	20	1.3	60	73	65	30	2
A	19	4.9	83	19	80	10	2.5	56	33	49	18	1.2	61	80	70	35	2
A	20	4.8	81	20	80	9	2.1	44	39	42	18	1.0	36	91	55	36	1
B	1	4.5	81	20	78	11	1.8	46	52	43	19	1.0	58	102	65	35	1
B	1	4.4	89	20	85	13	1.7	45	57	45	20	1.2	72	85	74	33	2
B	1	4.6	80	20	79	10	2.4	40	41	39	16	1.8	57	51	58	23	3
B	3	3.7	90	24	86	13	1.8	45	53	43	18	1.4	70	67	76	31	1
B	4	4.2	88	22	84	11	2.4	46	39	44	15	1.7	63	53	66	24	1
B	5	4.8	94	18	89	13	1.6	54	56	49	21	1.0	80	103	84	39	1
B	6	4.3	89	21	86	11	1.9	51	48	48	19	1.1	79	87	80	34	1
B	6	5.2	85	18	81	11	2.3	47	39	45	16	1.7	66	55	68	24	2
B	7	4.6	90	19	86	12	1.6	55	58	51	22	1.1	73	91	76	33	2
B	8	5.2	91	17	87	11	1.8	48	50	45	19	1.2	70	85	75	33	1
B	8	4.8	88	19	85	10	3.0	54	29	50	15	1.8	53	50	59	27	3
B	9	4.6	91	20	88	11	1.5	51	61	48	22	1.2	64	83	72	34	1
B	9	4.7	88	18	84	12	2.0	50	46	46	19	1.3	71	76	72	30	2
B	10	4.8	86	19	84	10	1.9	46	47	44	18	1.1	77	90	78	35	2
B	11	4.5	93	18	86	16	1.3	55	80	54	26	1.0	72	94	76	36	2
B	11	5.0	86	17	81	12	2.3	42	42	40	16	1.6	66	59	71	26	4
B	11	4.3	85	21	81	11	2.4	47	38	45	17	1.5	63	64	64	26	5
B	13	4.9	94	18	90	12	1.6	49	61	46	21	1.0	74	96	79	35	1
B	14	3.9	91	22	86	14	2.6	45	38	44	14	2.2	70	43	69	17	1
B	14	5.2	90	17	86	11	1.6	51	57	47	21	1.0	75	96	77	36	2
B	14	4.8	86	19	83	11	2.0	53	46	50	19	1.3	64	71	68	31	3
B	17	5.6	86	17	83	9	3.1	50	30	47	14	2.6	49	35	49	16	2
B	19	5.6	87	15	83	10	2.2	40	40	37	15	1.5	52	60	62	32	1
B	20	5.7	87	16	84	10	1.8	52	54	48	20	1.2	57	82	63	32	2
C	1	5.5	78	18	76	9	2.0	58	46	51	20	1.2	54	80	59	30	1
C	2	4.3	83	21	79	12	1.5	52	63	49	22	1.2	69	81	69	32	1
C	2	3.6	80	26	78	11	1.5	59	64	55	23	1.0	61	91	64	35	2
C	3	4.8	80	18	76	11	2.8	61	31	55	18	1.8	47	50	53	26	3
C	7	4.5	84	20	80	12	1.8	62	53	57	21	1.1	52	92	62	36	2
C	8	4.7	85	18	81	12	1.7	40	54	40	19	1.2	83	83	81	31	1
C	10	3.4	90	23	80	18	1.7	40	55	43	21	1.2	81	82	82	32	2
C	11	4.6	84	19	79	13	2.1	43	45	43	18	1.3	71	73	73	29	2
C	12	3.9	81	23	77	13	2.3	45	41	43	17	1.5	68	63	70	29	3
C	13	3.1	79	31	77	13	2.2	45	45	47	18	1.3	60	72	63	30	4
C	14	3.7	89	25	85	12	1.4	43	67	44	22	1.0	76	95	78	34	1
C	15	4.6	79	21	77	10	2.1	44	45	41	17	1.2	62	86	65	32	3
C	16	3.3	87	26	83	14	1.8	48	54	46	20	1.2	71	75	76	35	1
C	17	4.9	79	19	77	10	2.2	52	39	47	19	1.2	58	79	61	29	1
C	17	4.0	77	23	75	11	2.8	49	33	50	15	1.6	51	60	52	23	2
C	18	3.9	86	25	85	11	1.4	55	72	53	24	1.0	63	96	70	36	2
C	19	5.3	86	17	83	11	1.5	48	66	49	23	1.2	86	82	79	33	1
C	20	3.6	80	26	78	12	1.6	52	61	53	22	1.1	56	85	63	2	1

Table 14: Analysis of MG-G stain's components uptake for lymphocytes in normal population.

Sample	Area	Normal Population					
		# WBC	# RBC	% WBC	% RBC	#/mm <sup>2</sup> WBC	#/mm <sup>2</sup> RBC
A	1	5	218.00	1.85	98.15	25.94	1131.04
A	2	3	199.00	1.63	98.37	15.56	1032.47
A	3	2	294.00	1.31	98.69	10.38	1525.35
A	4	2	279.00	1.21	98.79	10.38	1447.53
A	5	4	223.00	1.86	98.14	20.75	1156.98
A	6	3	211.00	2.09	97.91	15.56	1094.72
A	7	3	198.00	1.69	98.31	15.56	1027.28
A	8	2	278.00	1.38	98.62	10.38	1442.34
A	9	3	284.00	1.98	98.02	15.56	1473.47
A	10	2	244.00	1.90	98.10	10.38	1265.94
A	11	3	227.00	2.93	97.07	15.56	1177.74
A	12	2	246.00	1.55	98.45	10.38	1276.31
A	13	3	270.00	1.90	98.10	15.56	1400.83
A	14	3	260.00	2.00	98.00	15.56	1348.95
A	15	3	262.00	1.82	98.18	15.56	1359.33
A	16	3	213.00	2.01	97.99	15.56	1105.10
A	17	3	243.00	1.59	98.41	15.56	1260.75
A	18	3	271.00	2.01	97.99	15.56	1406.02
A	19	2	259.00	1.45	98.55	10.38	1343.76
A	20	2	272.00	1.38	98.62	10.38	1411.21
B	1	3	241.00	1.86	98.14	15.56	1250.37
B	2	2	251.00	1.39	98.61	10.38	1302.26
B	3	3	256.00	1.60	98.40	15.56	1328.20
B	4	2	246.00	1.22	98.78	10.38	1276.31
B	5	2	262.00	1.36	98.64	10.38	1359.33
B	6	2	279.00	1.05	98.95	10.38	1447.53
B	7	3	253.00	1.89	98.11	15.56	1312.63
B	8	3	257.00	1.72	98.28	15.56	1333.39
B	9	3	235.00	2.00	98.00	15.56	1219.24
B	10	2	257.00	1.40	98.60	10.38	1333.39
B	11	5	261.00	2.63	97.37	25.94	1354.14
B	12	2	252.00	1.87	98.13	10.38	1307.44
B	13	2	265.00	1.39	98.61	10.38	1374.89
B	14	3	253.00	1.79	98.21	15.56	1312.63
B	15	2	252.00	1.79	98.21	10.38	1307.44
B	16	2	281.00	1.80	98.20	10.38	1457.90
B	17	2	244.00	2.08	97.92	10.38	1265.94
B	18	2	246.00	2.17	97.83	10.38	1276.31
B	19	2	244.00	1.72	98.28	10.38	1265.94
B	20	2	216.00	2.04	97.96	10.38	1120.67
C	1	2	232.00	1.45	98.55	10.38	1203.68
C	2	2	240.00	1.04	98.96	10.38	1245.18
C	3	4	219.00	2.46	97.54	20.75	1136.23
C	4	2	229.00	1.48	98.52	10.38	1188.11
C	5	2	260.00	1.09	98.91	10.38	1348.95
C	6	2	282.00	1.74	98.26	10.38	1463.09
C	7	2	228.00	1.45	98.55	10.38	1182.93
C	8	3	253.00	2.45	97.55	15.56	1312.63
C	9	3	258.00	4.81	95.19	15.56	1338.57
C	10	2	179.00	1.43	98.57	10.38	928.70
C	11	2	232.00	1.32	98.68	10.38	1203.68
C	12	3	224.00	2.75	97.25	15.56	1162.17
C	13	4	246.00	3.31	96.69	20.75	1276.31
C	14	2	242.00	1.05	98.95	10.38	1273.16
C	15	3	259.00	2.73	97.27	15.56	1343.76
C	16	2	254.00	1.16	98.84	10.38	1317.82
C	17	2	222.00	1.08	98.92	10.38	1151.80
C	18	2	248.00	1.13	98.87	10.38	1270.12
C	19	2	266.00	1.76	98.24	10.38	1380.08
C	20	2	234.00	1.18	98.82	10.38	1214.06

Table 15: Cytometry statistics for normal population.

# Appendix B: Acute Lymphoblastic Leukemia Samples Analysis

Sample	Area	Acute Lymphoblastic Leukemia - Lymphoblasts															
		Eosin Y					Azure B					Methylene Blue					Cell Index
		Peak (%)	Peak (Int.)	FWHM (Int.)	Mean (Int.)	STD (Int.)	Peak (%)	Peak (Int.)	FWHM (Int.)	Mean (Int.)	STD (Int.)	Peak (%)	Peak (Int.)	FWHM (Int.)	Mean (Int.)	STD (Int.)	
D 2	2	3.3	66	30	67	11	3.8	43	24	43	14	2.0	40	45	42	19	1
D 5	5	4.1	70	22	69	12	2.8	42	33	39	14	2.0	51	46	56	21	1
D 16	16	4.6	66	21	67	9	2.6	50	31	45	17	1.2	36	80	54	36	1
D 21	21	2.8	70	34	69	15	2.4	59	40	57	17	1.6	38	57	45	27	1
D 25	25	3.5	70	27	67	12	3.2	59	28	55	15	1.7	42	59	45	22	1
E 1	1	5.6	69	17	67	9	2.2	37	44	37	16	1.6	60	60	59	25	1
E 3	3	5.0	54	19	53	8	2.4	38	40	37	15	2.2	34	41	38	22	1
E 4	4	5.2	69	18	67	10	1.6	41	56	39	19	0.9	64	113	70	37	1
E 7	7	4.6	67	20	66	10	2.1	55	40	49	19	1.1	41	84	53	33	1
E 8	8	8.1	44	12	44	6	4.3	30	20	28	10	2.9	32	30	39	19	1
E 9	9	8.5	46	11	46	8	4.4	35	18	33	10	3.6	26	21	39	27	1
E 9	9	7.2	47	13	47	7	3.7	31	24	31	11	3.9	32	22	39	20	2
E 10	10	4.6	66	20	64	10	1.8	44	52	42	19	1.2	52	88	56	29	1
E 10	10	6.3	64	15	62	8	1.8	36	53	35	17	1.2	55	83	58	29	2
E 11	11	8.2	46	11	45	7	3.6	33	24	31	10	2.1	29	40	41	26	1
E 12	12	4.0	71	24	69	12	1.7	53	56	49	21	1.2	45	89	52	29	1
E 12	12	4.2	51	24	51	9	3.1	46	27	41	14	1.5	24	61	42	30	3
E 13	13	5.2	42	18	45	10	3.3	37	27	35	12	2.5	21	36	31	23	1
E 14	14	5.7	53	16	53	9	2.2	43	39	40	17	1.3	35	76	51	33	2
E 14	14	6.0	53	15	55	8	2.2	44	36	41	16	1.1	20	87	53	37	3
E 17	17	5.7	46	16	50	9	3.6	40	22	37	13	2.6	20	24	42	32	1
E 18	18	3.5	72	25	68	14	1.7	38	54	39	19	1.1	67	90	73	37	1
E 19	19	4.8	47	20	49	9	2.9	38	33	37	13	2.9	28	29	35	22	1
E 20	20	6.1	50	16	50	7	4.7	29	20	28	9	3.5	44	26	46	16	2
E 21	21	7.2	52	14	51	7	5.2	35	17	34	10	3.7	38	24	42	16	1
E 22	22	6.7	54	14	56	9	3.7	44	24	42	12	2.6	32	31	44	30	1
E 22	22	7.0	50	14	50	6	4.1	34	23	35	10	3.5	37	26	40	14	2
E 24	24	6.1	68	16	67	7	2.6	40	37	39	15	1.9	45	54	45	19	2
E 25	25	3.3	70	31	69	11	2.5	48	39	46	15	1.5	45	68	45	23	1
E 26	26	8.2	51	12	51	5	5.4	35	16	33	9	3.5	35	26	39	18	2
E 28	28	7.4	58	13	58	7	3.9	42	21	38	12	2.4	33	34	47	29	1
E 29	29	4.6	73	19	68	12	2.3	37	36	36	16	1.5	42	58	51	31	1
E 29	29	5.5	56	16	59	10	3.8	28	21	27	10	2.2	21	34	39	30	2
E 30	30	6.9	49	13	52	11	3.5	39	24	38	13	3.0	30	26	44	33	2

Table 16: Analysis of MG-G stain's components uptake for lymphoblasts in ALL samples.

Sample	Area	Acute Lymphoblastic Leukemia - Lymphocytes															
		Eosin Y					Azure B					Methylene Blue					Cell Index
		Peak (%)	Peak (Int.)	FWHM (Int.)	Mean (Int.)	STD (Int.)	Peak (%)	Peak (Int.)	FWHM (Int.)	Mean (Int.)	STD (Int.)	Peak (%)	Peak (Int.)	FWHM (Int.)	Mean (Int.)	STD (Int.)	
D 1	1	4.0	71	25	70	10	3.0	46	30	44	14	2.1	44	45	46	19	1
D 4	4	5.2	73	18	72	9	2.2	49	40	45	18	1.2	49	83	56	31	1
D 6	6	4.4	88	21	86	13	1.4	60	69	58	25	1.0	80	96	77	35	1
D 6	6	5.0	82	18	79	11	2.2	66	37	60	22	1.2	48	82	62	36	2
D 8	8	2.0	76	48	71	19	2.1	67	41	61	21	1.2	53	83	59	30	1
D 9	9	3.5	83	27	81	12	2.1	65	42	59	21	1.3	58	70	61	31	1
D 10	10	4.8	90	19	86	13	1.6	63	59	61	24	1.2	70	78	71	33	1
D 11	11	3.5	85	24	82	15	1.7	60	59	60	22	1.1	70	84	71	32	1
D 12	12	3.9	76	23	72	13	2.3	66	38	59	20	1.3	49	72	56	30	1
D 12	12	5.7	107	13	101	12	1.3	87	77	85	30	1.5	76	66	78	27	2
D 13	13	2.8	82	35	78	14	1.6	55	60	54	23	1.1	79	88	80	33	1
D 13	13	3.4	86	27	83	13	1.7	63	59	63	23	1.4	68	65	71	31	2
D 14	14	3.7	82	23	77	15	1.7	65	57	61	23	1.2	67	77	71	32	1
D 15	15	5.3	86	15	82	13	2.0	82	42	72	25	1.3	47	77	53	28	1
D 17	17	5.0	77	18	74	11	3.0	57	32	56	13	2.2	48	44	49	18	1
D 18	18	4.1	76	22	75	12	2.1	63	41	57	21	1.6	51	60	55	24	1
D 19	19	4.4	87	19	80	13	1.5	68	65	66	24	1.1	65	92	70	34	1
D 19	19	6.1	95	16	94	8	1.8	98	48	88	28	1.0	70	95	77	38	2
D 20	20	3.1	85	27	78	17	2.1	80	45	78	19	1.2	48	82	55	30	1
D 22	22	3.3	78	29	76	14	2.3	65	41	65	19	1.7	42	56	47	24	1
D 23	23	3.3	82	27	80	14	1.3	52	76	55	28	1.5	50	68	52	24	1
D 23	23	5.6	78	17	76	10	2.2	68	38	59	22	1.2	47	85	55	30	2
D 23	23	3.7	75	27	75	10	2.0	61	46	57	21	1.8	43	52	47	22	3
D 26	26	2.7	78	33	73	17	2.4	72	38	66	19	1.3	47	80	54	29	1
D 27	27	4.7	83	21	83	9	2.3	71	37	62	21	1.5	49	64	57	28	1
D 27	27	4.5	90	20	86	13	2.0	64	47	61	21	1.4	70	67	69	28	2
D 28	28	3.5	81	25	76	14	3.0	70	28	62	19	1.6	50	59	56	26	1
D 29	29	3.8	72	25	73	11	2.3	52	40	49	18	1.9	42	47	46	22	1
D 30	30	3.7	73	27	73	11	0.8	61	98	74	45	1.1	32	78	53	38	1
E 6	6	4.1	73	24	72	10	1.3	54	80	51	25	1.1	66	89	67	32	1
E 20	20	3.1	78	30	73	15	1.3	37	76	43	24	1.1	80	83	77	35	1
E 23	23	3.9	81	24	80	11	1.6	67	58	61	24	1.1	64	91	70	36	1
E 23	23	6.2	78	13	74	10	2.0	53	48	49	19	1.3	65	78	67	29	2
E 24	24	3.7	71	26	71	11	2.7	39	35	39	14	1.8	51	54	54	21	1
E 25	25	4.3	77	22	75	11	2.0	52	48	50	19	1.4	57	71	60	27	2

Table 17: Analysis of MG-G stain's components uptake for lymphocytes in ALL samples.

Sample	Area	Acute Lymphoblastic Leukemia					
		# WBC	# RBC	% WBC	% RBC	#/mm <sup>2</sup> WBC	#/mm <sup>2</sup> RBC
D	1	1	302.00	1.47	98.53	5.19	1566.86
D	2	1	197.00	2.08	97.92	5.19	1022.09
D	3	1	138.00	3.79	96.21	5.19	715.98
D	4	1	274.00	1.10	98.90	5.19	1421.59
D	5	1	367.00	1.12	98.88	5.19	1904.09
D	6	2	313.00	1.63	98.37	10.38	1623.93
D	7	1	363.00	1.26	98.74	5.19	1883.34
D	8	1	253.00	1.25	98.75	5.19	1312.63
D	9	1	215.00	0.93	99.07	5.19	1115.48
D	10	1	230.00	0.68	99.32	5.19	1193.30
D	11	1	205.00	0.69	99.31	5.19	1063.60
D	12	2	193.00	1.44	98.56	10.38	1001.34
D	13	2	197.00	1.19	98.81	10.38	1022.09
D	14	1	189.00	0.73	99.27	5.19	980.58
D	15	2	192.00	1.50	98.50	10.38	996.15
D	16	1	230.00	0.87	99.13	5.19	1193.30
D	17	1	359.00	1.03	98.97	5.19	1862.59
D	18	1	191.00	0.97	99.03	5.19	990.96
D	19	2	178.00	1.07	98.93	10.38	923.51
D	20	1	164.00	1.31	98.69	5.19	850.88
D	21	1	189.00	2.23	97.77	5.19	980.58
D	22	1	136.00	2.94	97.06	5.19	705.60
D	23	3	213.00	2.76	97.24	15.56	1105.10
D	24	1	277.00	1.11	98.89	5.19	1437.15
D	25	1	227.00	1.17	98.83	5.19	1177.74
D	26	1	254.00	1.17	98.83	5.19	1317.82
D	27	2	300.00	1.33	98.67	10.38	1556.48
D	28	1	252.00	1.55	98.45	5.19	1307.44
D	29	1	371.00	1.25	98.75	5.19	1924.85
D	30	1	230.00	0.64	99.36	5.19	1191.24
E	1	1	494.00	0.60	99.40	5.19	2563.01
E	2	1	505.00	0.57	99.43	5.19	2620.08
E	3	1	496.00	0.94	99.06	5.19	2573.38
E	4	1	568.00	0.65	99.35	5.19	2946.94
E	5	1	589.00	0.76	99.24	5.19	3055.89
E	6	2	500.00	1.22	98.78	10.38	2594.13
E	7	1	450.00	0.57	99.43	5.19	2334.72
E	8	1	382.00	1.26	98.74	5.19	1981.92
E	9	2	354.00	2.48	97.52	10.38	1836.65
E	10	3	371.00	2.44	97.56	15.56	1924.85
E	11	1	314.00	1.38	98.62	5.19	1629.12
E	12	3	337.00	3.98	96.02	15.56	1748.45
E	13	2	298.00	4.07	95.93	10.38	1546.10
E	14	3	340.00	3.27	96.73	15.56	1764.01
E	15	2	331.00	2.15	97.85	10.38	1717.32
E	16	1	3.00	0.43	99.57	5.19	15.56
E	17	1	481.00	1.01	98.99	5.19	2495.56
E	18	2	494.00	1.28	98.72	10.38	2563.01
E	19	2	552.00	1.50	98.50	10.38	2863.92
E	20	3	640.00	2.19	97.81	15.56	3320.49
E	21	1	666.00	0.97	99.03	5.19	3455.39
E	22	2	593.00	1.76	98.24	10.38	3076.64
E	23	2	592.00	0.82	99.18	10.38	3071.46
E	24	2	353.00	1.35	98.65	10.38	1831.46
E	25	2	588.00	1.18	98.82	10.38	3050.70
E	26	2	521.00	2.22	97.78	10.38	2703.09
E	27	2	477.00	1.57	98.43	10.38	2474.80
E	28	1	626.00	0.76	99.24	5.19	3247.86
E	29	3	504.00	2.01	97.99	15.56	2614.89
E	30	2	328.00	1.54	98.46	10.38	1701.75

Table 18: Cytometry statistics for ALL samples.

# Appendix C: Chronic Lymphocytic Leukemia Samples Analysis

Ασθενής	Περιοχή	Χρόνια Λεμφοκυτταρική Λευχαιμία															Cell Index
		Eosin Y					Azura B					Methylene Blue					
		Peak (%)	Peak (Int.)	FWHM (Int.)	Mean (Int.)	STD (Int.)	Peak (%)	Peak (Int.)	FWHM (Int.)	Mean (Int.)	STD (Int.)	Peak (%)	Peak (Int.)	FWHM (Int.)	Mean (Int.)	STD (Int.)	
F	1	3.1	90	27	83	17	2.0	65	47	66	20	1.5	63	63	63	27	1
F	1	3.3	80	30	79	12	3.5	43	28	41	12	1.6	64	60	67	25	2
F	2	5.6	90	16	86	12	1.3	37	78	40	22	0.9	93	108	95	38	2
F	2	5.0	90	18	86	13	1.5	55	60	50	23	1.0	90	93	93	38	3
F	2	6.3	90	14	86	11	1.8	49	49	47	19	1.2	78	79	85	35	5
F	3	3.2	75	31	74	13	2.3	53	39	51	18	1.3	48	74	56	31	2
F	3	4.7	79	19	78	11	2.2	45	43	43	16	1.7	61	57	62	23	4
F	4	5.1	84	18	81	11	2.3	52	43	51	16	1.7	60	58	59	23	1
F	4	4.6	85	20	82	12	2.3	54	42	51	18	1.3	62	74	64	29	2
F	4	2.9	91	31	85	16	1.7	62	55	59	23	1.1	71	85	73	34	3
F	4	4.8	89	18	85	12	2.0	49	45	48	19	1.5	68	60	72	30	4
F	6	4.2	86	22	83	13	2.3	46	45	46	16	1.6	68	59	66	24	1
F	6	2.8	82	34	78	16	2.1	55	47	55	18	1.4	54	67	58	28	2
F	6	3.3	82	27	79	15	2.5	50	39	48	16	1.3	59	75	64	30	4
F	6	3.1	80	30	78	14	2.2	46	46	45	17	1.2	61	79	64	30	5
F	7	3.1	84	31	82	14	2.3	49	44	47	16	1.4	65	69	68	27	1
F	7	5.4	95	16	91	12	1.3	51	74	53	26	0.9	91	105	92	40	2
F	7	4.9	94	17	87	14	1.0	47	93	49	26	0.9	94	110	96	42	5
F	8	5.1	71	19	70	9	2.7	42	35	40	14	1.6	52	61	56	26	1
F	8	4.9	85	19	82	10	2.5	48	40	47	15	1.8	62	54	63	22	2
F	8	3.7	82	25	79	12	2.0	47	48	46	19	1.4	67	67	67	27	3
F	8	3.8	76	24	75	11	2.9	46	32	46	15	1.7	54	57	56	23	4
F	9	3.7	80	27	79	11	2.2	49	44	48	18	1.3	60	73	62	27	1
F	9	2.9	82	33	80	14	2.0	43	47	42	17	1.3	71	70	76	30	2
F	9	4.2	83	23	81	11	1.9	59	47	54	21	1.2	53	87	59	31	3
F	10	4.8	89	19	86	11	2.1	49	46	46	19	1.5	71	65	73	28	1
F	10	3.3	86	28	86	13	2.2	56	43	54	18	1.4	64	67	68	31	2
F	11	4.8	85	19	82	11	2.2	46	45	44	17	1.4	67	70	67	27	1
F	11	3.3	87	29	86	12	1.4	69	64	64	27	1.0	58	103	67	37	2
F	12	4.3	87	20	84	13	2.0	48	48	47	19	1.3	69	78	71	30	2
F	13	5.3	85	17	83	11	1.7	56	55	54	22	1.1	61	89	67	34	2
F	13	4.1	82	23	79	11	1.8	59	55	57	21	1.5	48	64	51	25	3
F	14	4.3	70	22	70	9	4.3	41	21	39	10	1.9	51	49	55	22	1
F	14	4.0	82	25	81	10	1.7	49	53	48	20	1.0	68	101	72	36	2
F	15	5.8	85	16	83	10	2.2	44	42	40	17	1.8	68	56	70	21	1
F	15	4.0	72	25	70	11	3.5	45	27	46	13	1.6	47	61	49	22	2
F	15	6.4	81	14	79	9	3.1	53	28	49	15	2.1	48	40	57	26	4
G	1	3.4	82	27	80	14	1.3	59	71	56	26	1.0	40	92	59	40	1
G	1	4.1	85	22	84	12	1.7	61	52	55	22	1.1	56	95	61	31	2
G	1	5.0	89	19	88	10	1.5	74	61	69	25	0.9	42	102	58	37	3
G	1	4.3	91	20	89	13	1.7	74	55	65	25	1.1	65	86	68	33	4
G	1	4.0	86	24	86	10	1.4	65	69	65	27	0.9	51	105	58	33	5
G	2	4.5	77	20	75	12	2.3	50	41	47	16	1.3	52	73	55	28	2
G	2	3.9	86	23	82	13	1.2	55	81	54	26	1.0	79	88	76	35	3
G	2	3.5	92	27	90	13	1.5	59	64	59	24	1.0	71	93	73	36	4
G	2	5.5	93	17	91	9	1.3	66	74	62	27	0.9	73	109	79	43	5
G	2	2.8	79	27	72	14	1.2	54	73	53	26	0.8	70	127	77	42	8
G	3	3.4	84	30	83	12	1.4	70	64	64	25	0.8	60	121	70	41	1
G	3	3.4	83	28	81	13	1.4	62	67	59	25	1.0	58	90	63	35	2
G	3	3.1	85	30	82	14	1.5	62	65	59	24	1.1	61	82	62	32	3
G	3	4.1	85	21	84	13	1.6	56	59	55	23	1.2	58	85	63	33	4
G	3	3.7	80	23	77	15	1.4	44	66	46	24	1.0	94	93	96	39	5
G	3	5.6	92	15	91	12	1.3	68	77	65	26	1.0	64	109	68	37	6
G	4	4.2	85	22	83	12	1.7	61	57	58	22	1.0	60	94	64	34	1
G	4	3.7	82	25	81	13	1.5	64	60	60	24	1.1	57	92	63	34	2
G	4	4.0	93	23	91	12	1.7	76	59	71	23	1.2	58	78	62	29	3
G	4	3.9	84	22	80	16	1.4	68	68	65	26	1.0	65	93	66	33	4
G	4	2.8	84	33	81	15	1.2	66	76	62	27	0.9	59	110	68	39	5
G	5	4.4	83	20	83	12	1.4	69	69	65	26	1.0	59	100	64	34	2
G	5	3.7	79	25	79	13	1.5	64	64	59	24	0.9	40	104	58	36	3
G	5	3.2	71	30	70	14	2.2	59	41	55	19	1.2	45	88	52	30	4
G	5	2.9	85	32	84	14	1.8	73	53	68	23	1.2	66	78	69	34	5
G	5	2.5	92	36	86	20	1.4	71	71	69	26	1.1	75	87	77	33	6
G	6	5.6	83	13	76	13	1.2	66	77	61	28	0.9	55	120	70	42	1
G	6	3.5	95	24	90	16	2.3	76	40	77	20	1.2	77	80	76	31	3
G	6	3.5	89	28	87	13	1.3	69	71	63	27	1.1	61	89	63	33	5
G	6	3.3	83	29	81	12	1.4	64	65	59	24	0.9	58	109	68	39	6
G	7	3.2	85	29	84	15	1.5	71	61	67	26	1.2	58	80	61	29	2
G	7	3.7	76	23	72	14	1.4	54	71	53	24	0.9	67	100	69	36	3
G	7	5.2	76	17	74	11	1.7	43	55	44	19	1.2	64	82	66	31	4
G	7	4.1	81	24	83	10	1.8	55	51	52	22	1.2	39	81	51	32	5
G	7	5.1	84	17	83	13	1.6	69	61	66	24	1.3	60	72	66	32	6
G	8	3.6	85	25	81	15	1.8	63	49	62	22	1.1	57	84	63	34	1
G	8	3.2	77	31	76	13	1.4	51	68	50	23	0.9	80	104	80	41	2
G	8	4.8	75	18	70	13	1.5	52	56	47	22	0.9	59	111	67	37	3
G	8	3.8	76	23	74	14	1.4	57	62	54	23	0.8	68	126	77	43	4
G	8	3.1	84	31	81	14	1.5	58	66	55	23	1.0	66	94	68	35	5
G	8	5.4	80	15	78	13	1.8	56	50	54	21	1.1	57	83	65	36	6
G	8	4.3	94	22	92	11	1.3	66	74	67	29	1.0	78	88	79	37	7
G	9	3.2	83	29	81	13	1.6	59	53	55	22	1.0	61	88	69	38	1
G	9	3.6	79	26	78	12	1.5	64	59	60	24	1.0	52	102	61	35	2
G	9	4.1	81	22	78	13	1.4	55	71	51	24	1.0	70	93	72	35	3
G	9	4.3	80	20	78	12	1.4	48	67	49	23	1.0	68	92	70	36	4
G	9	3.7	74	23	70	14	1.9	49	48	45	19	1.1	60	91	64	32	5
G	9	3.5	77	27	76	13	1.4	49	61	48	23	1.0	61	94	65	34	6
G	9	4.0	84	24	83	11	1.3	64	73	60	27	1.1	56	89	59	30	7
G	9	3.4	72	28	70	13	1.6	57	61	53	23	1.1	43	95	55	34	8
G	10	3.4	96	28	93	12	1.6	79	56	77	27	1.0	62	100	69	36	1
G	10	3.6	86	25	81	15	1.3	62	71	62	26	1.0	68	92	69	33	2
G	10	3.2	84	30	83	12	1.5	63	64	60	24	1.1	59	90	62	33	3
G	10	3.4	71	27	70	12	1.8	52	52	48	20	1.0	62	106	66	36	4
G	10	3.5	81	26	79	13	1.5										

G	15	3.0	80	30	75	15	2.0	38	48	36	17	1.1	77	87	81	35	1
G	15	3.2	76	31	75	13	1.6	46	57	45	21	0.9	73	103	76	38	2
G	15	2.8	80	34	79	14	1.3	55	70	52	24	0.9	63	111	70	39	3
G	15	3.0	79	32	77	14	1.3	39	77	42	23	1.0	76	99	78	38	4
G	15	3.3	83	26	78	16	1.9	36	53	36	18	1.2	81	81	82	32	5
G	15	2.5	77	37	80	18	1.2	42	76	43	23	0.8	70	113	87	55	6
H	1	5.6	89	15	84	12	2.5	48	39	48	16	1.6	63	59	62	24	2
H	1	6.3	84	14	82	9	2.3	53	42	54	17	2.1	49	44	48	19	3
H	1	5.2	85	18	82	10	2.2	42	41	44	18	1.8	59	50	61	28	4
H	1	3.5	76	27	74	11	3.1	41	30	41	14	2.8	45	33	45	16	5
H	2	5.3	79	17	77	10	2.4	56	39	54	16	2.3	45	39	48	25	1
H	2	4.6	87	19	84	11	2.2	51	44	50	18	1.7	57	57	57	22	2
H	3	4.7	86	18	80	13	1.5	67	60	62	25	1.1	72	91	75	36	1
H	3	5.4	79	16	78	10	1.9	53	50	53	20	1.8	47	52	50	26	2
H	3	4.4	82	21	80	11	3.0	54	33	54	13	2.3	48	42	49	18	3
H	4	5.0	83	18	81	10	2.6	56	36	56	16	1.8	49	51	53	24	2
H	4	3.8	85	25	85	12	2.5	62	38	59	17	1.6	50	57	56	28	3
H	4	3.8	76	25	75	11	2.3	56	40	52	18	1.5	51	63	55	27	4
H	4	4.2	81	22	79	11	2.0	62	43	56	22	1.2	51	80	56	29	5
H	5	4.3	86	22	84	10	2.4	81	33	71	24	1.2	37	76	51	34	2
H	5	4.8	88	18	84	13	2.0	67	43	63	22	1.3	49	73	57	32	5
H	6	4.4	87	21	84	12	1.6	64	57	60	23	0.9	58	114	66	36	1
H	6	3.7	89	25	87	14	1.2	58	76	59	28	0.9	73	118	77	40	4
H	7	3.6	100	25	96	14	1.3	83	71	80	29	1.0	71	94	75	38	1
H	7	4.1	100	21	94	14	1.7	87	55	81	25	1.3	65	67	68	31	2
H	7	4.6	95	19	91	13	1.5	73	63	71	26	1.2	76	81	75	31	3
H	7	2.8	89	35	88	15	1.5	77	58	71	27	0.9	60	108	67	36	4
H	7	6.4	99	14	97	10	1.5	89	64	86	25	1.1	60	91	63	33	5
H	8	3.6	90	24	87	14	1.6	76	60	70	25	1.0	61	101	67	36	2
H	8	3.3	92	29	90	13	1.2	78	83	76	29	1.0	63	89	69	36	4
H	8	3.3	87	29	85	13	2.0	83	42	74	25	1.0	56	107	63	35	5
H	9	4.2	109	21	103	14	1.3	96	73	95	29	1.0	80	97	83	37	3
H	9	3.5	94	27	93	13	1.4	90	68	84	29	0.9	68	111	75	40	5
H	9	4.9	104	19	103	11	1.2	101	84	99	33	0.8	53	132	76	47	8
H	10	3.9	86	24	86	11	1.8	67	48	61	23	1.2	51	81	60	33	1
H	10	4.7	83	19	81	11	2.4	65	36	60	20	1.7	53	56	58	25	2
H	10	4.0	87	24	85	11	1.8	82	47	74	26	1.0	27	90	53	35	4
H	11	4.1	89	22	86	13	1.6	81	65	76	23	1.0	48	99	57	33	1
H	11	4.2	94	22	91	12	1.2	73	78	72	29	1.0	67	99	74	38	5
H	11	3.2	96	28	91	16	1.5	84	65	81	27	1.0	58	103	67	37	6
H	12	6.0	87	14	82	12	2.8	67	33	63	17	1.7	52	56	54	24	4
H	13	4.0	97	23	94	11	1.2	88	83	85	32	1.0	65	88	74	39	1
H	13	2.8	89	34	86	15	1.3	78	77	75	28	1.0	70	93	73	36	3
H	13	4.1	93	22	90	12	1.6	90	60	87	27	1.1	56	82	66	37	4
H	13	3.6	89	25	87	13	1.1	73	87	71	32	0.8	77	134	83	47	5
H	14	4.3	84	22	81	11	1.4	72	73	67	26	1.0	58	98	64	35	1
H	14	4.6	96	21	94	10	1.4	82	71	79	27	1.0	63	103	71	38	2
H	14	5.0	77	19	75	10	2.2	60	41	56	19	1.6	52	60	56	29	4
H	14	3.9	82	25	82	11	1.7	65	59	61	21	1.0	56	97	63	35	5
H	14	4.9	88	18	87	11	1.6	69	60	66	24	1.0	60	106	71	39	6
H	14	4.0	88	23	84	13	1.8	80	51	73	23	1.3	54	72	60	31	8
H	15	4.0	77	23	75	12	2.7	49	36	49	15	1.6	55	61	56	24	2
H	15	3.9	87	22	82	15	2.8	49	34	48	14	1.5	65	64	66	25	3
H	15	3.9	90	22	85	15	2.1	50	47	49	18	1.4	73	69	71	29	5
I	2	4.1	83	22	80	11	1.9	49	52	48	20	1.8	63	52	62	22	2
I	3	4.5	89	21	87	11	1.9	53	50	53	20	1.4	68	67	69	27	1
I	4	4.5	81	21	80	9	2.7	52	34	50	16	1.6	64	59	64	23	1
I	4	4.7	86	20	85	9	2.4	62	37	59	20	1.5	56	60	62	29	3
I	6	4.5	76	21	75	10	2.7	47	36	44	14	1.8	57	53	59	23	1
I	6	3.9	78	25	78	11	2.1	58	40	53	21	1.2	57	82	63	31	2
I	6	4.3	72	23	71	9	2.9	50	32	48	15	1.6	51	60	53	24	3
I	7	4.7	79	20	77	10	2.6	52	37	53	15	1.7	57	56	57	23	1
I	7	4.3	83	21	80	11	1.4	53	67	49	23	0.9	65	119	70	38	3
I	8	4.9	83	19	82	10	1.8	56	50	50	21	1.1	63	92	71	34	2
I	9	5.2	74	19	73	8	3.5	53	24	48	14	1.7	50	51	54	26	2
I	9	6.2	84	15	82	8	1.8	62	46	58	22	1.2	55	82	63	34	3
I	10	4.3	86	23	85	10	2.1	67	46	65	19	1.4	55	70	57	28	2
I	10	6.3	85	15	83	9	2.2	61	37	53	21	1.3	56	69	66	33	3
I	11	5.0	81	19	79	9	2.0	54	43	50	19	1.4	57	68	63	30	1
I	12	4.5	82	21	81	10	1.9	53	47	49	19	0.9	61	109	71	40	1
I	12	3.8	82	26	81	10	2.3	60	41	57	17	1.4	60	72	60	27	2
I	13	4.3	73	23	72	9	3.2	57	29	55	15	1.5	47	63	52	27	1
I	13	4.4	72	22	70	10	3.2	58	28	55	14	1.2	41	83	52	32	2
I	15	4.2	87	22	85	10	2.3	63	41	59	18	1.5	55	66	58	27	3

Table 19: Analysis of MG-G stain's components uptake for lymphocytes in CLL samples.

Sample	Area	Chronic Lymphocytic Leukemia					
		# WBC	# RBC	% WBC	% RBC	#/mm <sup>2</sup> WBC	#/mm <sup>2</sup> RBC
F	1	2	256.00	2.00	98.00	10.38	1328.20
F	2	6	311.00	3.07	96.93	31.13	1613.55
F	3	4	291.00	3.60	96.40	20.75	1509.79
F	4	4	259.00	2.29	97.71	20.75	1343.76
F	5	3	240.00	1.67	98.33	15.56	1245.18
F	6	5	303.00	2.74	97.26	25.94	1572.05
F	7	5	225.00	2.74	97.26	25.94	1167.36
F	8	4	296.00	2.82	97.18	20.75	1535.73
F	9	3	283.00	1.85	98.15	15.56	1468.28
F	10	3	285.00	2.25	97.75	15.56	1478.66
F	11	2	298.00	1.26	98.74	10.38	1546.10
F	12	2	262.00	1.66	98.34	10.38	1359.33
F	13	3	285.00	2.44	97.56	15.56	1478.66
F	14	2	231.00	1.66	98.34	10.38	1198.49
F	15	4	218.00	4.46	95.54	20.75	1131.04
G	1	5	239.00	2.93	97.07	25.94	1240.00
G	2	8	233.00	5.12	94.88	41.51	1208.87
G	3	6	236.00	3.11	96.89	31.13	1224.43
G	4	5	238.00	2.73	97.27	25.94	1234.81
G	5	6	226.00	2.97	97.03	31.13	1172.55
G	6	7	256.00	4.25	95.75	36.32	1328.20
G	7	6	234.00	2.73	97.27	31.13	1214.06
G	8	7	216.00	3.68	96.32	36.32	1120.67
G	9	8	233.00	4.50	95.50	41.51	1208.87
G	10	7	258.00	3.48	96.52	36.32	1338.57
G	11	6	225.00	4.06	95.94	31.13	1167.36
G	12	3	257.00	2.11	97.89	15.56	1333.39
G	13	7	220.00	4.88	95.12	36.32	1141.42
G	14	5	228.00	2.77	97.23	25.94	1182.93
G	15	6	229.00	3.58	96.42	31.13	1188.11
H	1	5	254.00	3.97	96.03	25.94	1317.82
H	2	2	238.00	1.64	98.36	10.38	1234.81
H	3	3	252.00	2.60	97.40	15.56	1307.44
H	4	5	252.00	3.23	96.77	25.94	1307.44
H	5	5	208.00	3.98	96.02	25.94	1079.16
H	6	4	207.00	2.63	97.37	20.75	1073.97
H	7	5	213.00	2.15	97.85	25.94	1105.10
H	8	6	218.00	4.38	95.62	31.13	1131.04
H	9	8	188.00	4.37	95.63	41.51	975.39
H	10	5	185.00	4.06	95.94	25.94	959.83
H	11	6	174.00	4.43	95.57	31.13	902.76
H	12	4	217.00	3.61	96.39	20.75	1125.85
H	13	5	200.00	3.10	96.90	25.94	1037.65
H	14	8	234.00	5.45	94.55	41.51	1214.06
H	15	6	224.00	4.02	95.98	31.13	1162.17
I	1	2	266.00	1.69	98.31	10.38	1380.08
I	2	3	276.00	2.81	97.19	15.56	1431.96
I	3	3	252.00	1.96	98.04	15.56	1307.44
I	4	5	258.00	2.30	97.70	25.94	1338.57
I	5	2	266.00	1.69	98.31	10.38	1380.08
I	6	3	318.00	1.89	98.11	15.56	1649.87
I	7	3	302.00	1.45	98.55	15.56	1566.86
I	8	2	257.00	1.34	98.66	10.38	1333.39
I	9	3	276.00	2.54	97.46	15.56	1431.96
I	10	3	295.00	2.23	97.77	15.56	1530.54
I	11	3	299.00	1.98	98.02	15.56	1551.29
I	12	3	267.00	2.79	97.21	15.56	1385.27
I	13	2	275.00	1.57	98.43	10.38	1426.77
I	14	2	267.00	1.86	98.14	10.38	1385.27
I	15	4	288.00	2.78	97.22	20.75	1494.22

Table 20: Cytometry statistics for CLL samples.